STOCKHOLM OBSERVATORY
DEPARTMENT OF ASTRONOMY

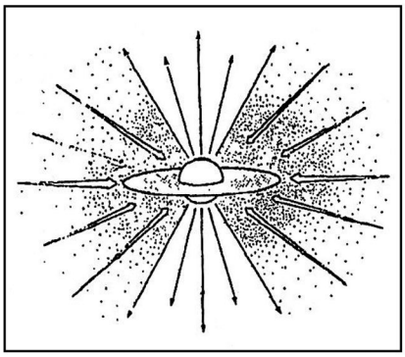

# L-BAND (3.5 μm) IR-EXCESS AS AN INDICATOR OF CIRCUMSTELLAR DISKS

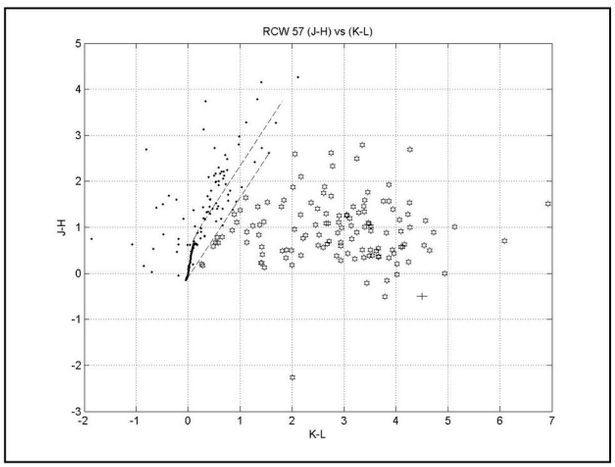


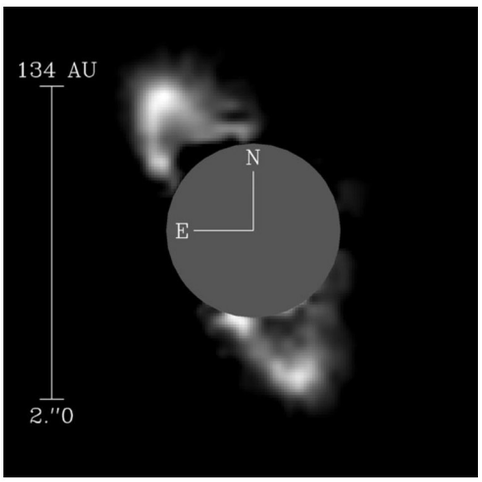


**A MASTERS THESIS IN ASTRONOMY**

**MATTHIAS MAERCKER, 2004**

UNSW
DEPARTMENT OF
ASTROPHYSICS AND OPTICS

# L-band (3.5 μm) IR-excess as an Indicator of Circumstellar Disks

A Masters Thesis in Astronomy

Matthias Maercker

Department of Astronomy, Stockholm Observatory
Stockholm University

Department of Astrophysics and Optics
University of New South Wales

2004

# Contents

## 1. Introduction

Using images of 30 Doradus, RCW 57 and the Galactic Centre obtained by the 60 cm SPIREX telescope at the South Pole in the L-band (3.5 μm) (and Br α (4.05 μm) for the Galactic Centre), combined with JHK (1.25 - 2.2 μm) data from 2MASS, colour-colour diagrams are created in order to detect infrared excess. The infrared excess is interpreted as coming from circumstellar disks. Using the longer wavelength data at 3.5 μm combined with the shorter wavelength data at 1-2μm, creating (J-H) vs (K-L) colour-colour diagrams, proves to be a more effective way of determining the disk fraction of a given cluster than simply using the latter. The results from the photometry with IRAF on the SPIREX data are matched with the 2MASS point-source-catalogue. The derived disk fraction is used to estimate the probability for stars to form disks (i.e. the initial disk fraction), the dependence of this on stellar mass and the lifetime of circumstellar disks. The results are compared to earlier studies of the same or similar regions. The data for 30 Doradus and RCW 57 fit well with the previous estimations, confirming a high initial disk fraction (>80%) and an average lifetime of ~6 Myr. SPIREX observations of the Galactic Centre at 4.05μm reveal signs of pre-main sequence stars with circumstellar disks. Interestingly, all SPIREX images contain sources not detected in the shorter wavebands, indicating heavily embedded sources which possibly could be massive stars with disks. Finally, an image of the PAH (3.28 μm) emission towards RCW 38 is presented, showing that these emission features wrap around the HII region identified in the near-infrared images.

## 2. About this thesis

This thesis is the written part towards a masters of science in astronomy at the Stockholm Observatory at Stockholms Universitet in Sweden under supervision of Prof. Hans Olofsson. The practical work was done between February and July 2004 at the department of Astrophysics and Optics at the University of New South Wales in Sydney, Australia under supervision of Dr. Michael Burton. The thesis involves analysing images taken through near-infrared filters (J-band (1.25 μm), H-band (1.65 μm), K-band (2.2 μm), L-band (3.5 μm), Br α (4.05 μm) and PAH emission (3.28 μm)). The analysed images in the J, H and K-bands are from the 2MASS survey. Images in the other wavebands are from SPIREX and magnitudes are sometime referred to as $m_{SPIREX}$, meaning the magnitude in the respective wavelengths. All coordinates given in this thesis are in J2000. The thesis is separated into three parts. Part one gives the relevant theoretical background in star formation and IR observations. Part two describes the process from collecting the data to the final results. Part three discusses the results and presents the conclusions. A list of literature cited in the thesis is given in appendix A. Appendix B contains my photometric results including the coordinates for each star found. Finally, Appendix C gives the values of the parameters used during the analysis process.

## PART 1: THEORETICAL BACKGROUND

# 3. Star Formation

## 3.1. Molecular Clouds

The typical particle density of the interstellar medium is n ~1 $cm^{-3}$. Regions with a density n > 10 $cm^{-3}$ are defined as interstellar clouds. Some of these clouds are molecular clouds, which can be separated into giant molecular clouds (GMC) and dark clouds. GMCs are the places of high-mass star formation and dark clouds generally the birthplaces of low-mass stars. The sizes of cloud complexes range from 6-10 pc and $10^3$-$10^4$ $M_{sun}$ for dark clouds, to 20-60 pc and $10^4$-$10^6$ $M_{sun}$ for GMCs. Inhomogeneity is found on all scales, with cloud complexes showing substructures in the form of individual clouds, denser cores within the clouds, even denser clumps and hot molecular cores (HMC) (table 1). Star formation is believed to take place in these dense clumps when the cloud starts contracting under its own gravity. The minimum mass required to start the collapse of the molecular cloud can be derived when assuming that the collapse is opposed only by the thermal pressure of the collapsing cloud. The first person to do this was Jeans, giving

$$M_J = \left(\frac{5k_BT}{G\mu m_H}\right)^{3/2}\left(\frac{3}{4\pi\rho_0}\right)^{1/2}, \qquad (1)$$

where T is the temperature, µ the mean molecular weight, $\rho_0$ the (assumed constant) density of the cloud and all other constants take their usual definitions. Clouds with masses larger than the Jeans Mass should contract under their own gravity. However, clouds with masses larger than $M_J$ are often observed, suggesting that there must be an additional mechanism to halt the collapse besides the thermal pressure. Today it is believed that this mechanism is a combination of turbulent motion within the cloud and magnetic fields (e.g. Brandeker, 2003; Shu et al, 1987).

| *Parameters* | | *Complex* | *Cloud* | *Core* | *Clump* | *HMC* |
|---|---|---|---|---|---|---|
| ***Giant Molecular Clouds*** | | | | | | |
| Size | (pc) | 20-60 | 3 - 20 | 0.5 - 3 | < 0.5 | < 0.1 |
| Density | ($cm^{-3}$) | 100-300 | $10^3$ - $10^4$ | $10^4$ - $10^6$ | > $10^6$ | $10^5$ - $10^8$ |
| Mass | ($M_{Sun}$) | $10^4$ - $10^6$ | $10^3$ - $10^4$ | 10 - $10^3$ | 30 - $10^3$ | ~ 100 |
| Line Width | (km/s) | 6 – 15 | 4 - 12 | 1 - 3 | 4 - 15 | 4 - 10 |
| Temperature | (K) | 7 – 15 | 15 - 40 | 30 - 100 | 30 - 200 | 50 - 250 |
| Examples | | W51; W3; M17 | OMC1; W33;W3A | Orion Ridge | W3(OH) | W3($H_2O$) |
| ***Dark Clouds*** | | | | | | |
| Size | (pc) | 6 – 10 | 0.2 - 4 | 0.1 - 0.4 | | |
| Density | ($cm^{-3}$) | $10^2$ – $10^4$ | $10^2$ - $10^4$ | $10^4$ - $10^5$ | | |
| Mass | ($M_{Sun}$) | $10^3$ - $10^4$ | 5 - 500 | 0.3 - 10 | | |
| Line Width | (km/s) | 1 – 3 | 0.5 - 1.5 | 0.2 - 0.4 | | |
| Temperature | (K) | ~ 10 | ~ 8 - 15 | ~ 10 | | |
| Examples | | Taurus; Perseus; ρ-Oph | B227; HCL2; B5; L1495 | TMC1; TMC2; B1 | | |

*Table 1: Physical properties of the components within GMC and dark clouds (adapted from Rathborne, 2003).*

### 3.2. Gravitational collapse

Eventually however, the cloud will lose the magnetic and turbulent support and enter a super-critical state at which it starts to collapse under its own gravity (Shu et al, 1987). This collapse is a run-away process, since the collapse increases the density in the core which leads to a decrease in $M_J$ (formula 1) and therefore to an even more super-critical state. When heat is released quickly during infall (keeping the cloud isothermal), the pressure is not strong enough to halt the collapse. The timescale for this is just the free-fall time for a shell of collapsing material to reach the core of the to-be star. The free-fall time is given by

$$t_{ff} = \sqrt{\frac{3\pi}{31 G \rho_0}} \approx 4 \cdot 10^7 \sqrt{\frac{cm^{-3}}{n}} yr \,, \qquad (2)$$

where n is the mean particle density. For typical densities the free-fall time is on the order of $10^5$ years. Stars leave their protostellar phase and settle on the zero-age-main-sequence (ZAMS) when the core becomes optically thick resulting in a rise in temperature and eventually hydrogen burning sets in. The timescale for this to start is given by the Kelvin-Helmholtz timescale and is relatively long for low-mass stars (on the order of ~3x$10^7$ yrs for 1 $M_{Sun}$) and rather short for high-mass stars (~$10^4$ yrs for 50 $M_{Sun}$). This means that high-mass stars are still forming when they ignite hydrogen burning and settle on the ZAMS. The fact that they then are still embedded in their molecular clouds is what makes it so complicated to study high-mass star formation (Rathborne, 2003).

### 3.3. Protostars to main sequence

The protostellar phase begins when the thermal pressure inside the collapsing cloud becomes high enough to halt the collapse. The conservation of angular momentum **L** = m**r** x **v** of the infalling material causes the material to increase its rotation around the protostar. As the distance **r** to the star decreases the velocity **v** of the particles must increase in a direction perpendicular to the angular momentum and the direction of infall, hence causing rotation. However, the change in angular momentum is less for particles moving parallel to **L** and **r** and they therefore feel less of the resistance of inertial momentum than particles moving perpendicular to **L**. This allows the matter directly above the poles to freely fall onto the core, while matter further away from the poles is forced into a rotating disk. The star continues to accrete mass from the disk, this being one of the main means by which stars accrete most of their dust and gas (Haisch et al, 2001 April). During infall, only a small preferred direction of rotation would lead to rotation velocities far above the escape velocity of the protostar. Something must happen to keep the cloud from blowing apart during collapse. A means by which protostars can lose angular momentum and mechanical energy is by developing bipolar outflows. The outflows are created as more and more matter accretes onto the disk instead of the protostar. The exact mechanism of how they occur is however not known. The strong winds move radially outward from the poles of the star at high speeds. While moving through the remnants of the molecular cloud they produce shocks which produce line emission from dissociated molecules. These objects are called Herbig-Haro (HH) objects and are found in star forming regions, often associated with T Tauri stars. At this stage the protostar with the circumstellar disk and molecular outflow is still heavily embedded in a dusty envelope from the molecular cloud. All along matter keeps falling onto the core and as the protostar contracts, half of the gravitational potential energy is radiated away. This causes the core to heat up, until eventually the temperature rises enough to ignite hydrogen, ending the protostellar phase (Christensen-Dalsgaard, 2000). At this stage the protostar radiates mainly in the infrared as the dust absorbs and re-emits the radiation absorbed by the dust at shorter wavelengths. Absorbing the radiation at shorter wavelengths heats the dust up and causes thermal radiation. Circumstellar gas and dust are therefore easiest to observe at infrared wavelengths.
At the stage of T Tauri stars, the molecular outflows have blown away most of the mass that hasn't accreted onto the star. Accretion still takes place through the circumstellar disk, adding luminosity to

the star comparable to the energy generated through hydrogen burning. The star and its disk are now optically visible and have settled on the ZAMS. It is at this stage that it is believed that the dust particles start sticking together to form planetesimals, which eventually might develop into planetary systems (Brandeker, 2003), (Rathborne, 2003).

### 3.4. High-mass star formation

The formation scenario of low-mass stars is not directly applicable to high-mass stars, since the effect of high-mass stars on their surroundings raises the question whether they follow the same evolution as low-mass stars. The radiation pressure from the core will halt the accretion of mass and therefore prevent stars with masses larger than ~10 $M_{sun}$ from forming. Proposed solutions to this problem are that high-mass stars either form through the merger of low-mass stars, or that they form as low-mass stars do, although with much higher accretion rates. The merger of low-mass stars into higher mass stars only works in the very early stages of star formation. However, the limit of about 10 $M_{Sun}$ due to radiation pressure applies to spherical accretion onto a star. A non-spherical dust distribution, such as an accretion disk, would significantly lower the radiation pressure, allowing higher-mass stars to form. A combination of both higher accretion rates and circumstellar disks seems to be required to form high-mass stars (Rathborne, 2003). Because high-mass stars start hydrogen burning already before they emerge from their molecular clouds, the surrounding material gets exposed to large amounts of UV radiation, ionizing the matter and creating compact HII regions. The surrounding molecular cloud also makes it hard or impossible to observe the formation of high-mass stars directly. Further, the fact that high-mass stars preferably form in clusters makes it hard to assign phenomena as outflows and disks to individual stars. However, these features are strong in the infrared, mm and radio wavelengths and observations at these wavelengths can be used to examine the evolution of high-mass star formation.

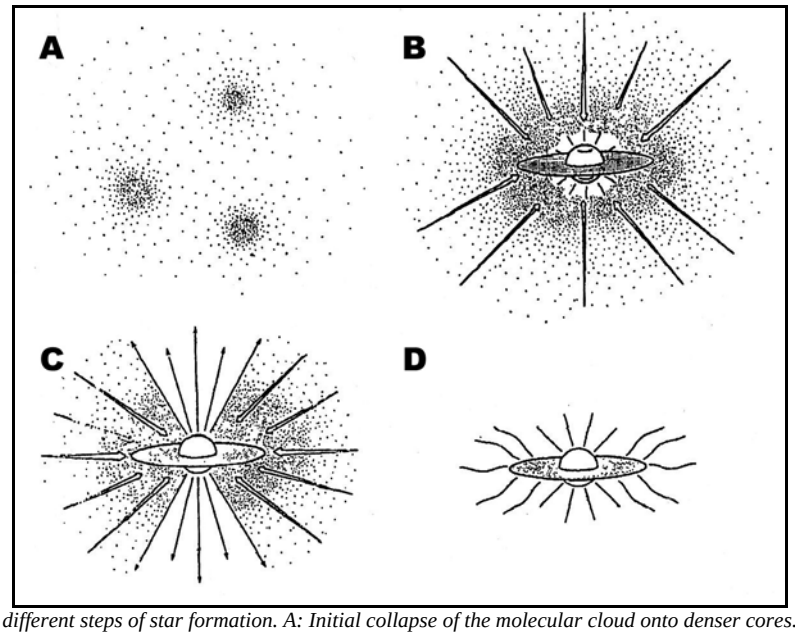


*Figure 1: The different steps of star formation. A: Initial collapse of the molecular cloud onto denser cores. B: the heavily embedded protostar with disk. C: The T Tauri phase with molecular outflows and a disk. D: ZAMS star with remaining disk. Image adapted from Shu, Adams, Lizano, 1987.*

### 3.5. Stages of stellar evolution as indicated by Spectral Energy Distributions (SEDs)

During star formation, young stellar objects (YSOs) are associated with the circumstellar material surrounding them, making them very bright at infrared wavelengths by absorbing and re-emitting the radiation from the central star. As the star evolves the distribution of the surrounding material evolves with the star, which is reflected in the spectral energy distribution (SED) of the star. SEDs can therefore be used as an indicator of the evolutionary state a YSO is in. The evolutionary sequence can be separated into four classes, each class representing a distribution of circumstellar material, with a diminishing of circumstellar dust along the sequence.

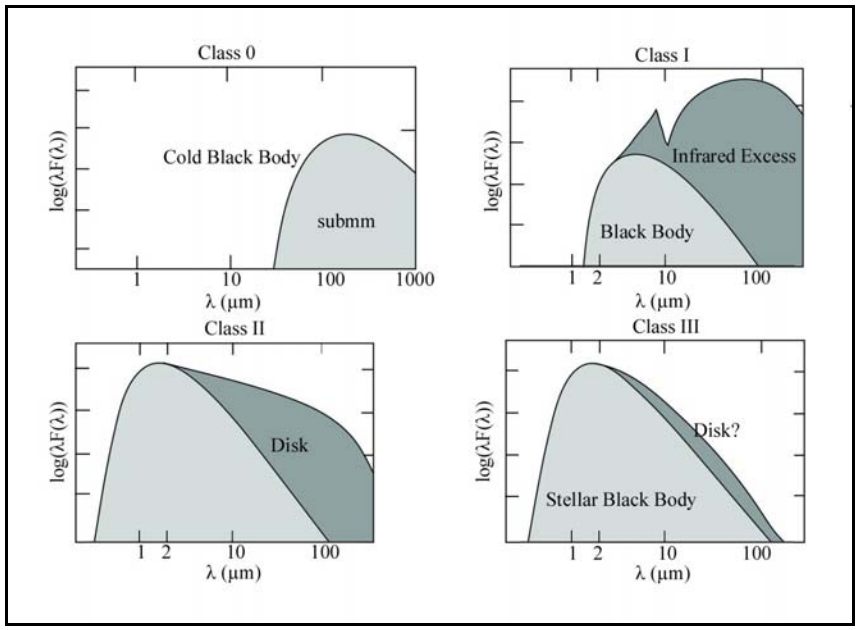


*Figure 2: SED shapes and classification for YSOs. Upper left: Class 0. Upper right: Class I. Lower left: Class II. Lower right: Class III.*

**Class 0** objects are stars in their main accretion phase with cold (20-30 K) blackbody spectra peaking in the sub-mm regime and are therefore not detected in the mid infrared. Instead they are often associated with highly collimated molecular outflows.

**Class I** objects show broader blackbody SEDs at 50-100K peaking at ~100 μm with an additional component at temperatures between 200-400K. As more and more of the inflowing matter falls onto the disk instead of the star, the molecular outflow weakens and becomes more poorly collimated as the outflow angle widens. The surrounding dust envelope is optically thick and absorption features from silicate grains at 10 μm can be seen.

**Class II** objects also display SEDs which are broader than single black-bodies, showing excess emission above that of a regular blackbody in the infrared. Most of the circumstellar material has been swept away and the excess radiation comes from circumstellar disks. The detailed shape of this excess depends on whether the disk is passive or active. Passive disks merely reprocess the radiation coming from the central stars, whereas active disks are massive disks kept hot by ongoing accretion and therefore have a an additional luminosity.

**Class III** objects represent stars which have shed their circumstellar material and disks. The SEDs consist of single black-bodies peaking at optical wavelengths, generally with a reddened stellar photosphere. These stars are usually pre-main sequence or young main sequence stars (Rathborne, 2003) (Shu et al, 1987).

The different stages of stellar evolution are also reflected in the slope of the SED defined by the spectral index $\alpha$ as

$$\alpha = -\frac{d \log \lambda F_\lambda}{d \log \lambda}, \quad (3)$$

and usually calculated between 2-20 μm. Class I objects have $0 < \alpha < 2$, Class II objects $-2 < \alpha < 0$, Class III objects $\alpha \sim 3$. (Rathborne, 2003).

## 4. Circumstellar Disks

When IRAS (Infrared Astronomical Satellite) flew as the first satellite able to observe far-IR radiation in 1983, it showed that some stars show excess radiation in the infrared above that expected by regular stellar photospheres. The orbits of the planets around the sun show low inclinations and eccentricities and this has long suggested that the Solar System formed from a dusty disk, or a circumstellar disk. These disks are the natural by-products of star formation, and some IRAS sources were found to be Class II pre-main sequence stars. The connection to star formation is confirmed by near-infrared observations of embedded populations and young stellar clusters, where ~80-85% of all stars show signs of circumstellar disks (Lada and Lada, 2003). Similar studies determine the lifetime for disks around stars to be relatively short, only ~3-15 Myr. The lifetime of circumstellar disks sets important constraints on models for the formation of planets. The timescale for how quickly disks disappear can be estimated by observing clusters of varying ages through infrared filters and counting the number of stars with and without infrared excess, assuming the cluster population to be co-eval, thus determining the cluster disk fraction (CDF). Observing clusters gives an advantage over studying single star forming regions, since significant sample of stars (hundreds) can be obtained with a not necessarily well known but at least equal mean age and by combining observations of embedded and revealed clusters, a significant range of ages can be covered. By observing very young clusters the initial disk fraction (IDF) can be estimated and the probability for new stars to form disks can be determined. Together with the probability for planet formation from circumstellar disks, this gives an indirect estimation of the number of extrasolar planetary systems in the Galaxy (Lada and Lada, 2003).

A number of studies have shown that observations in the JHKL broadband filters are optimal for determining the disk fraction (Rathborne, 2003), (Lyo et al, 2003), (Kenyon et al, 2001). Ground-based observations in the L-band can essentially detect all stars in our Galaxy with disks containing $\sim 10^{-9}$ $M_{sun}$ of hot dust or more by measuring the infrared excess coming from the disks (Lada and Lada, 2003). These observations are sensitive only to hot inner disks and it is possible that a large amount of disk material remains in the disk even after the inner disk has disappeared or cannot be detected. This would be the case if the dust grains have started to coagulate and form planetesimals, leaving mostly gas behind, since an equal amount of mass is much easier to detect when spread out in a dusty disk than when clumped together in larger bodies. However, studies show that the lifetimes of inner and outer disks are coupled and that therefore L-band observations can be used to determine the CDF, and hence estimate the disk lifetime (Lada and Lada, 2003).

An important question concerning circumstellar disks is the initial fraction of stars with disks (IDF). Does this number depend on the mass of the central star, the environment in which the star is forming or possibly both? What is the lifetime of disks and therefore the limit for planet formation and how does this depend on the stellar mass and environment?

In the past it has been difficult to address these questions, since the Earth's atmosphere makes observations in the infrared difficult or even impossible. L-band (3.5 μm) observations combined with shorter wavelength data (JHK bands, 1-2 μm) prove to be the best way of determining the disk fraction. However, sufficiently sensitive observations are necessary to sample the whole mass range of the stellar populations. Technological advances have made observations in the infrared possible by

combining more sensitive detectors with large telescopes. Access to sites with outstanding observing conditions, such as the Antarctica, make L-band observations possible with a sensitivity not achieved anywhere else on the planet.

Advances in technology have also made it possible to image disks around stars. One of the nearest known regions of recent star formation is the TW Hydrae Association (TWA) at an age of about 10 million years. Since the TWA is only ~60 pc from Earth it is possible to study the dusty disks around the stars in detail. For these sources the determination of disk properties is possible through direct imaging of the disks. One of the most interesting members is HR 4796 (figure 3), one of the dustiest stars in the bright star catalogue. Another very well imaged circumstellar disk is that of β Pictoris only 19.3 pc away.

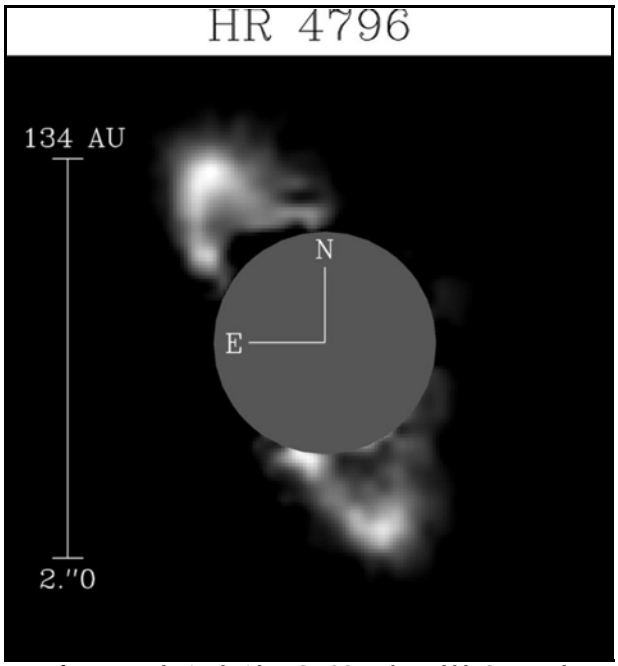


*Figure 3: Image of HR 4796 obtained with NICMOS on the Hubble Space Telescope at 1.1 µm. The region near the star is unusable and the area of the coronagraphic hole is indicated by the grey circle. The ring lies at about 150 AU (Schneider et al, 1999).*

Imaging circumstellar disks gives a range of information on disk properties. Typical disk radii are a few tens or hundreds of AU, although the disk around β Pic extends to over 1000 AU. The disks are made of dust and small amounts of gas. Some disks show structures in the form of gaps or rings (see ring in figure 3), which could be signs of bodies (planets or planetesimals) not discovered with our telescopes. Since these structures can be seen at relatively large distances from the stars, it is hard to explain the quick formation of planets in these regions. Another explanation for the observed structure is radiation pressure from the central star, blowing smaller dust particles and gas out of the system, while larger dust grains are subject to gas drag and Poynting-Robertson drag, concentrating smaller grains in a ring in the outer region of the gas disk and moving larger particles closer to the star until they evaporate (Brandeker, 2003).

Submillimetre observations show that single blackbodies with one grain temperature are not sufficient to characterize circumstellar disks and cooler grains at 200 K must be present. Since the flux from the disks mostly depends on the dust mass and not on the particle size, submillimetre measurements can also be used to determine the dust mass. The size of dust grains visible in observations range between 1µm to 1mm (Liseau et al, 2003). However, due to a lower surface-to-volume ratio, particles much larger than the wavelength of observation will have lower emissivity and are difficult to observe, so

larger grains are probably present. The larger grains might contain most of the mass, so mass determinations using submillimetre continuum flux can only give a lower bound on the dust mass in the disk. Keeping this in mind, measurements for stars just settling on the main sequence such as β Pic and HR 4796 give masses on the order of 0.5 Earth masses (Zuckerman, 2002), (Brandeker, 2003).

Whereas the dust around young stars most likely forms first generation disks from remnant particles from the molecular cloud in which the star is forming, disk lifetimes for β Pic for example are longer than the dust lifetime due to the Poynting-Robertson drag (Brandeker, 2003). The dust must therefore be renewed at a constant rate, forming second generation disks. These disks are generated by the breaking down of larger bodies into smaller particles, such as evaporation of comets or collisional erosions by kilometre-sized objects (Zuckerman, 2002), (Brandeker, 2003).

Circumstellar disks are believed to be the place for planet formation. The process of planet formation is however still poorly understood. Terrestrial planets probably form by dust particles sticking together and forming larger and larger bodies. The giant planets might have formed in a similar way, forming icy, solid cores similar to the way terrestrial planets were formed and then accreting the gas from the circumstellar disk onto these cores. Due to gas drag, the seeds of terrestrial planets will migrate to the inner part of the system, while the gaseous planets form in the outer parts where there are sufficient amounts of gas. Observations of planets around other stars however show the presence of massive planets close to the star. Also, the lifetimes of disks do not allow for the formation of large planets in the outer parts of the system (Beatty et al, 1999).

## 5. Infrared observations

Stars are formed in clouds of gas and dust and cannot be observed at optical wavelengths during most of their pre-main sequence evolution due to dust extinction. The energy released by collapse must be radiated away and this is done in the near-infrared (1-3μm) and optical (0.3-1μm) and is then absorbed by the surrounding dust and re-emitted in the thermal and far infrared (3-300μm) (Beckwith, 1994). The strong extinction in the visual therefore makes observations at these wavelengths relatively meaningless. A region totally opaque in the visual might be observable at infrared wavelengths, making it possible to see into the clouds where star formation is occurring. Further, the emission from YSOs peaks at infrared wavelengths, due to the radiative transfer in the surrounding dusty material, giving infrared observations an advantage over other wavelengths when searching for embedded young stars and measuring their luminosity. Hence, infrared observations are essential in examining the evolution and processes of stellar formation (Beckwith, 1994).

### 5.1. Extinction by dust

Dust grains in the interstellar medium or in a dusty envelope around the star will absorb the radiation from the star at short (mainly UV) wavelengths, re-emit it in the infrared and therefore redden the star. The interaction of small particles with radiation is characterized by the extinction efficiency $Q_e(\lambda)$ and the emittance. The extinction is a combination of absorption and scattering. However, for Rayleigh scattering $Q_s(\lambda) \sim \lambda^{-4}$ while for absorption $Q_a(\lambda) \sim \lambda^{-1}$. Absorption therefore plays the dominant role in extinction for almost all infrared radiation (Beckwith, 1994).

When looking at a star through a column of dust of optical depth $\tau_\lambda$, the flux will be reduced by

$$I(\lambda) = I_0(\lambda) e^{-\tau_\lambda}, \tag{4}$$

and the magnitude will be increased by an amount $\Delta m$. The increase in magnitude is called the extinction coefficient $A(\lambda)$ and depends on the wavelength (Emerson, 1996). The extinction is usually expressed by the extinction coefficient in the visual (0.55μm) $A_V$. In the near infrared $A(\lambda) \sim \lambda^{-1.7}$ and the extinction is stronger at shorter wavelengths, causing the stars to redden. The colour excess of a star is defined as the difference in the extinction coefficients at different wavelengths and it increases with increasing extinction, for example

$$(B\text{-}V)=(B\text{-}V)_0+A_B\text{-}A_V=(B\text{-}V)_0+E(B\text{-}V), \tag{5}$$

where $E(B\text{-}V)$ is the colour excess, $(B\text{-}V)_0$ the intrinsic colour of the star, $(B\text{-}V)$ is the observed colour, and $B$ and $V$ the magnitudes in the B- and V bands. The ratio $R$ of total to selective extinction $A_V/E(B\text{-}V)$ gives a measure of the amount of dust between the source and the observer.

The process responsible for infrared continuum emission is the thermal emission by dust grains heated by stellar radiation. The spectral energy distribution of thermal emission at uniform temperature from a single object is a Planck function dependent on the temperature T and the area A of the object

$$\upsilon F_\upsilon = \varepsilon(\upsilon) \frac{A}{D^2} \frac{2h\upsilon^4}{c^2} \frac{1}{e^{\frac{h\upsilon}{kT}} - 1}, \tag{6}$$

where $\varepsilon(\upsilon)$ is the emissivity, D the distance from the source and all other constants are the usual definitions. The peak IR emission corresponds to a temperature of a few hundred to a few thousand K. However, carbon particles will melt at about 1200 K and silicate particles at about 2000K resulting in no dust emission at wavelengths shorter than IR, hence always reddening the SED (Beckwith, 1994).

### 5.1.1. Interstellar reddening

All stars are observed through dust grains in the interstellar medium between the stars and are therefore reddened. The colour excess causes the stars to move along reddening vectors in colour-magnitude and colour-colour diagrams, determined by the amount of extinction at different wavelengths. If the intrinsic colour of a star is known the colour excess can be determined using (5) and if *R* is known the extinction coefficient can be determined and the extinction by interstellar dust can be corrected for (Christensen-Dalsgaard, 2000). It is often difficult to determine the exact extinction by interstellar dust, since the dust is not necessarily evenly distributed, resulting in more extinction towards parts of the source. Therefore reddening vectors showing the direction of reddening are plotted allowing for a range of extinction coefficients.

### 5.1.2. Infrared excess due to circumstellar disks

A star is said to have an infrared excess when the star shows a colour excess even after interstellar extinction has been taken into account. This excess radiation comes from intrinsic reddening due to dust around the stars and lifts the emission in the infrared above that expected from a stellar photosphere reddened by interstellar dust (figure 4). In the colour-colour diagrams these stars lie outside the region defined by the reddening vectors. These regions are generally occupied by Herbig Ae/Be stars or T Tauri stars and indicate the presence of circumstellar disks (Lada and Adams, 1992). The excess emission is measurable in the K-band at 2.2 μm making infrared excess detectable using JHK observations. However, this radiation may be caused by a circumstellar disk, the protostellar envelope or emission from HII regions and therefore JHK band observations alone may not be sufficient to determine the nature of the IR excess. L-band observations (3.5 μm) prove to be the ideal wavelength for detecting circumstellar disks. Compared to JHK colour-colour diagrams, the stars with IR excess are much more clearly separated in JHKL colour-colour diagrams. Additionally, the continuum emission from the stellar photosphere is strong enough in L-band to allow the determination of the number of stars with IR excess compared to the total number of stars in a given region, while it is still relatively easy to obtain L-band observations compared to far IR observations with the same sensitivities and spatial resolution as JHK band observations (Rathborne, 2003).

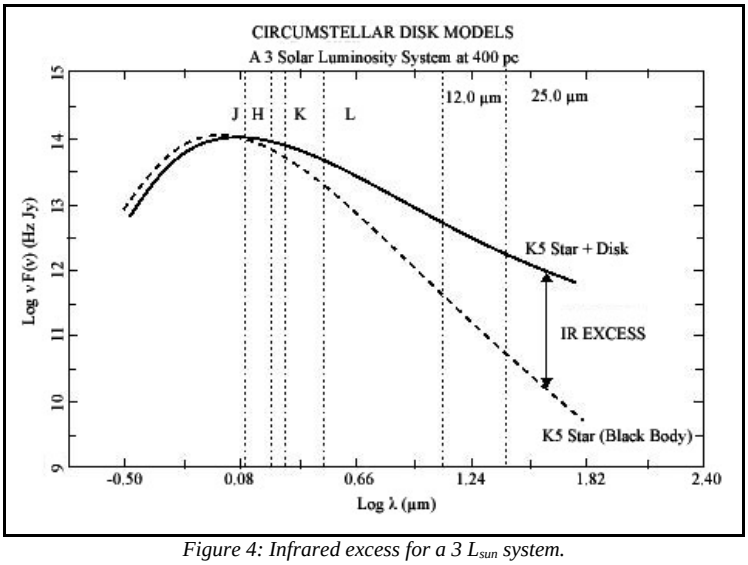


*Figure 4: Infrared excess for a 3 $L_{sun}$ system.*

### 5.2. Infrared observations from the Antarctica

The Antarctica is the coldest, driest and darkest place on Earth. Observations in the near-infrared (1-5 μm) are limited by the thermal background and air glow emission from OH radicals. Compared to temperate sites such as Mauna Kea the flux of the sky at the South Pole is reduced by order of about two magnitudes at 2.4 μm at typical temperatures during the winter of -60°C. The low thermal background makes longer observations in the 3-5 μm regimes much easier. Figure 6 shows the sky emission at Dome C on top of the Antarctic plateau compared to Mauna Kea (Dome C and the South Pole have similar conditions). Observations at these wavelengths are at the best difficult at most temperate sites. Due to the cold atmosphere, the amount of water vapour is of order 700 μm ppt $H_2O$ during the summer and 300 μm in the Antarctic winter. This compares to 1.2 mm on an excellent night on Mauna Kea. The low water vapour increases the transmission of the sky (figure 5 compares Dome C with Mauna Kea), giving most effect at mid-infrared and sub-mm wavelengths and to some degree in the near-infrared. Stable atmospheric conditions and negligible airflow caused by diurnal temperature variations give the best seeing on Earth (Burton et al, 1994). In addition to continuum emission these conditions give access to astrophysically interesting molecular lines such as those from polycyclic aromatic hydrocarbons (PAH).

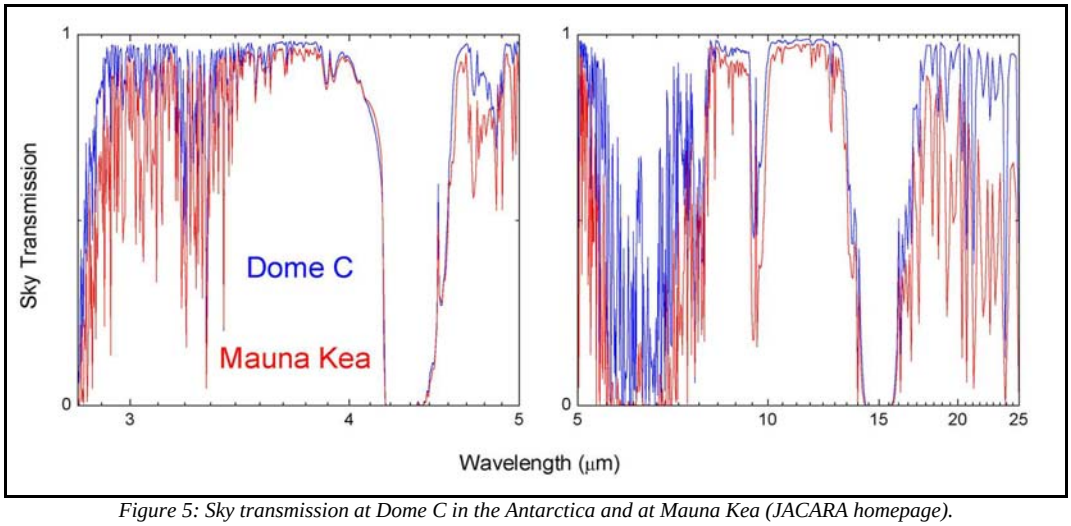


*Figure 5: Sky transmission at Dome C in the Antarctica and at Mauna Kea (JACARA homepage).*

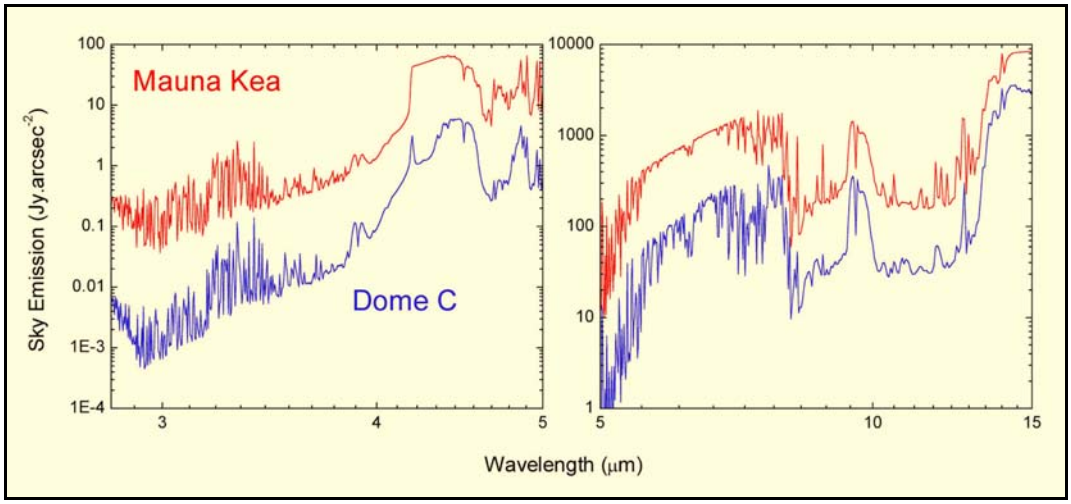


*Figure 6: Sky background at Dome C and Mauna Kea (JACARA homepage).*

### 5.3. Infrared detectors

Infrared radiation is detected by absorbing photons and thereby elevating an electron from a bound state to an unbound state within the semiconducting detector material. This unbound state is part of a series of continuum levels and allows the electron to migrate freely and therefore conduct electricity. The ion left behind by the electron can also move freely within the lattice. Recombinations of charges occur, adding noise to the signal. In hybrid detectors (also known as blocked-impurity-band (BIB) detectors) a thin layer of heavily doped semiconductor creates a high potential of photon generated charges. The rest of the detector material is undoped, providing a conduction band for charges. The blocking layer prevents recombinations and causes the detector to accumulate charges therefore producing a voltage across the detector. The accumulated charge can be read out before the detector is flushed. A multiplexer chip containing unit cells for each detector reads out and transfers the charges to external units. The unit cells are connected to the detectors through bump bonds, small electrical welds providing the mechanical and electrical connections between the detectors and the multiplexer. Individual unit cells are addressed through circuitry on the multiplexer chip.

One cycle consists of integration, read out and resetting the detector. While integrating, a voltage builds up within the unit cell. When read out, this voltage is amplified by an output amplifier and recorded by off-chip electronics. Which detector currently is read out is determined by the address register on the multiplexer. The unit cells read out the detectors non-destructively, making it possible to read out the accumulated charge several times during an integration cycle. This enables several different read out methods (see 'An overview of CASPIR below).

## 6. Observed regions

### 6.1. 30 Doradus

30 Doradus in the Large Magellanic Cloud is the most luminous giant HII region in the Local Group of galaxies and is located at a distance of ~ 50Mpc. The region shows recent and ongoing star formation at discrete epochs. The stellar population consists of multiple generations, with pre-main sequence stars, early type main sequence stars and evolved blue and red supergiants. Ages range from very young stars with ages of less than 1 Myr up to the giant population with ages up to 25 Myr. The location of the stars in near infrared colour-colour diagrams indicate a population of early-type stars seen through moderate foreground extinction ( $A_V$= 5 to 10 mag). However, there seems to be no low-mass cut-off for pre-main sequence stars giving the full range of spectral masses down to ~1.35 $M_{sun}$ (Brandner et al, 2001). Studies of near infrared colour-colour diagrams indicate the presence of Class I stars and T Tauri stars. Already earlier the identification of early O-type stars in nebular knots were taken as evidence for ongoing star formation. These knots are revealed to be compact multiple systems and are similar to star forming regions in the Galaxy such as the Trapezium system in the Orion Cluster. The present day star formation coincides with the distribution of the molecular gas or the interfaces of the gas with the central cavity created by the central cluster. The massive stars (with single stars with masses exceeding 100 $M_{sun}$) are located in the central region and it is suspected that this region is responsible for the bright filamentary arcs of nebulosity. Star formation possibly was triggered by the central cluster as well (Walborn, Blades, 1997). It is the nearest and therefore most highly resolved starburst region outside the Galaxy, thus making it an ideal source to study extragalactic star formation (Brandner et al, 2001). No direct evidence can be found indicating that 30 Doradus might form stars in a different way than stars are formed in the Galaxy. However, relative faintness, crowding and bright inhomogeneous nebulosity make observations difficult (Walborn and Blades, 1997).

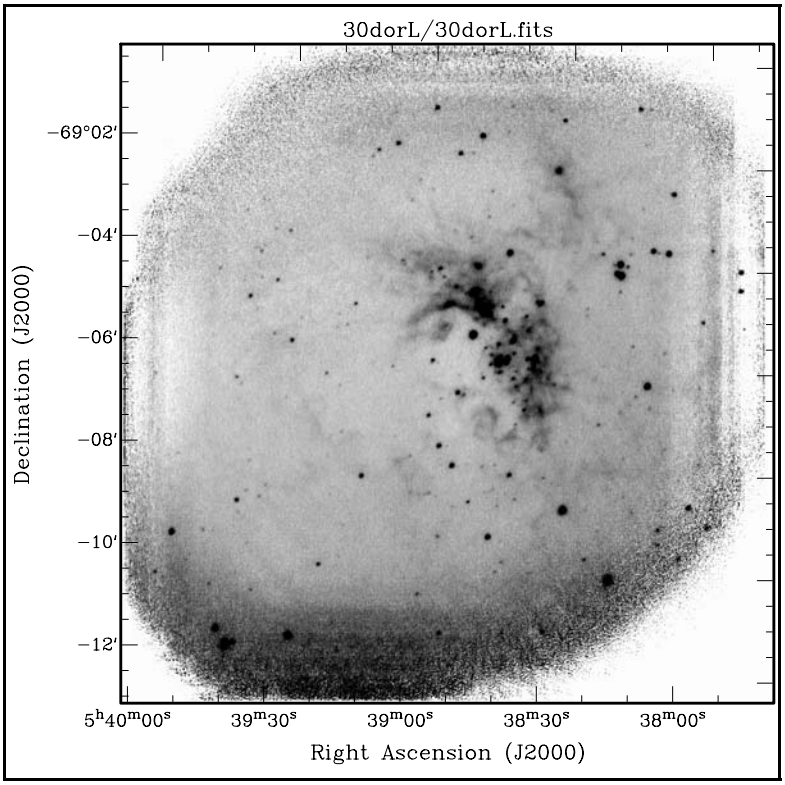


*Figure 7: L-band image of 30 Doradus from SPIREX.*

The images of 30 Doradus obtained with SPIREX are the most sensitive L-band images of this region ever made. This makes it possible to study the embedded stellar population and in combination with JHK data determine the number of stars with IR excess and therefore obtain information on the young stellar population in this region. Figure 7 shows the L-band SPIREX image of 30 Doradus. A total of 216 point sources were detected in the L-band.

### 6.2. RCW 57

This very young massive star forming region is one of the brightest HII regions in the infrared in our Galaxy. The distance to RCW 57 is not very well established. The kinematical distance was determined by Wilson et al in 1970 to be 3.6 kpc. However, kinematical distances are connected with large uncertainties and a distance of 2.4 kpc is obtained using the spectral information for HD97499 (Persi et al, 1994). RCW 57 is a very bright nebula with several dark globules and luminous arcs. Spectral energy distributions of the region indicate the presence of protostellar objects with silicate absorption features, therefore indicating Class I objects. JHK observations show that the majority of stars (>70%) have infrared excess (Persi et al, 1994). A large number of the stars found in the JHK bands are confined to the central area which confirms the extreme youth of the cluster (see figure 25). The massive stars are in the process of shredding the local molecular cloud they were formed in, destroying the cloud from the north-east to south-west (Figuerêdo et al, 2002). This indicates that star formation began in the north-eastern part of the cluster and is moving towards the south-west. The cluster population consists of A0-type stars and earlier. An older population is suspected of causing the bubbles and arcs seen at visual wavelengths in the northern part of the region. This population has however not been detected yet (Persi et al, 1994).

The L-band image from SPIREX reveals 279 point sources. As with 30 Doradus, this makes it possible to study the embedded population for infrared excess and draw conclusions on the fraction of stars with circumstellar disks. Especially the question whether high-mass stars form from disks and how their evolution depends on the stellar masses can be addressed. Figure 8 shows the SPIREX L-band image of RCW 57.

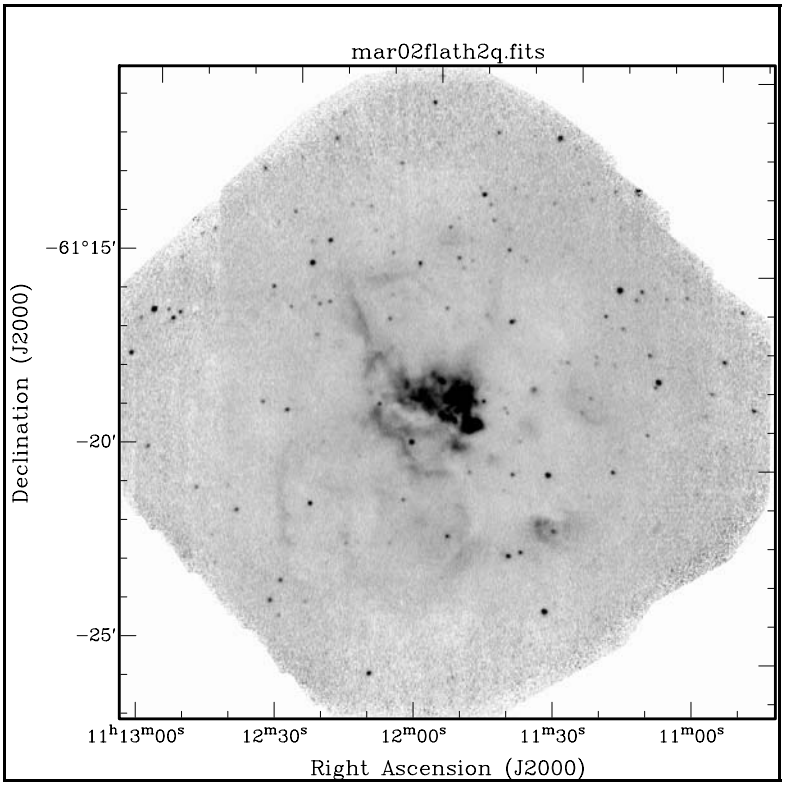


*Figure 8: L-band image of RCW 57 obtained by SPIREX.*

### 6.3. Galactic Centre

The core of the Galactic Centre is an extremely dense stellar cluster composed of both older red giants and young massive stars. Spectral examination of individual sources shows the presence of late-type giants and supergiants by the CO absorption feature at 2.3 µm. At the same time a group of OB stars is suspected to be ionizing the surrounding gas and producing the observed excitation of the gas. This requires a massive young population of stars in the Galactic Centre possibly formed in a starburst which occurred about 10 Myr ago. The examination of bright stars showing an IR-excess confirms an epoch of star formation less that 10 Myr ago. The special conditions of the Galactic Centre make it a unique region of star formation. Since the lifetime of massive stars is too short for them to move far from their birthplaces, a large amount of gas must have been delivered to and collapsed in the Galactic Centre (Blum et al, 1996).

The Galactic Centre is extremely hard to observe at visual wavelengths due to very high extinction. The SPIREX observations at 4.05 µm (figure 9) give a totally different picture of the Galactic Centre. Several bright sources are found, three of them in the nucleus located around the presumed nucleus Sgr A*. The high spatial resolution achieved with SPIREX makes it possible to identify objects at these wavelengths.

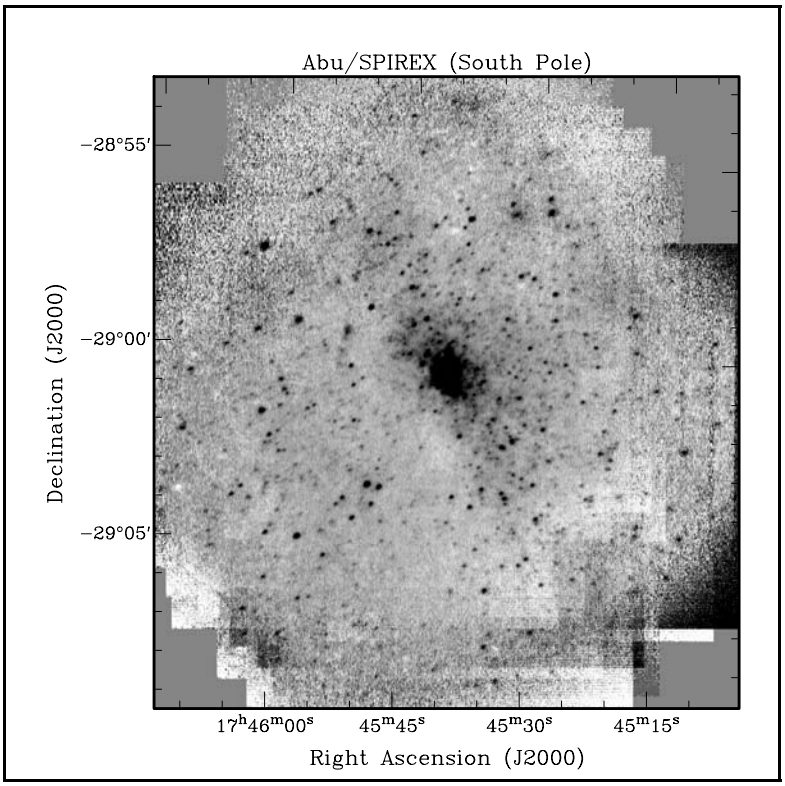


*Figure 9: SPIREX image of the Galactic Centre at 4.05 µm.*

### 6.4. RCW 38

RCW 38 is also a bright HII region in the Milky Way. It shows a very young embedded cluster of high-mass stars. In the near infrared extended nebulosity and dust lanes and dark patches can be seen. Photodissociation regions (PDRs) outline the regions where far UV-photons dissociate the molecular gas. Studying these regions gives important information on how the far-UV radiation effects star formation. PDRs can be traced by observing the 3.29 µm features from extended PAH emission. In RCW 38 many of these features coincide with the nebulosity and dust features in the near infrared. The SPIREX image of RCW 38 shows the extended PAH emission in this region (figure 10).

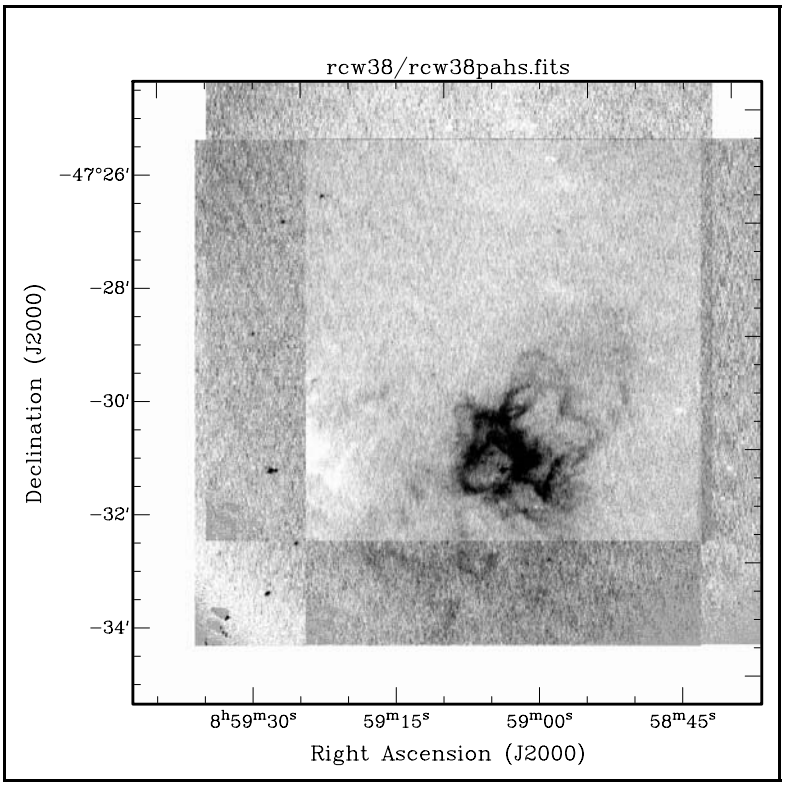


*Figure 10: SPIREX image of PAH emission in RCW 38.*

## PART 2: THE DATA

The following part describes the steps involved in finding circumstellar disks by detecting the IR-excess using JHK and L-band observations.

- **The data.** The SPIREX images provide the L-band and Br α magnitudes needed to detect the IR-excess. The JHK magnitude information from the 2MASS point source catalogue (PSC) is used to complete the longer wavelength data and to create colour-colour and colour-magnitude diagrams. The CASPIR data is used to calibrate the SPIREX images.
- **Reductions**. Only CASPIR data needed to be reduced, as the SPIREX and 2MASS data already had been reduced.
- **Data analysis**. Photometry was done on the SPIREX images and also on the 2MASS images to complement the point source catalogue.
- **Error estimation**. Errors were estimated for the photometry on the SPIREX and 2MASS images and for the calibration data from CASPIR.
- **Calibrations**. The SPIREX images were calibrated using the CASPIR data.
- **Sensitivity**. Sensitivity limits for the SPIREX images were determined.
- **Diagrams**. Combining the information from 2MASS and the SPIREX images colour-colour and colour-magnitude diagrams were created.

## 7. Observations

### 7.1. The SPIREX telescope

The 60 cm South Pole InfraRed Explorer (SPIREX) was built at the Amundsen-Scott South-Pole station in the Antarctica in 1994 to test the conditions for using an infrared telescope during the Antarctic winter. When SPIREX commenced operations it measured the thermal background, the transmission of the sky and the total time available for near infrared observations. The telescope was equipped with a grism imager (GRIM) camera and a 128x128 detector sensitive between 1-2.5 μm. In 1998 the telescope was upgraded to an Aladdin 1024x1024 InSb ABU detector sensitive in the range from 2.4 – 5 μm. The camera provided a 10' field of view with a pixel size of 0.6". Six science filters were offered with the SPIREX/Abu system (table 2). Three filters were optimized for observing the emission from molecular hydrogen (2.42 μm), PAHs (3.29 μm) and hydrogen line emission (Br α at 4.05 μm). Three broadband filters covered the L-, L'- and M-bands at 3.5, 3.8 and 4.7 μm respectively.

| *filter* | *Centre (μm)* | *width (μm)* | *range (μm)* | *time (s) x coadds* |
|---|---|---|---|---|
| $H_2$[a] | 2.425 | 0.034 | 2.408 - 2.441 | 360 x 1 |
| PAH | 3.299 | 0.074 | 3.262 - 3.336 | 60 x 3 |
| Br α | 4.051 | 0.054 | 4.024 - 4.078 | 10 x 18 |
| L | 3.514 | 0.618 | 3.205 - 3.823 | 6 x 30 |
| L' | 3.821 | 0.602 | 3.520 - 4.122 | 6 x 30 |
| narrow M | 4.668 | 0.162 | 4.586 - 4.749 | 1.2 x 90 |

*Table 2: Available filters for SPIREX/Abu and typical integration times x number of coadded frames per position. (Rathborne, Burton, 2003).*

During the 1999 season 38% of the total observing time was spent on L-band observations with an average of 9 reduced frames per day with 3.5 hours of on target time. More than 138 hours of L-band observations were made. Observations were done by taking one set of sky frames followed by two sets of object frames. Each set consisted of five averaged frames offset by approximately 30" from the previous frame. This allowed for the easy removal of image artefacts from the array and sky emission. Off-source background images were collected in a searchable database along with other information and used for dark subtraction and flat-fielding. Observations were carried out by the winter-over scientists Rodney Marks (1998) and Charlie Kaminsky (1999). Reductions were done automatically by the RIT SPIREX/Abu pipeline. Although observations of standard stars were obtained, these were not available for this thesis and the images had to be calibrated with observations made with the 2.3m telescope at Siding Spring (see below).

Using the quick look images from 2MASS, coordinate frames were fit to the SPIREX images of 30 Doradus, RCW 57, the Galactic Centre and RCW 38 using **koords** in the karma package. By marking the same stars in the reference image from 2MASS and the target image from SPIREX, **koords** uses the coordinate information in the reference image's fits header to calculate a coordinate system for the target image. This information is then written into the fits header of the target file. All coordinate frames were fit with a root mean square (RMS) pixel error of 0.3.

### 7.2. The Two Micron All Sky Survey (2MASS)

The infrared excess was detected using the JHK and L-band magnitudes of the detected stars. For the Galactic Centre a 4.05 μm image taken by SPIREX was used instead of L-band observations. The observations from SPIREX were complemented with the 2MASS point source catalogue (PSC) and Atlas images. The 2MASS project scanned the sky in both hemispheres in three near infrared filters (J, H and K, 1.25, 1.65 and 2.2 μm respectively) and detected point sources in each band which were brighter than about 1mJy using a pixel size of 2.0"/ pixel. 2MASS used two 1.3 metre telescopes located at Mt Hopkins in Arizona and at CTIO in Chile. The telescopes each used a camera capable of observing the sky in each band simultaneously using three channels. Each channel consisted of a 256x256 array of HgCdTe detectors.

The imaging was done while the highly automated telescopes scanned over the sky in declination at a rate of ~1' per second. The secondary mirror would scan in the opposite direction in order to freeze the image in the focal plane for 1.3 seconds, then move back to its original position and freeze a new piece of sky. The dead time required for moving back to the original position was less than 0.1s. The camera's field-of-view shifted 1/6 of a frame in declination between frames. The images consist of six pointings on the sky giving a total integration time of 7.8 seconds. Considering the dead-time, the 2MASS telescopes integrated for 84% of an observing night. The sensitivity limit for the J,H and K bands was 15.8, 15.1 and 14.3 magnitudes respectively with a photometric precision of 5% for unconfused point sources. The signal-to-noise ratio for sources in the PSC is greater than 10 in at least one of the bands. The position reconstruction error was 0.5". The Atlas images are tiles 6° long in declination and 8.5' wide (2MASS homepage). Both the images in form of quick look images and the PSC can be accessed through the 2MASS homepage. However, the quick look images are compressed images with a lower resolution and 2MASS does not recommend doing photometry on these images, as it will only be correct to an offset of about ±0.09 magnitudes. After examining and doing photometry on the images myself, a detailed analysis by 2MASS on this problem confirmed these results. The PSC gives the RA and DEC in degrees in J2000 of each source and the JHK magnitudes with corresponding error.

The reduction process and detection of point sources in the 2MASS PSC was done using an automated process and predefined selection criteria, such as detection in all 3 bands (JHK), limiting S/N criteria, artifact confusion and a minimum distance from the tile edge. Since some stars might have not been picked up by this automated routine, photometry was done on the compressed Atlas images to match SPIREX stars that did not match with the PSC.

## 7.3. CASPIR

In order to calibrate the SPIREX images, observations were carried out by Michael Burton and myself in early April using the MSSSO 2.3m telescope at Siding Spring Observatory equipped with CASPIR (Cryogenic Array Spectrometer/Imager).

The 2.3m telescope has an Alt-Azimuth mount and a primary mirror with a focal ration of f/2.05. The central hole has a diameter of 0.5m giving a total collecting area of 3.973m². The telescope was used in Cassegrain configuration with a 0.3m diameter secondary mirror with a focal length of f/7.87. The telescope is controlled using the Telescope Control System (TCS). At start-up configurations for infrared observations are loaded together with the standard star catalogue (MSSSO homepage, telescope user manual).

Siding Spring Observatory is not the ideal location for L-band observations. The background brightness measured in mag/arcsec$^2$ in 1997 at 3.6 μm was ~3.8. Based on the background flux, the 5 σ detection threshold for a one minute integration is 9.8 magnitudes with 1.5" seeing. All observed sources are brighter than this limit, making observations possible.

### 7.3.1. An overview of CASPIR

CASPIR is a cryogenic re-imaging camera with pixel scales of 0.5"/pixel and 0.25"/pixel and 5 different readout methods. It has a 50mm long and 10.4mm diameter collimated beam section. The camera is cooled by a closed cycle helium refrigerator. The camera body is cooled to ~60 K in the first stage and the detector array is cooled to ~32 K. The telescope beam gets redirected into the CASPIR dewar by a rotatable dichroic mirror in the instrument mount box. A gold-coated mirror then reflects the beam down parallel to the dewar axis. The aperture wheel is located directly below the mirror at the telescope focus and contains baffles for the 0.5"/pixel and 0.25"/pixel focal plane scales and slits for the grism. The beam then passes through a collimator lens into the collimated beam section. Next comes the upper filter wheel, the utility wheel, the lower filter wheel and the lens wheel. Each of the wheels contains 16 positions. The upper and lower filter wheel contain filters with the 3.6 μm continuum, 3.28 μm dust emission and Br α filters located in the lower filter wheel (table 3). To avoid saturation in the L-band, the narrow band filter had to be used. The utility wheel contains the $MgO/CaF_2$ doublet slow camera lens for the 0.25"/pixel focal plane scale and the lens wheel has the $MgO/BaF_2$ fast camera lens for the 0.5"/pixel focal plane scale. This is taken out of the beam if the 0.25"/pixel scale is used. Finally, the detector is located at the lower end of the dewar at the camera focus.

| *filter* | *centre (μm)* | *width (μm)* |
|---|---|---|
| PAH | 3.299 | 0.074 |
| L | 3.592 | 0.078 |
| 4.00 | 3.990 | 0.052 |
| Br α | 4.051 | 0.054 |

*Table 3: Filters used for calibration observations.*

The detector is a hybrid device with 256x256 pixels in which the detector material InSb is bump bonded to the multiplexer chip. Developed at Santa Barbara Research Centre (SBRC), it is capable of direct imaging and spectroscopy between 1-5 µm. The array has four output channels corresponding to four interlaced columns. To prevent saturation from the background flux, the smaller pixel scale had to be used when observing between 3-5 µm, resulting in a 60" field of view.

Similarly only the fastest readout method (method 1) can be used in order to avoid saturation due to the background. In this method only one sample per pixel is taken and referenced to the electrical ground. The unit cell is reset, integrated and sampled once every cycle. Readout method 2 reads the voltage twice, at the beginning of the cycle and at the end. Method 1 is subject to DC voltage drifts since the voltage difference is not measured, which is prevented in method 2. The voltage drift can be seen as a stripe pattern in the final image with a four pixel spacing (corresponding to four output channels). By taking images of clear sky regions this pattern can be defined and subtracted during data reduction. The shortest readout time for method 1 is 0.2s. The dominant noise source is shot noise from the photons and readout noise (~60 $e^-$) is not an issue. The detector array has a quadratic response to light that must be allowed for during data reduction before any other additive effects can be corrected. The data must be linearised which can be readily done using the reduction tools described below.

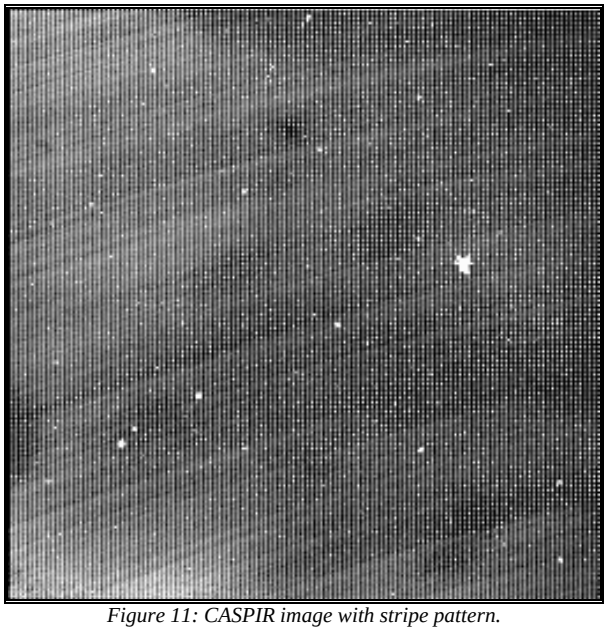

*Figure 11: CASPIR image with stripe pattern.*

CASPIR is controlled by typing DCL commands into the Control window. A status window shows system parameters for the filter wheels, readout method and readout time, and scrolls information on the bottom line. Two display screens are available. The idle display shows data taken using the idle parameters when no run is active, giving an almost real time image of the infrared sky. The idle loop is interrupted when real integrations start. The results of these are shown on the run display (McGregor, CASPIR user manual).

### 7.3.2. Observations

Source stars were chosen by picking bright, isolated stars in the SPIREX images. The number of sources for each field varied from three for RCW 57 to five for 30 Doradus (table 4). Two standard stars were chosen for each region from the list provided in the CASPIR manual (table 5).

| *source* | *RA (J2000)* (*h m s*) | *Dec (J2000)* (*d m s*) |
|---|---|---|
| RCW 57 id72 | 11 12 25.99 | -61 15 06.6 |
| RCW 57 id362 | 11 11 19.70 | -61 15 27.4 |
| RCW 57 id377 | 11 11 10.42 | -61 17 47.0 |
| 30 Doradus id163 | 05 38 10.09 | -69 03 42.4 |
| 30 Doradus id161 | 05 38 06.71 | -69 03 44.5 |
| 30 Doradus id179 | 05 38 09.63 | -69 06 20.8 |
| 30 Doradus id137 | 05 38 17.30 | -69 04 00.4 |
| 30 Doradus id160 | 05 38 06.30 | -69 02 34.5 |
| RCW 38 id719 | 08 59 26.80 | -47 26 07.0 |
| RCW 38 id363 | 08 59 29.95 | -47 31 01.7 |
| RCW 38 idcen | 08 59 05.70 | -47 30 41.3 |
| GC id1728 | 17 46 01.92 | -29 01 39.8 |
| GC id1063 | 17 45 57.12 | -29 04 51.3 |
| GC id1326 | 17 45 49.13 | -29 03 26.4 |
| GC id2918 | 17 45 38.23 | -28 56 29.3 |

*Table 4: Source list.*

| *region* | *standard* | *RA (J2000)* (*h m s*) | *Dec (J2000)* (*d m s*) | $m_L$ |
|---|---|---|---|---|
| RCW 57 | BS 4450 | 11 33 00.1 | -31 51 27 | 1.390 |
| | BS 4638 | 12 11 39.1 | -52 22 06 | 4.501 |
| 30 Doradus | BS 1983 | 05 44 27.8 | -22 26 54 | 2.415 |
| | BS 2015 | 05 44 46.5 | -65 44 08 | 3.711 |
| RCW 38 | BS 3842 | 09 38 01.4 | -43 11 27 | 3.354 |
| Galactic Centre | Y 4338 | 18 46 50.0 | -23 50 12 | 5.123 |
| | BS 7340 | 19 21 40.3 | -17 50 50 | 3.356 |

*Table 5: Standard stars.*

Observations were carried out between the 2nd and 8th of April at Siding Spring Observatory by myself and Steven Longmore who collected data for his own project which required similar observations. For the first two nights Michael Burton assisted and explained the use of the telescope.

At the beginning of each night the telescope's pointing was calibrated and the focus was set. Pointing was set by tracking a standard star and pushing the star into the middle of the idle display using the telescope's offset buttons. This procedure was repeated twice with the detector rotating 120° between each centring. The detector was then returned to its original position and the focus was set using the TCS and observing the shape of the star in the idle display. If necessary, the focus was re-set during the night.

Observations were carried out by running instruction files (".DO"- files). The instruction files define offsets, filters, readout method, integration time and the number of cycles over which should be integrated. Running the instruction file moved the telescope 12" north, integrated for the defined amount of cycles and integration time, then moved 12" south of the target and integrated for the same time resulting in a 'north' and 'south' image of the star. In general we observed first the standard stars and then the source stars, editing the necessary parameters in the .DO files to the correct filter and integration time. A number of sky, dark and bias frames were also obtained during each observing night. Table 6 lists which sources were observed on which days together with the number of n/s pairs (one pair gives 2 measurements for each star) and the integration time. All observations were made at 3.6 µm (L-band), except for the Galactic Centre where observations were also obtained through 4.00 and 4.05 µm filters and RCW 38 through the 3.28 µm filter. Standards were observed each night through the same filters as the source stars with 2 n/s pairs and total integration times of 60 *s*.

| *date* | *source* | *number of n/s* | *filter* | *integration time* |
|---|---|---|---|---|
| 2nd April | RCW 57 id72 | 2 | L | 200 x 0.3 |
| | RCW 57 id362 | 4 | L | 200 x 0.3 |
| | RCW 57 id377 | 4 | L | 200 x 0.3 |
| | GC id1063 | 2 | L, 4.00, 4.05 | 300 x 0.2 |
| | GC id1326 | 2 | L, 4.00, 4.05 | 300 x 0.2 |
| | GC id1728 | 2 | L, 4.00, 4.05 | 300 x 0.2 |
| | GC id2918 | 2 | L, 4.00, 4.05 | 300 x 0.2 |
| | RCW 38 id363 | 2 | L, 3.28 | 200 x 0.3 |
| | RCW 38 id719 | 2 | L, 3.28 | 200 x 0.3 |
| | RCW 38 idcen | 2 | L, 3.28 | 200 x 0.3 |
| 3rd April | nothing | - | - | - |
| 4th April | nothing | - | - | - |
| 5th April | 30 Doradus id 163 | 4 | L | 300 x 0.2 |
| | 30 Doradus id161 | 4 | L | 300 x 0.2 |
| | 30 Doradus id179 | 4 | L | 300 x 0.2 |
| | 30 Doradus id137 | 4 | L | 300 x 0.2 |
| | 30 Doradus id160 | 4 | L | 300 x 0.2 |
| 6th April | 30 Doradus id137 | 2 | L | 1000 x 0.2 |
| | 30 Doradus id179 | 2 | L | 1000 x 0.2 |
| | 30 Doradus id161 | 2 | L | 1000 x 0.2 |
| | RCW 57 id72 | 2 | L | 1000 x 0.2 |
| | RCW 57 id362 | 2 | L | 1000 x 0.2 |
| | RCW 57 id377 | 2 | L | 1000 x 0.2 |
| 7th April | 30 Doradus id161 | 2 | L | 1000 x 0.2 |
| 8th April | 30 Doradus id137 | 2 | L | 1000 x 0.2 |
| | 30 Doradus id179 | 2 | L | 1000 x 0.2 |
| | 30 Doradus id161 | 2 | L | 1000 x 0.2 |

*Table 6: Dates when different sources were observed together with number of n/s pairs and integration time per image. No data was obtained on 3rd and 4th of April due to bad weather. The integration time was increased to improve the signal to noise ratio.*

Due to bad weather data could not be collected during the nights of the 3rd and 4th of April. A quick look at the data showed that the images obtained on 2nd of April were good enough to work with. However, I tried to collect additional data on RCW 57 with longer total integration time to increase the signal-to-noise ratio. Unfortunately clouds passed over during the observations and this data was useless. The data for 30 Doradus collected on the 5th of April was equally useless and I obtained data with longer integration times on the following nights. Weather conditions were not always very stable and I therefore pointed to 30 Doradus more often than the other sources to make sure I had usable data in all observed regions.

### 7.3.3. Reductions

The CASPIR data was reduced using the MSSSO CASPIR package in IRAF (Image Reduction and Analysis Facility). Specifically the **redimage** task is a convenient tool to do most of the image reductions, such as linearising, sky subtracting, destriping and combining the images. However, dark and bias frames were created by combining the individual frames using the task **imcombine**.

The data is linearised in the **redimage** task by first subtracting a linearised bias frame, applying the quadratic correction, subtracting the dark frame, converting the units from ADUs to electrons and dividing by the exposure time to get a signal rate in electrons/sec. The task is run on a list of file names which contains all the images with the same exposure time. Next the north and south images are subtracted from each other, resulting in a final image with a positive star in the upper part and a negative star in the lower part of the image. This results in automatic sky subtraction between the images. At the same time the **redimage** task defines the striping pattern caused by the readout of the detector (see above) and destripes the image. The final images are then multiplied with -1 to get images where the lower star is positive and the upper star is negative.

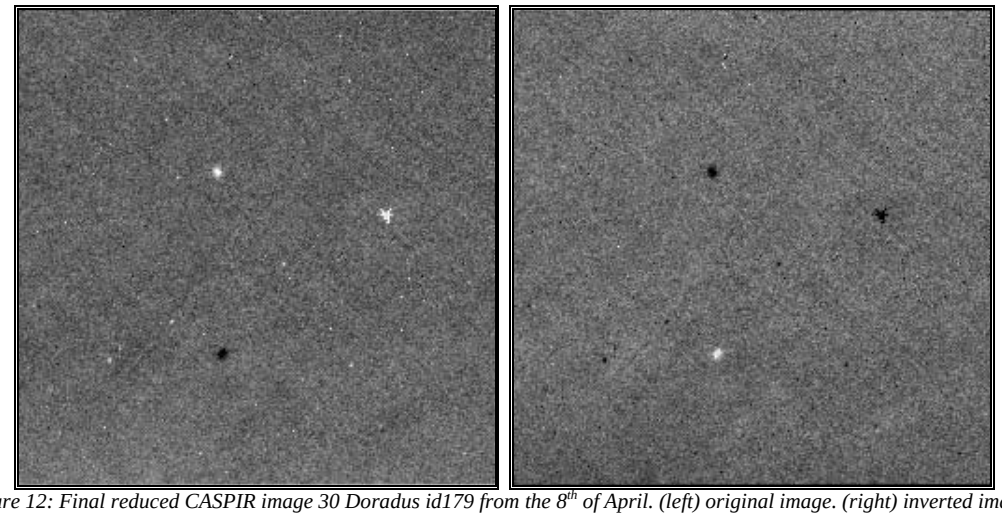

*Figure 12: Final reduced CASPIR image 30 Doradus id179 from the 8th of April. (left) original image. (right) inverted image.*

# 8. Data analysis

## 8.1. The IRAF/daophot package

The photometry and data analysis were the same for 30 Doradus, RCW 57 and the Galactic Centre. The analysis of the PAH emission of RCW 38 was somewhat different and is described at the end of this chapter.

Photometry on the images was done using the **IRAF/daophot** package in IRAF. The package is based on and uses the same tasks and algorithms as the DAOPHOT package written by Peter Stetson of the Dominion Astrophysical Observatory for stellar photometry in crowded fields. The tasks allow the user to interactively examine, select and deselect stars using the image display. According to the parameters the user enters, the procedure automatically finds stars, selects model stars and calculates a point spread function (psf), fits the psf to all the stars and calculates the magnitudes. The tasks and parameter files used are described in the following.

### 8.1.1. Tasks and parameters within the IRAF/daophot package

- **daoedit**: this task is used together with the image display to obtain basic information about the image properties. By selecting different stars in the image, **daoedit** fits a Gaussian to the data and displays a radial profile. The information given together with the profile includes the full width at half maximum (FWHM), the sky background level and the sky variation $\sigma_{sky}$.

- **tvmark**: enables the user to mark the stars in the output lists from the various tasks on the image display.

- **datapars**: contains the parameters defining the image properties obtained using **daoedit**. Scale units for the FWHM, sky annulus and fitting parameters are defined. Image header keywords, noise characteristics, and minimum and maximum good data values can also be defined.

- **centerpars**: contains the information used by the **phot** aperture photometry task (see below). Here the centring algorithm and width of the data used to compute the centres of the stars are defined. However, the parameters here are not critical since the stars are re-centred using non-linear least squares fitting techniques during the psf fitting process.

- **fitskypars**: contains the parameters used for the sky fitting algorithms in the **phot** task. Important parameters are the sky fitting algorithm and the radius and width of the sky annulus. Although the option to refit the sky exists later in the process, it is important to get a good sky fit early on, since those values are used when calculating and fitting the psf.

- **photpars**: defines the aperture photometry parameters used in the **phot** task. Magnitudes are measured through an aperture size defined here and are relative to the zero point given here.

- **daopars**: sets the parameters for the psf computation. The radius over which the psf is defined and the radius over which the psf will be fit are defined here.

- **setimpars**: saves all the parameters entered into the parameters files in a text file so that they can be re-loaded at a later time.

- **daofind**: This task reads the input parameters from the **datapars** algorithm parameters, and asks the user to verify values for the FWHM, $\sigma_{sky}$, detection threshold in units of $\sigma_{sky}$ and minimum and maximum good data values. It then computes the amplitude of the best-fitting Gaussian with the given FWHM at every point in the image and searches for maxima above the detection threshold.

The approximate centres in pixel coordinates in the image, magnitudes, shape statistics and ids for the found stars are then written to the output star list.

- **phot**: The **phot** task reads the parameter values from the **datapars**, **centerpars**, **fitskypars** and **photpars** parameter files and asks the user to verify the most important of the values. **phot** computes the exact centres for the stars using the information from **centerpars**, fits the sky background using the parameters in **fitskypars** and calculates a preliminary magnitude by determining the total number of counts in an area defined by the aperture size and correcting for the sky background. A magnitude error is also calculated. However, the right keywords for integration time and gain must be entered. These were not available in this case, so the calculated errors had to be checked using the **addstar** task (see below). The output of the **phot** task is a photometry file including the positions of the stars, their ids, magnitudes and magnitude errors.

- **pstselect**: The psf fitting algorithms need bright, isolated stars distributed over the whole image to use as model psf stars. **pstselect** reads the information from **datapars** and **daopars**, reads the information from the phot output files, sorts the stars in order of increasing magnitude so that the brightest stars are in the beginning of the list and selects the *n* brightest, non-saturated stars where *n* is a user defined number of stars. These stars are written to the output file as candidate psf model stars.

- **psf**: The **psf** task computes the psf model used by all subsequent psf photometry fitting tasks. It reads the x and y coordinates, magnitudes and sky values for the candidate psf stars and displays them in an image display. The user can look at a surface plot, radial profile or contour plot of the stars and accept or reject them as psf models. It then computes the constant analytic component of the psf model specified by a 2D elliptical Gaussian function aligned along the x and y axes of the image using data within the psf fitting radius defined in **daopars**. The results are weighted proportional to the signal-to-noise ratio for each psf star and non-linear least-square fitting techniques. It then determines the residuals of each psf star and creates the psf model look-up table. The computed analytic function and look-up table are written to the output psf image. Finally stars within a defined radius of psf stars are identified as neighbours and stars in the vicinity of psf star neighbours are defined as friends of neighbours. The coordinates, magnitudes, sky values and ids of the psf stars are written to the output star list, the psf stars, neighbours and friends of neighbours are written to the output psf star group file.

- **nstar**: To check the accuracy of the psf model computed in the **psf** task, the current model can be fit to the psf stars and their neighbours using the **nstar** task.

- **substar**: Using the output photometry file from the **nstar** task, **substar** subtracts the psf stars and their neighbours from the image. The subtracted image is displayed and the user can examine the quality of the psf model. The psf stars should subtract cleanly out of the image and there should be no systematic patterns around the stars or hidden neighbours behind the stars.

- **allstar**: The **allstar** task reads in all the task parameters, the input image, input photometry file and psf model. It then groups the stars into groups with a defined maximum number of stars, subtracts the current best-fit psf model, performs a weighted, non-linear least squares fit to the data within the fitting radius and computes new x and y coordinates and magnitudes for each star in each group. Every four iterations it writes the id, x and y coordinates, sky value, magnitude and magnitude error, number of iterations to fit the star, chi and sharpness statistics of stars which met the convergence criteria to the output star list. The output list contains the final positions, ids, and magnitudes and magnitude errors used for the colour-colour diagrams. A subtracted output image is also produced, making it possible to examine the psf fitting.

- **wcsctran**: uses the image header information to convert the pixel coordinates to degrees.

- **addstar**: This tasks adds artificial stars whose positions and magnitudes are defined by the user to the image using the calculated psf model from the **psf** task.

- **tmatch**: matches the rows of one table with the rows of another table. This task is used to match the coordinate files from the photometry with the **IRAF/daophot** package with the 2MASS point source catalogue. Rows are only matched if they are closer to each other than a user defined distance. The distance between two rows is defined as the square root of the sums of the squares of the difference between each column.

- **ttables**: The package **ttables** contains various tasks to manipulate tables.

### 8.2. A typical analysis sequence

Doing photometry on the SPIREX and 2MASS images followed the same steps in the analysis sequence. In general I started with the parameter values suggested by the **IRAF/daophot** user manual and then-fine tuned them to get the optimal results. The parameter files for each region are listed in appendix C.

1) Load image into the image display, in this case ds9.

2) Use **daoedit** to examine the image and star properties, measuring the sky level, FWHM and $\sigma_{sky}$ for approximately 10 stars.

3) Enter the parameter values for FWHM, $\sigma_{sky}$ and minimum data value (dependent on sky level) into **datapars.**

4) Enter parameters into **centerpars** (size of centring box), **fitskypars** (radius and width of sky annulus, type of sky fitting algorithm), **photpars** (aperture size), **daopars** (radius over which the psf is defined and fitting radius for the psf) and **findpars** (detection threshold).

5) run **daofind**. The edges of the SPIREX images are very noisy, causing the star finding algorithm to be very unreliable in that region. To avoid this, the stars that could be seen in the edge regions on the image display were marked, **daofind** was run and the results were displayed on the image with **tvmark.** Then the stars in the inner parts of the image that had been found with **daofind** and the ones marked in the edge regions were selected running **daofind** interactively.

6) Run **phot** using the results from **daofind** creating a photometry file with initial coordinates and magnitudes for all stars.

7) Create a list of model stars to compute the psf model using **pstselect**. In general **pstselect** was set to choose 15 stars.

8) Display psf stars on the image display and run **psf** in interactive mode so stars which should be used as psf stars can be chosen from the output list from **pstselect**. Each star is examined by looking at its surface plot, contour plot and radial profile. Only isolated stars away from crowded regions and bright nebulosity are chosen (this was not possible in all cases for the Galactic Centre).

9) Compute the psf model using **psf**.

10) Group the psf stars and check the psf model using **nstar**.

11) Subtract the psf stars from the image using **substar**.

12) If the image looks good (i.e. no patterns or hidden neighbours where the psf stars were), **allstar** is run to fit the psf model to all stars and get the final star list with x and y coordinates, magnitudes, and magnitude errors.

13) Transform the x and y coordinates to degrees using the image header information and the **wcsctran** task, giving a final output file with the position in degrees, the magnitude, magnitude error and the id for each star.

### 8.3. Error estimation

#### 8.3.1. SPIREX images

As mentioned above correct values for the noise characteristics of the image are needed for the **IRAF/daophot** package to produce correct errors. These were not available in this case and another way of estimating the error had to be found. This could be done by using the **addstar** task and adding a number of artificial stars with known position and magnitude to the image. Then the same analysis sequence as described above could be done on the artificial image using the same parameters and psf model as for the original image. The resulting magnitudes for the artificial stars could then be compared with their true magnitudes to get an estimate of the real error. In the case of 30 Doradus 220 stars with magnitudes between 14.5 and 8 were added to the image. 172 of these ended up with measured magnitudes (figure 14). For RCW 57 210 stars with magnitudes between 13 and 7 were added with measured magnitudes for 105 of these (figure 15). In the case of the Galactic Centre 115 stars between 12 and 4 magnitudes were added with measured magnitudes for 76 of these (figure 16). The number of artificial stars added is less for the Galactic Centre, since the region analysed for the Galactic Centre only covered the inner 2.5' of the SPIREX image. In the case of 30 Doradus, the same analysis was also run for 3 different sets of psf stars and compared to the results using the "first choice" psf stars in order to see how the choice of psf stars affected the magnitude (figure 13).

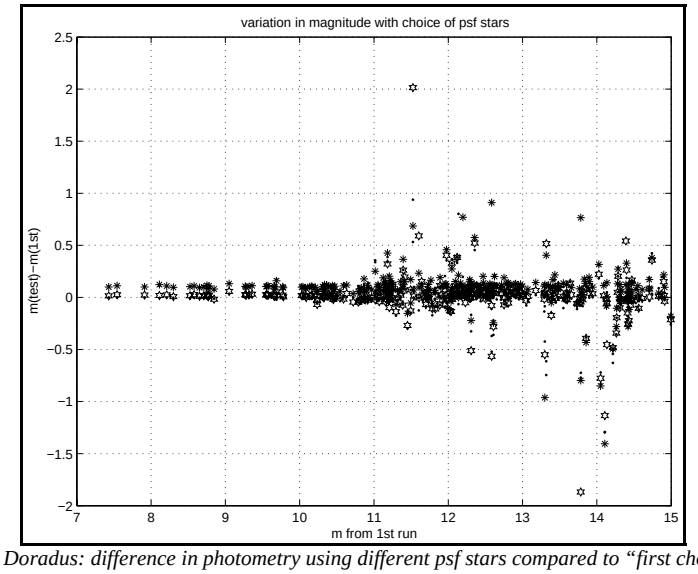


*Figure 13: 30 Doradus: difference in photometry using different psf stars compared to "first choice" psf stars.*

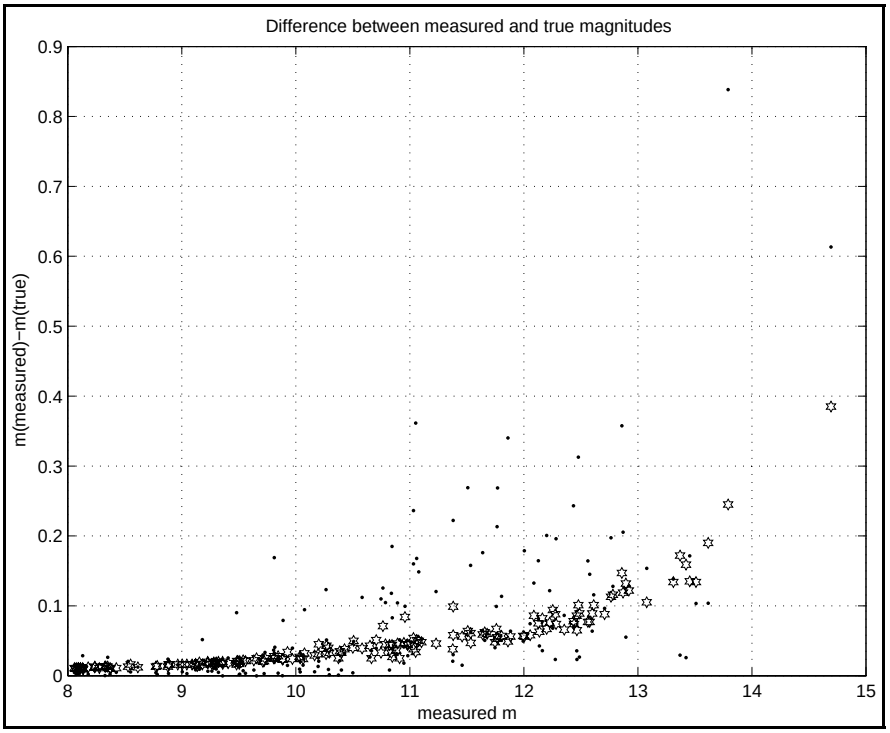


*Figure 14: 30 Doradus: Absolute values of the difference between measured and true magnitudes for 172 stars vs measured magnitudes (dots). Star shaped symbols are the errors given by the photometry by the **IRAF/daophot** package.*

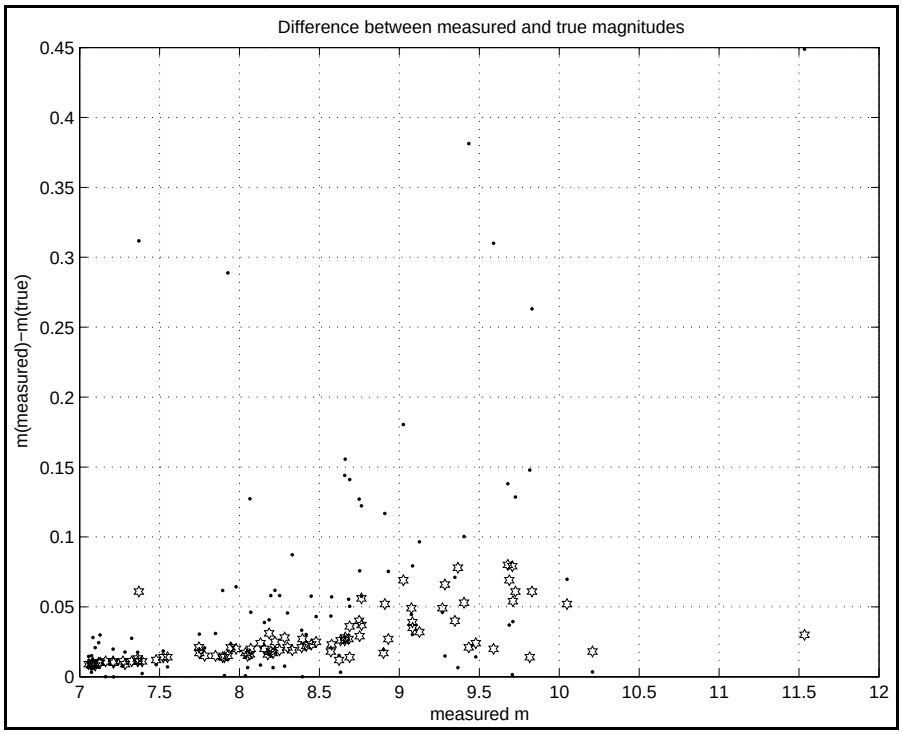


*Figure 15: Absolute values of the difference between measured and true magnitudes for 105 stars vs measured magnitudes (dots) for RCW 57. Star shaped symbols are the errors given by the photometry by the **IRAF/daophot** package.*

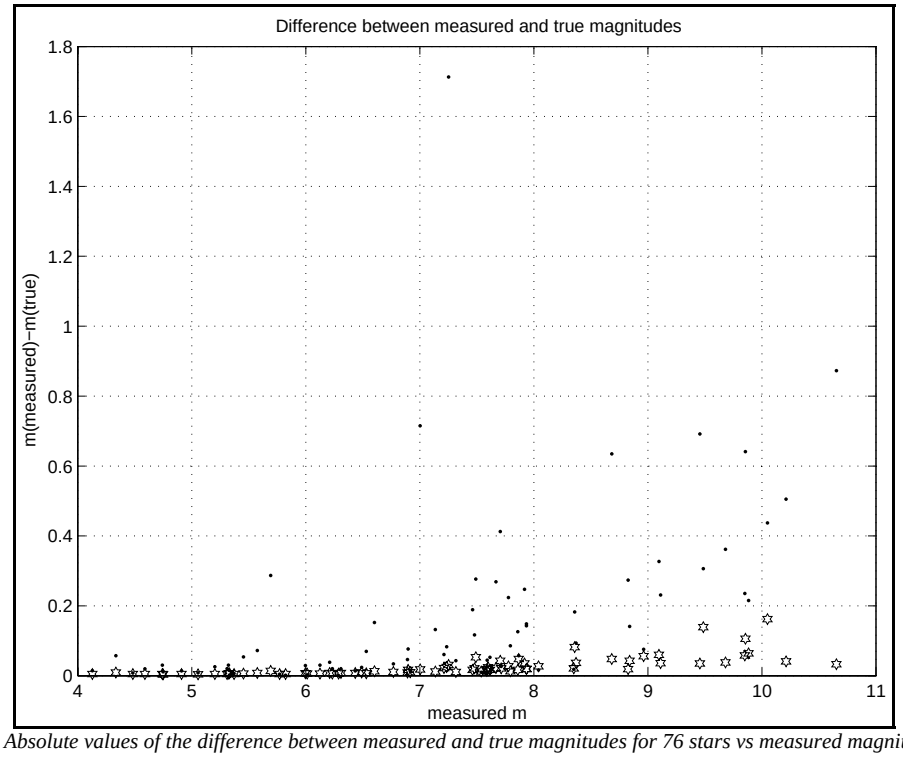


*Figure 16: Absolute values of the difference between measured and true magnitudes for 76 stars vs measured magnitudes (dots) for the Galactic Centre. Star shaped symbols are the errors given by the photometry by the **IRAF/daophot** package.*

The figures show that the errors given by the photometry in IRAF (star shaped symbols) follow the spread in magnitudes. Large deviations between the measured magnitude and the true magnitude have been examined using **imexam** by plotting radial profiles and surface contours and can be explained as being due to bad pixels, crowded stars (this applies especially to the Galactic Centre) and bad measurements due to the noisy edge regions of the SPIREX images. For subsequent analysis the error given by **IRAF/daophot** photometry was taken to be the true error.

### 8.3.2. 2MASS

The 2MASS image headers contained the information necessary to calculate the correct errors during the photometry process. However, since the photometry was done on the compressed images, the results were compared with the PSC, plotting the difference between the PSC magnitudes and the magnitudes obtained with IRAF. This was compared to an extensive analysis on photometry on the compressed images done by 2MASS and available on their homepage.

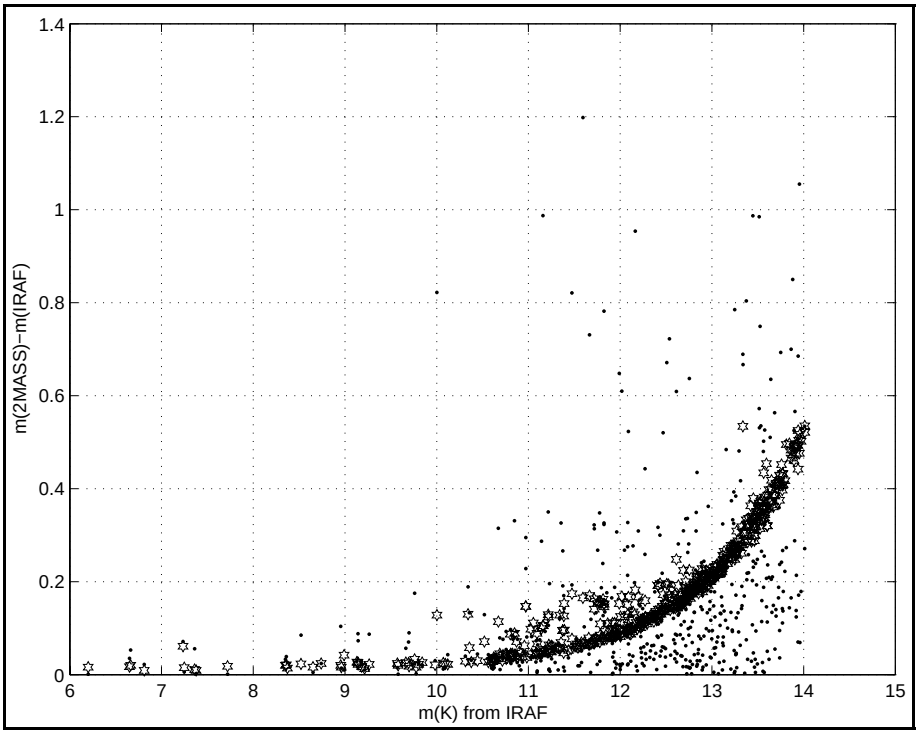


*Figure 17: Absolute values of difference between the 2MASS K-band magnitude and the magnitude from the compressed K-band images vs $m_K$ obtained with IRAF. Star shaped symbols are the errors given by the photometry in IRAF.*

Figure 17 shows an example of photometry done on a 2MASS K-band image covering part of the 30 Doradus field. After comparing these results with the 2MASS homepage the errors determined by the IRAF/daophot package (star shaped symbols) were used as the real errors.

### 8.4. Calibration

The magnitudes calculated using the IRAF/daophot package are only relative to an arbitrary zero point (ZP). The images must therefore be calibrated by determining the zero point correction. This was done using the CASPIR data. The ZP correction is a constant correction for all stars and once the difference between CASPIR magnitudes and SPIREX magnitudes is determined for a few stars, all other stars can be calibrated by adding the ZP correction.

The reduced CASPIR images were examined using **imexam**. A Gaussian was fit to the data and displayed as a radial plot. Depending on the shape of that fit it was decided whether the data should be included or not. Due to weather conditions, a number of frames did not show anything and had to be discarded. Bad radial profiles were also not taken into account in the subsequent calibration. In general all standard stars gave good images, although to ensure similar sky backgrounds, only the standard closest to the source was used for calibration.

Some of the source stars were found in frames of other source stars close by, giving additional measurements for some stars. For 30 Doradus source stars 163 and 161 were in the same frames. In the Galactic Centre the image of star 1326 contained the additional star 1310 and star 2918 also contained star 2853. The final data used after sorting out the unusable data is listed in table 7 together with the observation date and the total amount of measurements obtained for that source.

| *date* | *source* | *filter* | *measurements* |
|---|---|---|---|
| 2nd April | RCW 57 id72 | L | 4 |
| | RCW 57 id362 | L | 6 |
| | RCW 57 id377 | L | 4 |
| | GC id1063 | L | 4 |
| | GC id1326 | L | 4 |
| | GC id2918 | L | 2 |
| | GC id1310 | L | 4 |
| | RCW 38 idcen | L | 3 |
| 6th April | 30 Doradus id137 | L | 4 |
| | 30 Doradus id134 | L | 4 |
| 8th April | 30 Doradus id137 | L | 4 |
| | 30 Doradus id134 | L | 4 |
| | 30 Doradus id135 | L | 4 |
| | 30 Doradus id161 | L | 4 |
| | 30 Doradus id179 | L | 4 |

*Table 7: Final observations used for calibration.*

Using **imexam** I fit a Gaussian profile to the data and measured the total flux in counts in a circular aperture around the star. **imexam** automatically centres the profile and subtracts a sky value determined by fitting the sky in an annulus around the star. Doing this for the standard stars and the source stars gives their counts $C_{std,i}$ and $C_{source,i}$, respectively. The unweighted average of all measurements for each star is calculated with corresponding error $\Delta C$. The magnitude of the standard stars $m_{std}$ is known from the CASPIR manual and this gives for the calibrated magnitude of the source

$$m_{cali} = -2.5 \log \frac{C_{source,i}}{C_{std,i}} + m_{std} \,. \tag{7}$$

The error is given by error propagation

$$\Delta m_{cali} = \frac{2.5}{10} \sqrt{\left(\frac{\Delta C_{source}}{C_{source}}\right)^2 + \left(\frac{\Delta C_{std}}{C_{std}}\right)^2} \,. \tag{8}$$

The calibrated CASPIR magnitudes can now be compared to the magnitudes obtained for the SPIREX images. Displaying these in a diagram with the calibrated magnitude vs SPIREX magnitudes, the data should ideally lie on a straight line with inclination = 1. A weighted least-squares fit to a straight line is done to check the quality of the results (figures 18-20). By taking the difference $m_{diff}$ between the calibrated magnitude $m_{cali}$ and the SPIREX magnitude $m_{SPIREX}$, the ZP correction for each individual star is determined.

$$m_{diff,i} = m_{cali,i} - m_{SPIREX,i} \,, \tag{9}$$

$$\Delta m_{diff,i} = \sqrt{\left(\Delta m_{cali,i}\right)^2 + \left(\Delta m_{SPIREX,i}\right)^2} \,. \tag{10}$$

The overall ZP correction is given by the weighted average of all measurements of $m_{diff}$

$$ZP = \frac{\Sigma w_i m_{diff,i}}{\Sigma w_i} . \quad (11)$$

The error in the weighted average is

$$\Delta ZP = \frac{1}{\sqrt{\Sigma w_i}} , \quad (12)$$

and the weight $w_i$ is given by

$$w_i = \frac{1}{\Delta m_{diff,i}} . \quad (13)$$

Figures 18 to 20 show the $m_{cali}$ vs $m_{SPIREX}$ for 30 Doradus, RCW 57 and the Galactic Centre respectively. Results are shown in tables 9 to 11. The SPIREX image for the Galactic Centre was taken at 4.05 μm (Br α). Unfortunately, due to very low signal-to-noise ratio, **imexam** could not get fits on the data obtained with CASPIR at 4 μm and 4.05 μm and the data was not usable, so the calibrated L-band (3.5 μm) magnitudes had to be extrapolated to 4.05 μm. Table 8 shows the JHK magnitudes for four stars from 2MASS, their calibrated L-band magnitude from CASPIR and the magnitude at 4.05 μm ($m_{4.05}$) after linear extrapolation from the K and L-band magnitudes. Table 12 shows the resulting ZP corrections for the three regions. All L-band and 4.05 μm magnitudes were then corrected for the ZP.

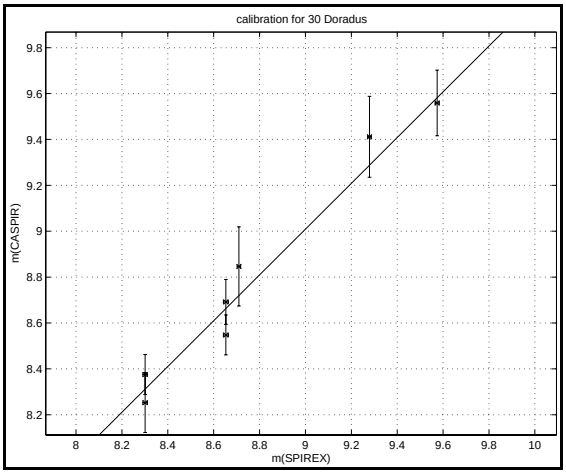


*Figure 18: 30 Doradus. $m_{CASPIR}$ vs $m_{SPIREX}$ with straight line fit to the data.*

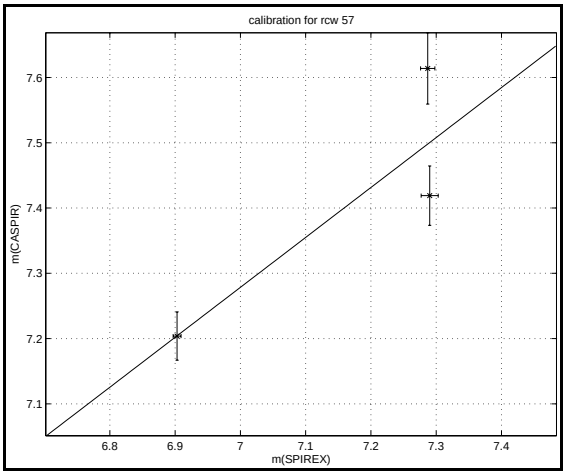


*Figure 19: RCW 57. $m_{CASPIR}$ vs $m_{SPIREX}$ with straight line fit to the data.*

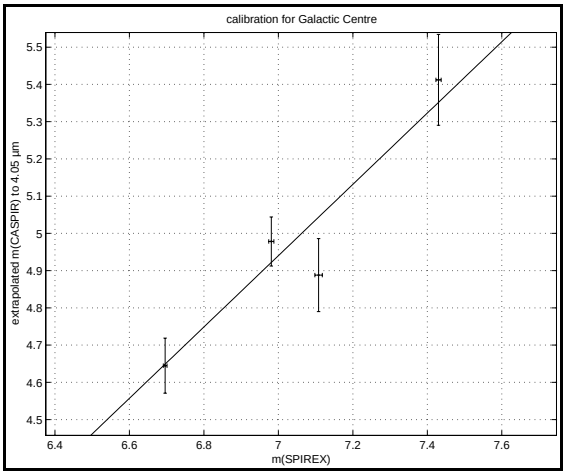


*Figure 20: Galactic Centre. $m_{CASPIR}$ vs $m_{SPIREX}$ with straight line fit to the data.*

| *source* | $m_J$ | $m_H$ | $m_K$ | $m_L$ | $m_{4.05}$ |
|---|---|---|---|---|---|
| GC id1063 | 6.45 ±0.02 | 5.44±0.05 | 4.98±0.02 | 4.98±0.06 | 4.98±0.07 |
| GC id1326 | 12.38±0.03 | 8.43±0.03 | 6.38±0.01 | 5.02±0.07 | 4.64±0.07 |
| GC id1310 | 8.15±0.02 | 6.54±0.02 | 5.84±0.02 | 5.51±0.12 | 5.41±0.12 |
| GC id2918 | 14.81±0.06 | 10.64±0.04 | 8.27±0.03 | 5.63±0.09 | 4.89±0.1 |

*Table 8: Extrapolation to 4.05 µm for sources in the Galactic Centre. JHK magnitudes are from the 2MASS point source catalogue, L magnitude is calibrated from CASPIR.*

| *source* | $m_{cali}$ | $m_{SPIREX}$ |
|---|---|---|
| 30 Doradus id137 | 8.69±0.1 | 8.65±0.01 |
| 30 Doradus id137 | 8.55±0.09 | 8.65±0.01 |
| 30 Doradus id134 | 8.38±0.09 | 8.30±0.01 |
| 30 Doradus id134 | 8.25±0.13 | 8.30±0.01 |
| 30 Doradus id135 | 9.56±0.14 | 9.57±0.01 |
| 30 Doradus id161 | 9.41±0.18 | 9.28±0.01 |
| 30 Doradus id179 | 8.85±0.17 | 8.71±0.01 |

*Table 9: Calibrated magnitudes and SPIREX magnitudes for 30 Doradus.*

| *source* | $m_{cali}$ | $m_{SPIREX}$ |
|---|---|---|
| RCW 57 id377 | 7.42±0.05 | 7.29±0.01 |
| RCW 57 id362 | 7.20±0.04 | 6.90±0.01 |
| RCW 57 id72 | 7.61±0.05 | 7.29±0.01 |

*Table 10: Calibrated magnitudes and SPIREX magnitudes for RCW 57.*

| *source* | $m_{cali}$ | $m_{SPIREX}$ |
|---|---|---|
| GC id1063 | 4.98±0.07 | 6.98±0.01 |
| GC id1326 | 4.64±0.07 | 6.70±0.01 |
| GC id1310 | 5.41±0.12 | 7.43±0.01 |
| GC id2918 | 4.89±0.1 | 7.11±0.01 |

*Table 11: Calibrated magnitudes and SPIREX magnitudes for the Galactic Centre.*

| *source* | *ZP correction* | *inclination* |
|---|---|---|
| 30 Doradus | 0.01±0.04 | 1.0±0.11 |
| RCW 57 | 0.25±0.03 | 0.77±0.13 |
| Galactic Centre | -2.05±0.04 | 0.96±0.18 |

*Table 12: ZP correction and inclination of the straight line fit to the data.*

### 8.5. Sensitivity

Looking at the background variation $\sigma_{sky}$, it is possible to get an estimate of the sensitivity of the images. Assuming a detection threshold of three $\sigma_{sky}$, the total number of counts $C_{3\sigma sky}$ in a typical area used to determine the flux of a star compared to the number of counts $C_{star}$ for a star with known magnitude gives a limiting magnitude. The radius over which the psf was fit was taken to be the typical radius for a star *(psfrad*). This gives

$$C_{3\sigma_{sky}} = 3 \cdot \sigma_{sky} \sqrt{\pi \cdot psfrad^2} \ , \tag{14}$$

and for the limiting magnitude

$$m_{3\sigma_{sky}} = 2.5 \log \frac{C_{star}}{C_{3\sigma_{sky}}} + m_{star} \ . \tag{15}$$

Values for $\sigma_{sky}$, *psfrad*, $C_{star}$, $m_{star}$ and resulting sensitivities are given in table 13.

| *source* | $\sigma_{sky}$ *(counts)* | *psfrad (pixels)* | $C_{3\sigma sky}$ *(counts)* | $C_{star}$ *(counts)* | $m_{star}$ | $m_{limit}$ |
|---|---|---|---|---|---|---|
| 30 Doradus | 2 | 14 | 148.89 | 7351 | 9.23 | 13.5 |
| RCW 57 | 7 | 13 | 414.75 | 29478 | 7.32 | 11.95 |
| Galactic Centre | 10 | 35 | 1146.42 | 34482 | 4.93 | 8.6 |

*Table 13: Values used to determine the sensitivity limit of the SPIREX images.*

### 8.6. Matching the two star lists

The final step before making colour-colour and colour-magnitude diagrams is to match the SPIREX star lists with the 2MASS PSC. The SPIREX star lists contain ids, $RA_{SPIREX}$, $Dec_{SPIREX}$, $m_{SPIREX}$ and $\Delta m_{SPIREX}$. The PSC has the RA, Dec and JHK magnitudes.

The lists were matched using **tmatch** in the **ttables** package in IRAF. The rows of each table were matched comparing the RA and Dec simultaneously. Rows were matched and written to the output list if the distance between two rows was less than a defined value *r*. The distance was determined to be the square root of the sum of the squares of the distance between the two columns

$$dist = \sqrt{\left(RA_{PSC} - RA_{SPIREX}\right)^2 + \left(Dec_{PSC} - Dec_{SPIREX}\right)^2} \ , \tag{16}$$

meaning that a star in the SPIREX list would be matched with a star in the PSC if it lay within radius *r* of the PSC star. **tmatch** produces an output star list which combines selected columns from both lists. The final star list contains RA, Dec, JHK-band magnitudes with error, SPIREX magnitudes with error and ids. In addition a diagnostic output file is produced listing all the stars not matched in the first list, stars that were matched more than once and the ten stars with the largest norm. Stars that were matched twice or more often were inspected visually to decide which match was the correct one.

Initially the lists were matched with a 1" radius (*r*=1"). However, a large number of stars that had obvious matches in all bands were for some reason not matched. When overlaying and blinking the SPIREX images with K-band images from 2MASS, one could see how the stars did not overlay. This was true for most parts of the images, except for the area that was used to match the coordinate systems. The problem persisted if the coordinate system was matched using a different area of the SPIREX image. If the whole SPIREX image was used to try and match a coordinate system, no decent

fit could be achieved. Finally it was concluded that since the SPIREX images are mosaics of many smaller images, parts of the images must have been fit poorly to the coordinate system when making the mosaic. This resulted in wrong coordinates for the stars in the SPIREX images when transforming the pixel coordinates to RA and Dec. The difference was significant, up to 4" for parts of the images. An attempt was made to fit several different coordinate systems to the different areas in the images and to treat these separately, matching each area with the PSC first and later combining the lists. However, since the SPIREX images contain a large number of individual images it was impossible to reconstruct the areas that belonged together. The problem was finally solved by matching the lists at a 1" radius and confirming the matches visually by overlaying the images and blinking between them. The matched stars were then taken out of the star list to ensure they would not be matched again. The remaining L-band stars were then matched with the PSC at 1.5" and matches were again confirmed visually. This step was repeated up to a radius of 4" where all obvious matches were found.

The Galactic Centre region is so crowded that it was impossible to tell whether stars were being matched correctly or not. Since in the case of the Galactic Centre the central region is of main interest, only a region roughly 2.5'x2.5' around the centre was considered.

Even after matching stars at a 4" radius, a number of stars were found in the SPIREX images that did not have a match in the PSC. These stars were matched with the star lists from the photometry on the 2MASS K-band images, making it possible to put these into the colour-magnitude diagrams. Matching the lists was done the same way as matching with the PSC including the visual confirmation of matches to allow for the wrong coordinates in the SPIREX images. Stars that still did not match with any star in K-band were written to a separate list.

The final lists contain the following columns:

1) PSC matched with SPIREX star lists:
$RA_{PSC}$, $Dec_{PSC}$, $m_{J,PSC}$, $\Delta m_{J,PSC}$, $m_{H,PSC}$, $\Delta m_{H,PSC}$, $m_{K,PSC}$, $\Delta m_{K,PSC}$, $m_{SPIREX}$, $\Delta m_{SPIREX}$, $id_{SPIREX}$.

2) Photometry on 2MASS K-band images matched with SPIREX star lists:
$RA_{PSC}$, $Dec_{PSC}$, $m_{K,im}$, $\Delta m_{K,im}$, $m_{SPIREX}$, $\Delta m_{SPIREX}$, $id_{SPIREX}$.

3) SPIREX stars without match:
$RA_{SPIREX}$, $Dec_{SPIREX}$, $m_{SPIREX}$, $\Delta m_{SPIREX}$, $id_{SPIREX}$.

### 8.7. Analysing the image of RCW 38

The SPIREX image of RCW 38 was taken at 3.299 µm to map the emission of polycyclic aromatic hydrocarbons (PAHs). Besides the bright central star, only very few stars can be seen in the image and therefore no photometry was done on this image. Instead the calibrated magnitude of the central star was determined as for the sources in the other SPIREX images (equation 7 and 8). Only the L-band magnitude could be measured since the other images obtained with CASPIR could not be used (table 7). The central star was matched with the PSC and the magnitude at 3.29 µm was determined by linearly extrapolating from the L-band and K-band magnitudes (table 14).

| *source* | $m_K$ | $m_{PAH}$ | $m_L$ |
|---|---|---|---|
| RCW 38 idcen | 6.53± 0.007 | 6.38± 0.07 | 6.34 ± 0.07 |

*Table 14: Linear extrapolation to 3.29 µm.*

The fluxes $F_0$ for a 0 magnitude star in units $Wm^{-2}\mu m^{-1}$ are given in table 15. The flux at 3.29 µm is linearly extrapolated from the K- and L-band fluxes. One count in the image corresponds to a flux $F_{count}$ given by

$$F_{count} = F_0 \cdot 10^{-\frac{m_{count}}{2.5}}, \tag{17}$$

and $m_{count}$ is given by

$$m_{count} = 2.5 \log \frac{C_{cen}}{C_{count}} + m_{cen} = 2.5 \log C_{cen} + m_{cen}, \tag{18}$$

where $C_{cen}$, $C_{count}$ and $m_{count}$ are the counts for the centre star, one count in the image and the magnitude corresponding to one count respectively. The final result is multiplied with the bandwidth (0.074 µm for the 3.29 µm filter used with SPIREX) to give the flux in $Wm^{-2}$.

| *band* | *centre (µm)* | *bandwidth (µm)* | *flux ( $Wm^{-2}\mu m^{-1}$)* |
|---|---|---|---|
| K | 2.2 | 0.4 | $3.8\ 10^{-10}$ |
| PAH | 3.29 | 0.074 | $1.1\ 10^{-10}$ |
| L | 3.6 | 0.6 | $6.9\ 10^{-11}$ |

*Table 15: Fluxes for 0 magnitude star.*

The flux corresponding to one count in the SPIREX image is therefore

$F_{count} = 6.12\ 10^{-19}\ Wm^{-2}$.

This makes it possible to draw a contour map of the intensity of the PAH emission and compare it to the K-band image.

### 8.8. Results

Table 16 gives the number of stars found and matched in the different wavelength bands for 30 Doradus, RCW 57 and the Galactic Centre. The total number of stars found in the SPIREX images is listed under *total*. Stars matched with the PSC and hence found in all four bands are listed under *PSC*. Stars only found in the SPIREX images and 2MASS K-band images are listed under *K*. All stars only found in the SPIREX images are listed under *SPIREX*. Of the stars that did not match, only stars brighter than the sensitivity threshold of the image were counted. The resulting lists with magnitudes at all wavelengths where available are listed in appendix B.

| *source* | *total* | *PSC* | *K* | *SPIREX* |
|---|---|---|---|---|
| 30 Doradus | 216 | 165 | 27 | 24 |
| RCW 57 | 279 | 213 | 16 | 50 |
| Galactic Centre | 91 | 55 | 28 | 8 |

*Table 16: Results of photometry on SPIREX images and matched lists.*

## 9. Analysis of results

### 9.1. Colour-colour diagrams

Colour-colour diagrams have proven to be a very effective way of identifying IR-excess. As described above, IR-excess is an indicator for circumstellar disks and colour-colour diagrams therefore give information about the amount of stars with disks. In particular, L-band observations combined with data at shorter wavelengths make it possible to estimate the total amount of stars with disks compared to the total amount of stars in the region, hence determining the disk fraction.

Colour-colour and colour-magnitude diagrams were created using the 2MASS JHK magnitudes and the SPIREX magnitudes. Using the intrinsic (V-K), (J-K), (H-K) and (K-L) colours of the main sequence and giant stars (Koornneef, 1983) and their visual magnitudes $M_V$ (Allen, 1973), the locations of the main sequence (spectral types O6-8 to M5) and the giant branch (spectral types K0 to M5) were plotted in all diagrams. For the colour-magnitude diagrams the apparent magnitude *m* for the main sequence and giant branch at the distance *d* (in pc) was calculated using the distance modulus

$$m = M + 5\log\frac{d}{10}. \tag{19}$$

### 9.2. Interstellar reddening

To see how reddening due to extinction from interstellar dust would affect the main sequence and the giant branch, reddening vectors were plotted in all diagrams. Assuming that the extinction in the near infrared is proportional to $\lambda^{-1.7}$, this gives for the extinction coefficients $A(\lambda_{JHKL})$ in the JHK and L-bands

$$\frac{A_V}{A(\lambda_{JHKL})} = \left(\frac{\lambda_V}{\lambda_{JHKL}}\right)^{-1.7}, \tag{20}$$

where $\lambda_{JHKL}$ is the wavelength in the centre of the JHK and L-bands, respectively, $\lambda_V$ is the visual wavelength (550 *nm*) and $A_V$ is the visual extinction coefficient. The reddened colours are then given

by adding the difference between the respective extinction coefficients.

### 9.3. 30 Doradus and RCW 57 – Infrared excess

Figures 21 to 23 show colour-colour and colour-magnitude diagrams for 30 Doradus and RCW 57 using the JHKL magnitudes from the 2MASS and SPIREX images. The thick solid curve shows the main-sequence for stars of spectral types O6-8 to M5 and the thin solid curve the giant branch for types between K0 and M5. The dashed curve shows the reddening vector up to $A_V$=30. A large number of stars in the JHKL diagram lie well outside this reddening vector, indicating a larger amount of extinction than that due to interstellar dust. Therefore, all stars which lie at least 1σ to the right of the reddening band in the JHKL plane are defined to have an IR-excess and are marked with the star symbol. Then the number of stars that lie a 2σ distance to the right of the reddening vector is calculated. The variation of the number of stars to the right of the reddening band when assuming 1σ and 2σ distances is taken as an estimate of the uncertainty of stars with IR-excess. Table 17 lists the number of stars found with IR-excess. Stars defined to have an IR-excess in the JHKL plane are marked with the same symbol in the other diagrams as well. In the colour-magnitude diagrams, stars with diamond shaped symbols are stars only found in the 2MASS K-band image and the SPIREX image. Stars with circle symbols are stars found only in the SPIREX image. Since the 2MASS project had a sensitivity limit of 14.3 magnitudes in K-band, this gives a limit on where stars only found in the SPIREX image could lie. Since $m_K$ for these stars must be ≥ 14.3, stars with circles will have the same or redder colours than displayed (i.e. they would move to the right in the diagram). Error bars show the average uncertainties for all stars.

The colour-magnitude diagrams show where the stars only detected in K- and L-bands lie. For RCW 57 all of these stars occupy the same region as the stars with an IR-excess, indicating that these too have an IR-excess. In fact, when inspecting the stars visually, it was found that these stars for the most part lie within the nebulous regions of the image. This is also seen for those stars which were only found in the SPIREX images. When determining the disk fraction, these stars were taken to have an IR-excess. For 30 Doradus a few of the stars only detected in K- and L-bands or not matched at all are located outside the region occupied by stars with an IR-excess and were not counted as having excess. For both regions, stars that lie within the region occupied by stars with an IR-excess are counted towards the total disk fraction.

| *source* | *JHKL (1σ)* | *JHKL (2σ)* | *KL (1σ)* | *KL (2σ)* | *L (1σ)* | *L (2σ)* | *total (1σ)* | *total (2σ)* | *fraction* |
|---|---|---|---|---|---|---|---|---|---|
| 30 Doradus | 53 | 49 | 19 | 19 | 20 | 16 | 94 | 84 | 43.5±4.6% |
| RCW 57 | 126 | 121 | 14 | 14 | 50 | 50 | 190 | 185 | 68.1±1.8% |

*Table 17: Sources with IR excess for 30 Doradus and RCW 57 at 1 σ and 2 σ distances to the right of the reddening band. Sources found in in all four bands are listed under JHKL, sources only found in K- and L-bands are listed under KL. Sources only found in L-band are listed under L. The total disk fraction is calculated using the total number of stars detected in each region.*

The majority of the stars in the colour-magnitude diagram for 30 Doradus (figure 23) are located above the main sequence, meaning that these stars are brighter than O6-8 type stars (the sensitivity threshold of the SPIREX image is at 13.5 magnitudes, only ~0.2 mag fainter than where O6-8 stars would be located). Massey and Hunter detect a large amount of O3V type stars in the 30 Doradus cluster (Massey and Hunter, 1998). Other studies find a significant amount of supergiants and giants (Walborn and Blades, 1997; Bosch et al, 1999; Parker, 1993). The location of supergiants between B0 and M0 is drawn in the 30 Doradus CMD in figure 23 as the upper thick solid line above the main sequence. Of the four papers on the stellar population quoted here, unfortunately, only Parker gives coordinates.

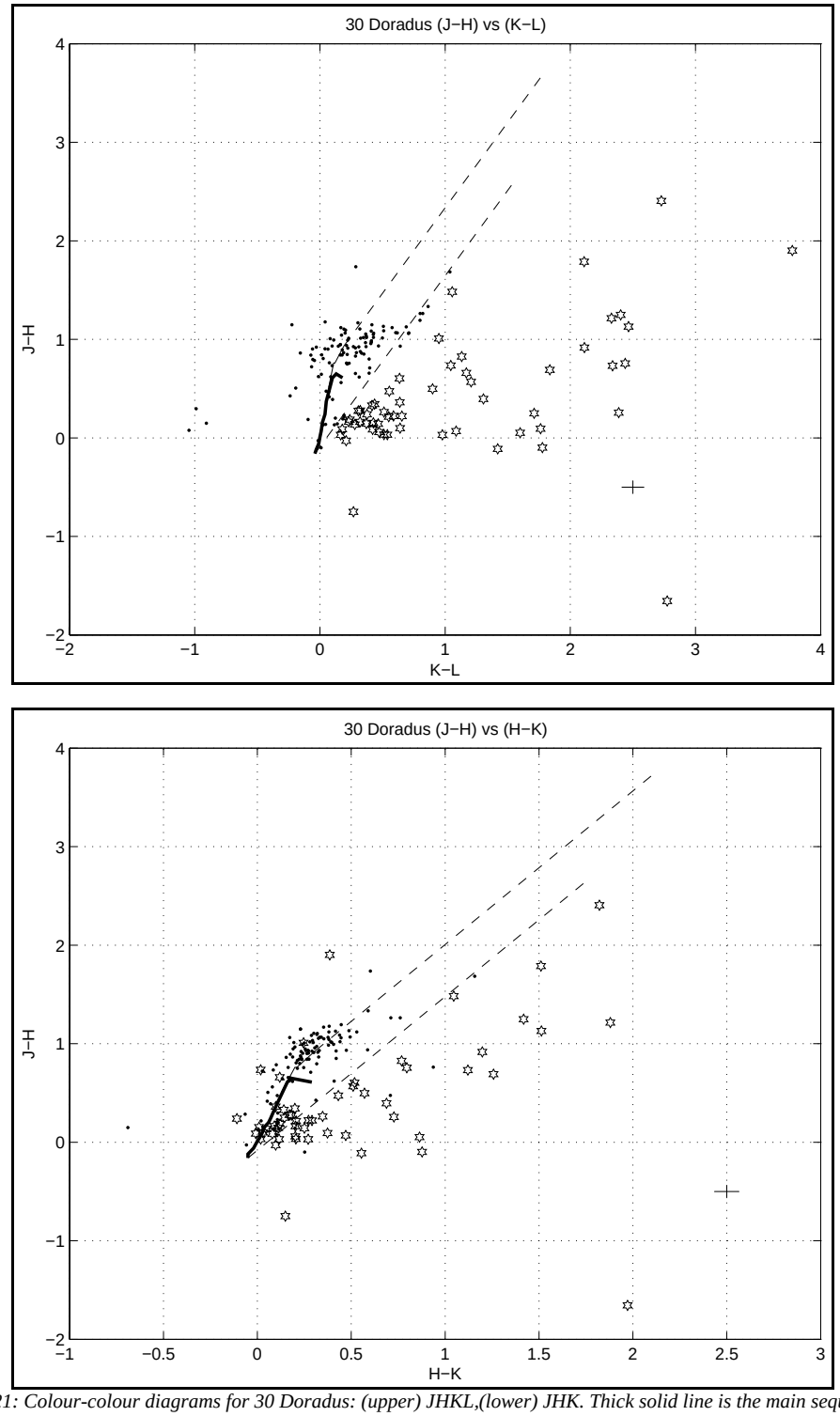


*Figure 21: Colour-colour diagrams for 30 Doradus: (upper) JHKL,(lower) JHK. Thick solid line is the main sequence for spectral types B6-8 to M5. The thin solid line is the giant branch for spectral types K0 to M5, but it is hard to see due to the large amount of stars in that region. Dashed lines are the reddening vectors up to $A_V$=30. Star shaped symbols are stars with IR-excess as found in the upper diagram. Mean errors are indicated in the lower right of the diagrams. The separation of stars with IR-excess is less clear in the JHK diagram, with several stars lying within the reddening vector, leading to an underestimation of the total disk fraction.*

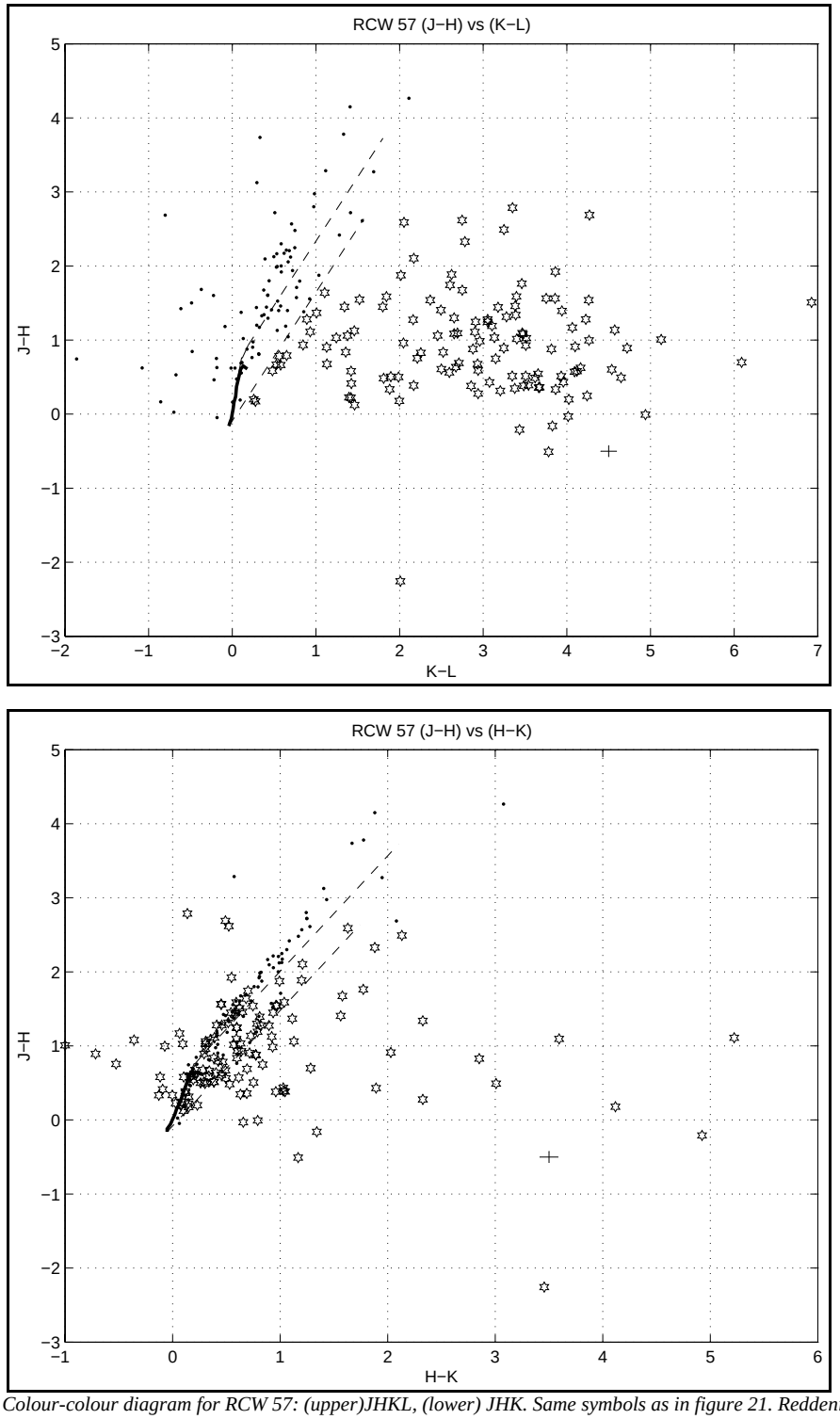


*Figure 22: Colour-colour diagram for RCW 57: (upper)JHKL, (lower) JHK. Same symbols as in figure 21. Reddening band is up to a visual extinction of 30 magnitudes. The separation of stars with IR-excess is much less clear in the JHK diagram with several stars lying within the reddening vector leading to an underestimation of the total disk fraction.*

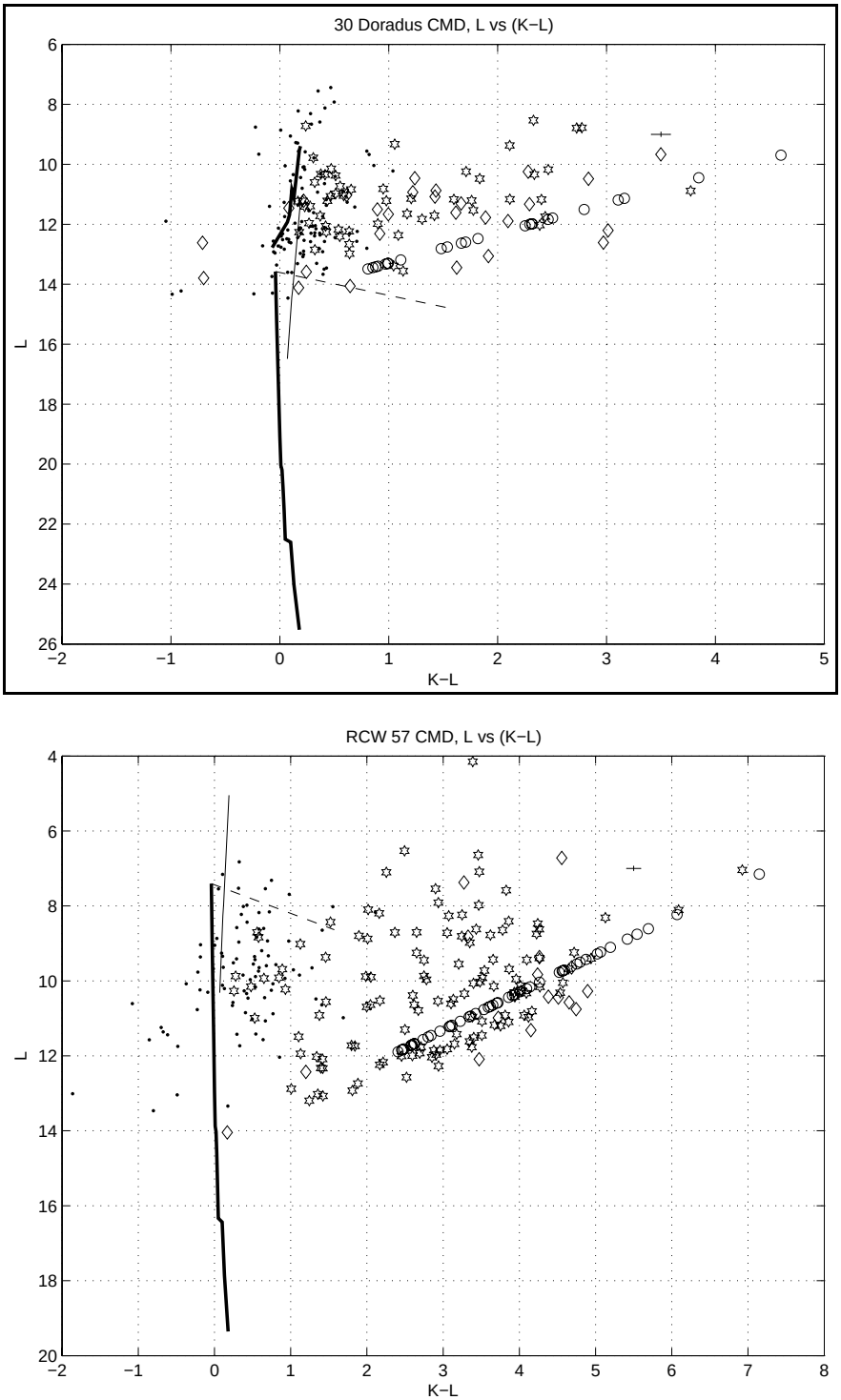


*Figure 23: L vs (K-L) colour-magnitude diagram for 30 Doradus (upper) and RCW 57 (lower). The thick solid lines are the unreddened main sequence, the thin solid line the giant branch. Dashed line is the reddening vector up to 30 magnitudes of visual extinction. In the upper image the upper thick solid line shows the location of supergiants. Diamond symbols are stars only found in K- and L-bands. Circle symbols are stars only found in the SPIREX image and are located at the lower limit, assuming these sources to be fainter than the 2MASS magnitude limit. The position of the stars found only in KL bands and L band can be compared to the location of stars with IR-excess (star shaped symbols). The ones occupying the same region are counted as having IR-excess as well.*

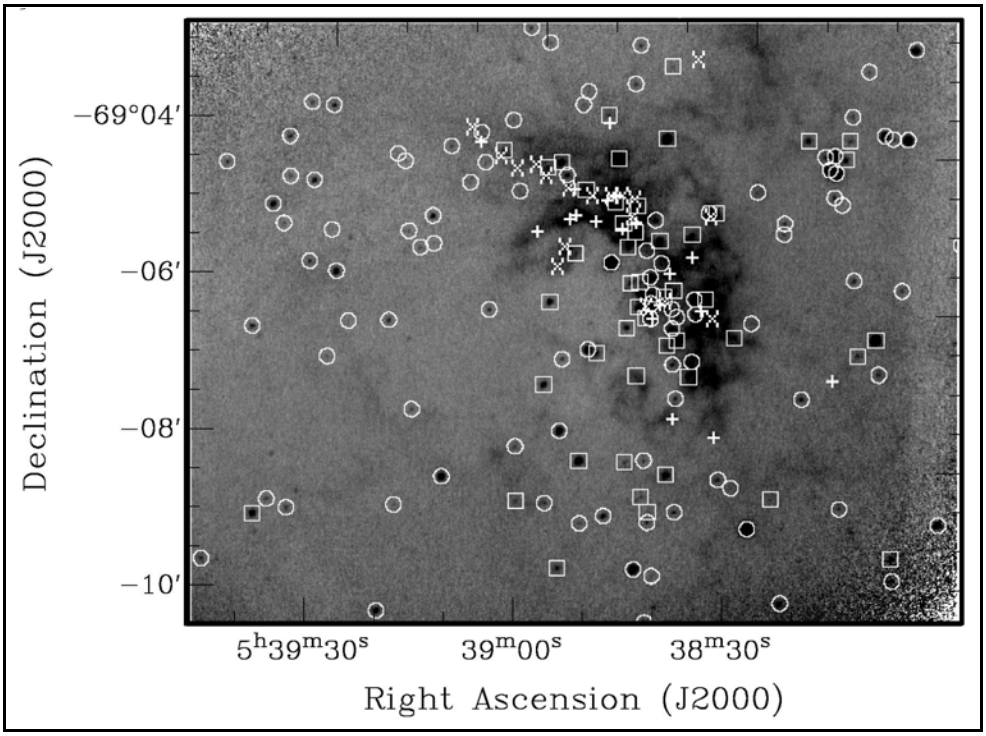


*Figure 24: Spatial distribution of sources in 30 Doradus. Circles mark stars found in any of the JHKL bands, squares mark stars with IR-excess found in the JHKL bands, plus signs mark stars found only in KL bands and crosses mark stars found only in L-band. The image shows only the central part of the SPIREX image. Stars outside this region areessentially stars without IR-excess.*

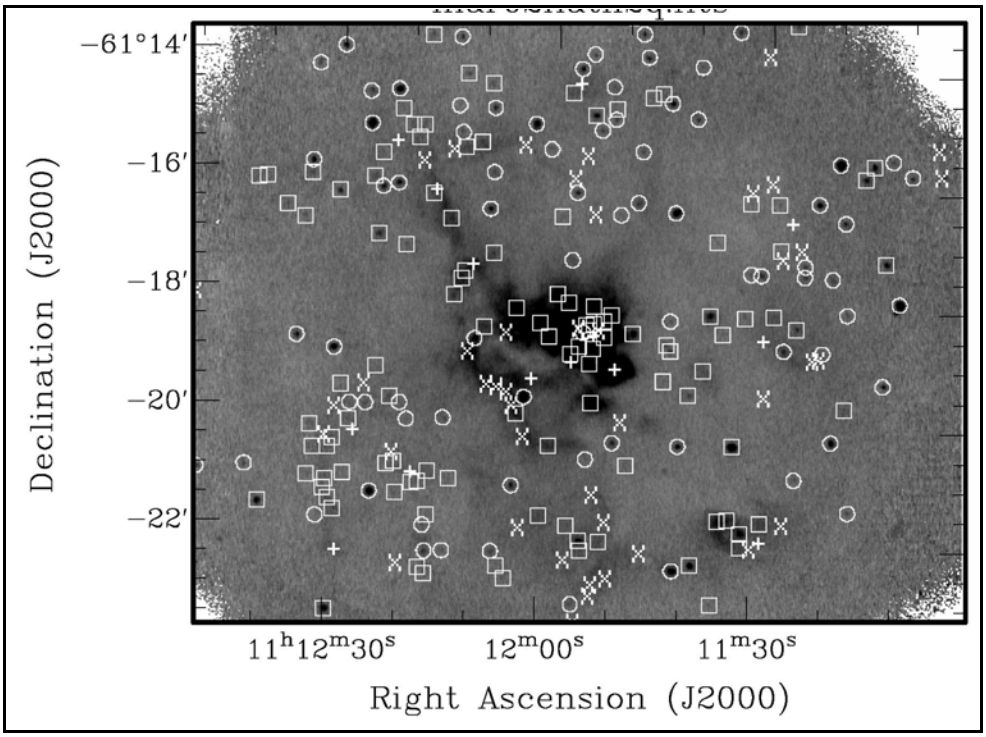


*Figure 25: Spatial distribution of sources in RCW 57. Same symbols as in figure above. The image only shows the central part of the SPIREX image. Stars outside this region are essentially stars without IR-excess.*

Matching a B0I supergiant and a O3V star from the Parker paper with my stars detected in the SPIREX image shows that these types of stars indeed occupy the region of the CMD where most of the detected stars lie (table 18), making it likely that I am mainly seeing the supergiant, giant and early type V stars.

| *type* | $m_V$ | $m_L$ | *(K-L)* | $id_{Parker}$ | $id_{SPIREX}$ |
|---|---|---|---|---|---|
| B0I | 13.61 | 13.78 | -0.69 | 850 | 218 |
| O3-6V | 14.72 | 10.24 | 1.71 | 1222 | 78 |
| O3-6V | 15.39 | 11.08 | 1.42 | 1429 | 284 |

*Table 18: Spectral types of stars from Parker, 1993 matched with stars detected in L-band in this thesis. Spectral type is as determined by Parker, V-band magnitudes are from Parker, L-band and (K-L) colours are from results obtained in this thesis. Column 5 gives the id as in the Parker paper, column 6 the id from this thesis. The L-band magnitudes position the B0I star at the bottom end of the supergiant location and the O3V above the main sequence, as expected, suggesting that the stars detected are of these types.*

### 9.4. 30 Doradus and RCW 57 – spatial distribution

Figure 24 and 25 show the spatial distribution of the sources detected in 30 Doradus and RCW 57 respectively. Stars marked with circles are stars found in any of the JHK or L-bands, stars marked with a box are stars with an IR-excess found in all bands (JHKL), stars marked with a plus are stars with an IR-excess that were only found in the K and L bands and stars marked with a cross are stars with an IR-excess that were only found in the L-band images. For 30 Doradus it can be seen that essentially all stars with an IR-excess lie within the central nebulosity. The positions of IR-excess stars follow the arcs and arms of the diffuse nebula. Within these regions it does not seem as if stars only detected in K and L bands occupy a preferred region. Stars only detected in L-band however seem to lie along a line to the north of the centre of the image, starting in the bright nebula and following an arm that stretches towards the north-east of the image. In RCW 57 stars with an IR-excess also lie predominantly in the nebulous regions of the image, again following the nebulous arcs and arms. A preferred region for stars only detected in the K and L-bands or only in the L-band does not appear to exist, as they occupy the same areas as stars detected in all bands. It seems however as if the central region of the nebula mainly contains stars detected in the JHKL bands.

### 9.5. Contamination by foreground stars

To determine the correct disk fraction an estimate of the number of foreground stars contaminating the image has to be made. This should be done by examining a comparison off-source image and scale the number of stars seen in that image to the sensitivity limit and size of the source image. This gives a statistical measure of the number of foreground stars which can be corrected for. If comparison images are not available, looking at the colours of the stars can give an estimate of the fraction of foreground stars. If the visual extinction $A_V$ to the source is known, the (J-K) colour due to interstellar reddening between the Earth and the source can be calculated. Assuming that the majority of all source stars are embedded and therefore additionally reddened, any star bluer than the given (J-K) colour is likely to be a foreground star. This is however only a first order approximation of the number of foreground stars and a more thorough investigation is required. Since the foreground stars will be blue stars they won't be counted as stars with IR-excess and therefore the disk fractions presented below represent lower limits. Nevertheless, to get a feeling for the number of foreground stars I examined the HR diagram plotting the J vs (J-K) colours for RCW 57 (figure 26). The solid line is the unreddened main sequence, the dots are all stars in the PSC and the star symbols are the stars from the PSC that matched with the SPIREX image. The main sequence for early-type stars seems to lie around a (J-K) colour of ~0 to ~0.5. Then there is a hint of a gap between ~0.5 and ~0.6 after which it seems as if the main sequence might be repeated at a redder colour. This first main sequence is interpreted as being main sequence stars between Earth and the source, i.e. foreground stars, whereas the second, redder main

sequence shows embedded main sequence stars, i.e. stars that belong to the source. The gap corresponds to a visual extinction of ~5 magnitudes. For 30 Doradus the visual extinction determined adopting an extinction parameter $R_V=A_V/E(B\text{-}V)$ of ~3.4 (Selman et al, 1999) and the (B-V) and $(B\text{-}V)_0$ colours (Walborn, Blades, 1997) give a visual extinction of ~1.4 which corresponds to a limiting (J-K) colour of ~0.6. In both cases excluding the stars bluer than the (J-K) colour limits increases the disk fraction with about 10-15% (see PART 3: CONCLUSIONS, 2. 30 Doradus and RCW 57).

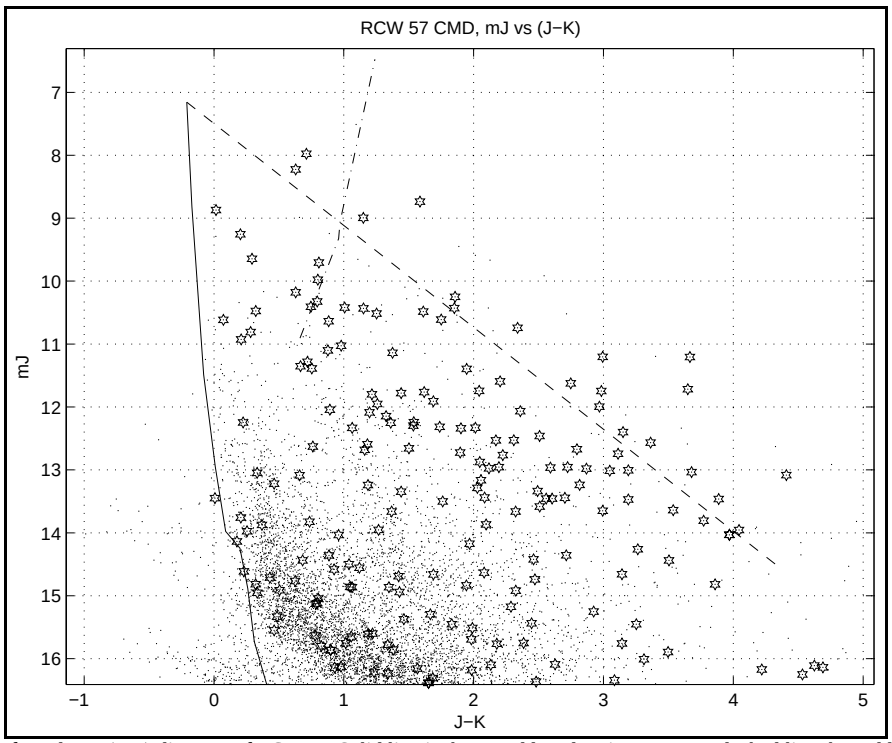


*Figure 26: Infrared J vs (J-K) diagram of RCW 57. Solid line is the unreddened main sequence, dashed line the reddening vector up to 30 magnitudes of extinction, dot-dashed line is the giant branch. Dots are all stars from the PSC and star symbols are PSC stars matched with SPIREX stars.*

### 9.6. The Galactic Centre

The creation of colour-colour and colour-magnitude diagrams for the Galactic Centre was done in the same way as for 30 Doradus and RCW 57, with the exception that the SPIREX image of the Galactic Centre is at 4.05 µm instead of 3.5 µm (L-band) and that only a region covering the inner 2.5' of the SPIREX image was considered. However, as opposed to the other two regions, the Galactic Centre is not an active star forming region. In addition to that, a large number of sources together within the error in the coordinate system (see 'matching the lists') made visual confirmation of all matches at best difficult. The results for the Galactic Centre must therefore be regarded with care and conclusions regarding circumstellar disks are not as easily made as for 30 Doradus and RCW 57.

Keeping that in mind, the same analysis for the Galactic Centre was done as for 30 Doradus and RCW 57. The number of stars detected with IR-excess is listed in table 19. Figures 27 and 28 show the colour-colour and colour-magnitude diagrams.

| *source* | *JHKBrα (1σ)* | *JHKBrα (2σ)* | *KBrα (1σ)* | *KBrα (2σ)* | *Brα (1σ)* | *Brα (2σ)* | *total (1σ)* | *total (2σ)* | *CDF* |
|---|---|---|---|---|---|---|---|---|---|
| Galactic Cen. | 26 | 26 | 13 | 13 | 8 | 8 | 47 | 47 | 51.6% |

*Table 19: Sources with IR excess for Galactic Centre at 1 σ and 2 σ distances from the reddening band. Sources found in in all four bands are listed under JHKBrα, sources only found in K- and Brα-bands are listed under KBrα. Sources only found in Brα-band are listed under Brα. The total disk fraction is calculated using the total number of stars detected in each region. Stars with IR-excess are sufficiently far away from the reddening band so that their number does not change, even taking a 2 σ distance into consideration.*

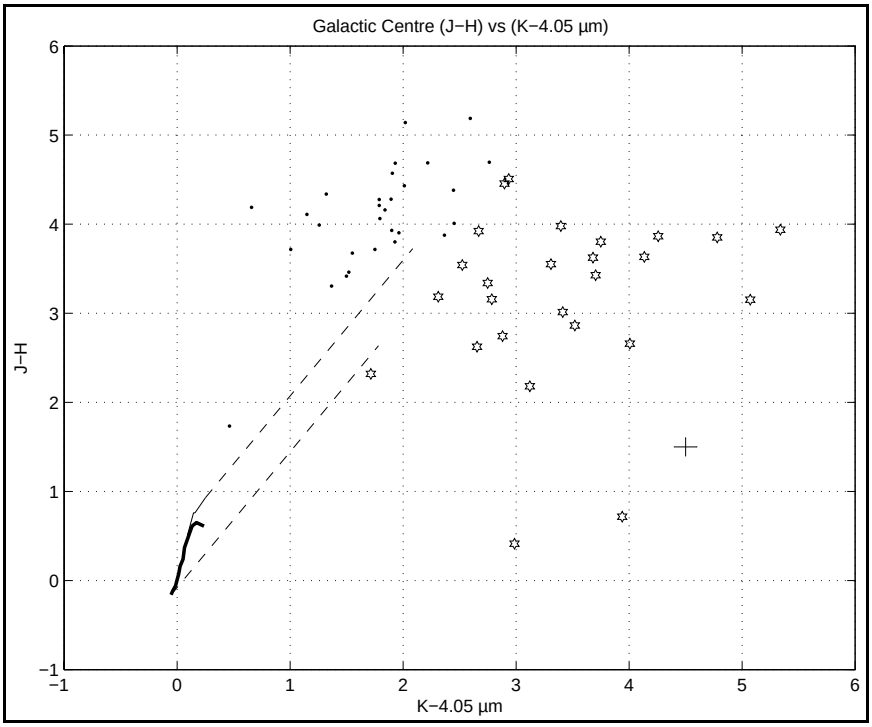


*Figure 27:JHK and 4.05 µm colour-colour diagram for the central 2' of the Galactic Centre. Symbols are the same as for 30 Doradus. Reddening band is up to a visual extinction of 30 magnitudes.*

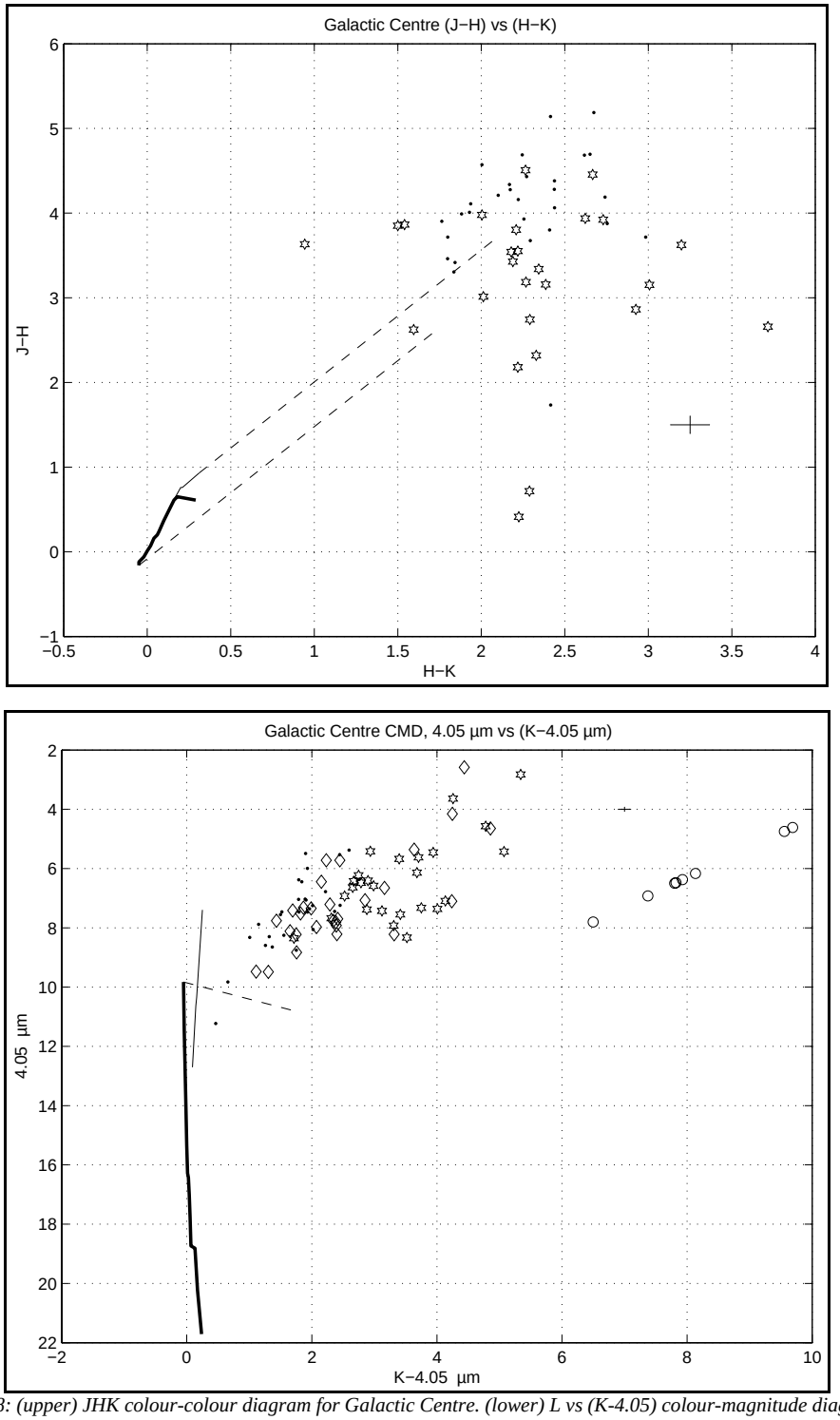


*Figure 28: (upper) JHK colour-colour diagram for Galactic Centre. (lower) L vs (K-4.05) colour-magnitude diagram for Galactic Centre. Symbols are the same as for 30 Doradus. The reddening vector is to an extinction of 30 magnitudes in the visual.*

### 9.7. RCW 38

A contour plot of the PAH emission in the central region of the RCW 38 image has been made using the flux/count calculated above. The contour plot was then overlaid with the 2MASS K-band image. Figure 29 shows the contour plot with contour levels between 6.12 $10^{-17}$ $Wm^{-2}$ and 3.67 $10^{-16}$ $Wm^{-2}$ with intervals of 6.12 $10^{-17}$ $Wm^{-2}$.

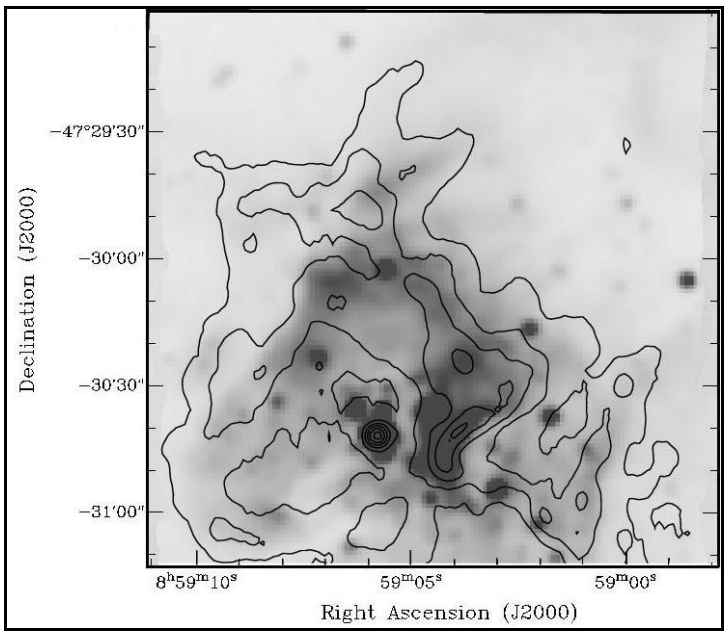


*Figure 29: Contour plot of PAH emission for RCW 38 overlaid over the 2MASS K-band image.*

# PART 3: DISCUSSION

## 10. Colour-colour diagrams

In all three cases (30 Doradus, RCW 57 and the Galactic Centre) the (J-H) vs (K-L) colour-colour diagrams show a large number of sources with infrared excess. Comparison with the (J-H) vs (H-K) diagrams shows that a significant number of sources would not be classified as having IR-excess only using the shorter wavelength data. By modelling the colours of stars with circumstellar disks using standard disk models, it can be shown that these models very well explain the location of stars outside the reddening bands in infrared colour-colour diagrams (Lada and Adams, 1992). In particular, it is pointed out that the amount of extinction required must come from a circumstellar disk, as infrared excess is detected over a large range of wavelengths and the amount of extinction necessary to produce this excess would extinguish the star at visual and near infrared wavelengths for any other distribution of circumstellar material. This allows interpreting the IR-excess as circumstellar disks around the stars. L-band observations therefore prove to be efficient at determining the cluster disk fraction (CDF).

## 11. 30 Doradus and RCW 57

Together with the CDF and the age of the cluster, it is possible to make estimations of the lifetime of circumstellar disks. Walborn et al find several regions with different ages in the 30 Doradus region. The massive central region is estimated to be ~2-3 Myr old, but a much younger population of less than 1 Myr and an older population of about 4-6 Myr are also found (Walborn, Blades, 1997) (Massey, Hunter, 1998). Adopting a mean age for 30 Doradus of 2-3 Myr the detected number of stars with IR-excess for 30 Doradus (~40 - 45%, table 17) would imply that more than 50% of the circumstellar disks have disappeared after 2-3 Myr. The very young cluster in RCW 57 still has ~70 % of its disk content remaining. Since RCW 57 mainly consists of one population of very young massive stars (Persi et al, 1994), the larger disk fraction for this region gives further support for the idea of evolving disks, the higher mean age of the cluster due to the older populations in 30 Doradus being reflected in a lower CDF. The results for RCW 57 imply that a large fraction of protostars (> 70%) form circumstellar disks. When interpreting my results, it must be kept in mind that due to the limited examination of foreground stars, the CDFs estimated here are only lower limits. Assuming that the exclusion of foreground stars increases the CDF with ~10-15%, approximately half of the stars lose their disks after ~2-3 Myr (30 Doradus) and more than 80% of the protostars form disks (RCW 57). If one assumes a linear relationship for the evolution and hence destruction of circumstellar disks, this would give a total disk lifetime of ~6 Myr. It is possible that the intense radiation from the early type stars in the 30 Doradus region effectively destroys circumstellar disks and therefore decreases the CDF. Observations of HII regions in the Galaxy have shown that externally illuminated circumstellar disks get photoevaporated and disappear after 0.01-0.1 Myr. If this is the case for 30 Doradus, the lifetime for disks estimated using the CDF of this region would be too low, hence lifetimes of 4-6 Myr can only be seen as a lower limit.

In order to make predictions on the lifetime of circumstellar disks, it is necessary to observe a number of clusters with a range of ages. This was done for the first time by Haisch, Lada and Lada in 2001 (Haisch et al, 2001 June). In their paper they combine JHKL observations for the clusters NGC 2264, NGC 2362 and NGC 1960 (ages between 2.5-30 Myr) with earlier observations for the younger clusters NGC 2024, Trapezium and IC 348, going down to ages of 0.3 Myr (NGC 2024). For all these clusters the fraction of sources with JHKL excess is determined. Each cluster is then plotted in a CDF

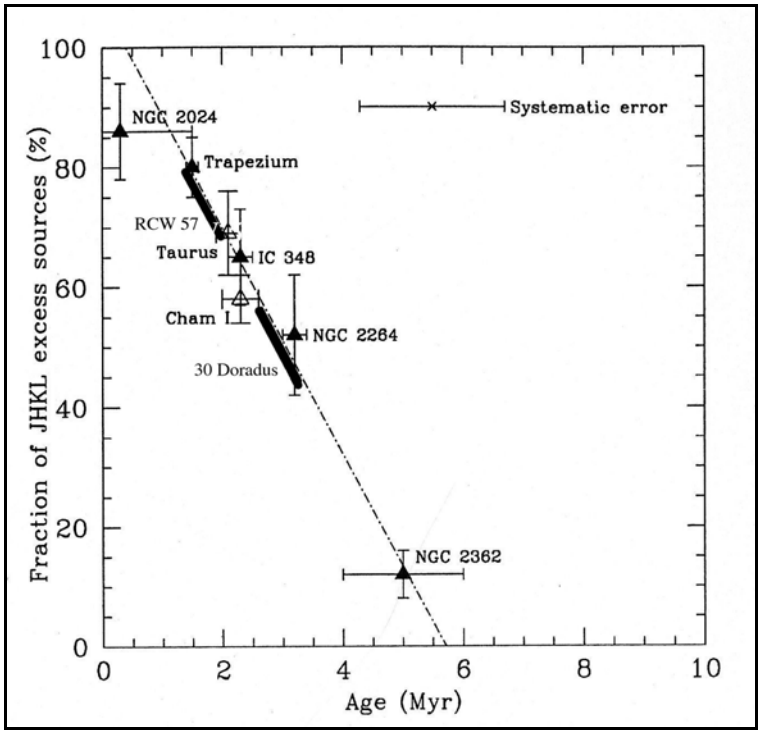


*Figure 30: CDF for 6 clusters by Haisch, Lada and Lada vs their mean ages. The location of 30 Doradus and RCW 57 is indicated by the solid lines along the dot-dashed line. Image from (Haisch et al, 2001 June).*

vs cluster age diagram (figure 30). The ages for the clusters are taken from the literature. A least-squares fit of a straight line to the data shows a linear relationship between disk fraction and cluster age. An estimated disk lifetime of 6 Myr is derived. The initial disk fraction appears to be very high (> 80%) and then declines linearly quickly with increasing age. The uncertainty in the age of NGC 2362 affects the fit of the straight line and implies disk lifetimes of 4-8 Myr, and a possible non-linear relationship for the evolution of old disks (this requires large errors in the age of NGC 2362 though). Even for the longest disk lifetimes (8 Myr), the data requires half of all stars to lose their disks within 4 Myr. The assumed age of 2-3 Myr for 30 Doradus would in this diagram give a disk fraction of 50 – 70 %, higher than the disk fraction determined in this thesis (43.5±4.6 %, table 17). Taking the 10-15% difference in the CDF due to foreground stars into consideration though, my results lie at the low end of what Haisch et al predict. The age of RCW 57 is not very well known. Barbosa et al (2003) indicate that the stars with an IR-excess as identified by Figuerêdo et al (2002), might be younger than the objects visible in M17, which are estimated to be younger than 3 Myr (Jiang et al, 2002). Considering that the detected stars most likely are massive pre-main sequence stars, zero-age-main sequence and main sequence stars, an age of less than 2 Myr is likely. In the diagram this would indicate a disk fraction of 70% or more, which also is consistent with my results (68.1±1.8 %, table 17). Since the lifetime for massive stars in the pre-main sequence stage is very short (~$5x10^5$ for a 5 $M_{sun}$ star (Christensen-Dalsgaard, 2000)), an even younger age of less that 1 Myr is possible for RCW 57. In this case the cluster disk fraction is less than predicted by Haisch et al, possibly together with NGC 2024 indicating a turn-off in the disk fraction for very young clusters. This could indicate a faster evolution of circumstellar disks around massive stars (Lada et al, 2000). It does not however seem to affect the initial disk fraction significantly, implying that the formation of circumstellar disks is largely independent of stellar mass.

Whereas 30 Doradus contains a large range of stellar masses (Brandner et al, 2001), we are mainly picking up the young massive stars. The fact that my results lie at the lower end of what is predicted by Haisch et al might again indicate a faster evolution of circumstellar disks around massive stars. The large number of young, massive stars showing IR-excess in RCW 57 does indicate that high-mass stars

possibly form from circumstellar disks like low-mass stars do. This is confirmed for the first time by an ESO News press release from May 13, 2004 (High Mass Stars Form From Disks Too). Rolf Chini and his team from the Ruhr-Universität in Bochum (Germany) find a nearly edge on flared disk around a ~20 solar mass central object. The accretion phase is still active and models predict that about 30-50% of the circumstellar material can be accumulated onto the central object. This makes it likely that the central object is a massive star forming from the surrounding disk.
Previous studies of the 30 Doradus complex show sources with IR-excess in JHK colour-colour diagrams (Brandner et al, 2001). These sources were associated with Herbig Ae/Be and T Tauri stars by comparing the detected colours with model colours for these stars. This again confirms the connection between star formation, circumstellar disks and IR-excess. In their study the sources of star formation are found to follow the densest regions of the molecular gas and the interface with the hollowed-out region from the central stars. The same is true for most of the 20 stars detected only in the L-band, which lie in the nebulous region north of the central star cluster (figure 24). In the L vs (K-L) colour-magnitude diagram they occupy the same region as the IR-excess stars from the (J-H) vs (K-L) colour-colour diagram. This makes it likely that these stars are in the process of forming and also contain circumstellar disks. The same is true for RCW 57, where the stars without matches in the JHK bands lie within the nebular regions (figure 25). These properties are characteristic of protostellar objects and the sources only detected in the L-band are possibly Class I protostars (Lada et al, 2000). The fact that these stars are only detected in the L-band, and not at shorter wavelengths, is evidence for these stars being heavily embedded in the circumstellar dust shells, possibly being regions of high-mass star formation.

No other extensive investigation of the JHKL colour excess has been made for RCW 57 and 30 Doradus, making this the first study of infrared excess for a significant number of stars for these regions. The JHKL investigation of the Trapezium cluster in Orion by Lada et al (Lada et al, 2000) found a large proportion of stars with circumstellar disks (~80 %) for this very young cluster in accordance with the results obtained for RCW 57. They also found that the formation and evolution of disks is independent of stellar mass for stars of type F or later. For early type stars (O,B and A) it is found that the fraction of disks is somewhat lower, indicating that high-mass stars either have a lower probability of forming disks or that disks dissipate quicker around early-type stars. This might explain the relatively low CDF of RCW 57 in figure 30.

## 12. The Galactic Centre

Due to the nature of the Galactic Centre region, interpretation of the colour-colour diagrams is not as straightforward as for 30 Doradus and RCW 57. In addition, the SPIREX image of the Galactic Centre was taken at 4.05 μm. An analysis of the JHKL colours of ~2000 stars in the Galactic Centre (Blum et al, 1996), reveals large and variable extinction, in some cases with $A_K > 6$. This can be seen in the spread of stars in the colour-colour diagrams. Blum et al conclude that some of the objects in the GC may have IR excess and compare these to the colours of YSOs. However, they only use the JHK information in their data, possibly missing sources which show IR-excess at longer wavelengths. Combining the JHK magnitudes with the magnitudes at 4.05 μm, I find that ~50% of the sources in the Galactic Centre show infrared excess, possibly indicating a larger number of protostellar objects with disks. Spectroscopic analysis of the sources in the Galactic Centre would be necessary to make definite statements about their evolutionary state, although some estimations can be made using photometric data. When plotting stars with known spectral types in a colour-magnitude diagram, Clénet et al (Clénet et al, 2001) find that detected types form relatively homogeneous groups in the diagram. Stars only found in the SPIREX image lie far away from the other stars towards the red end of the CMD obtained here for the Galactic Centre (figure 28). These stars all lie in the very bright nebular region in the centre of the region and might be deeply embedded protostellar objects, possibly high-mass stars in the process of formation.

## 13. Summary

I have obtained JHKL photometry for 30 Doradus, RCW 57 and the Galactic Centre. The data was analysed by plotting the stars in (J-H) vs (K-L) diagrams and detecting the infrared excess. The infrared excess is interpreted as an indicator for circumstellar disks. In all cases the JHKL data proves to be more powerful in detecting IR-excess than previously used JHK diagrams. A significant amount of sources show IR-excess (~50% for 30 Doradus, ~70% for RCW 57 and ~50% for the Galactic Centre) and when compared to earlier and similar studies of star formation complexes, the 30 Doradus and RCW 57 data fit well with previous results. In accordance with previous studies, a total lifetime for circumstellar disks of ~6 Myr is determined with a very high initial disk fraction of > 80%, which gives important constraints for planet formation, by limiting the time available to form planets. The formation of circumstellar disks seems to be independent of stellar mass, giving strong implications for the formation process of high-mass stars and supporting recent findings of high-mass stars forming from disks. The fact that the results of 30 Doradus fit well with Galactic sources is further evidence of no difference between Galactic and extragalactic star formation with different metalicities. Both in 30 Doradus and RCW 57 a number of sources are only detected in the L-band. The large amount of extinction at shorter wavelengths suggests that these sources are heavily embedded protostars. Results for the Galactic Centre can not be interpreted as easily, although signs of a population of pre-main sequence stars with circumstellar disks and heavily embedded protostars exist.

Future observations of clusters observed at different ages, especially very young clusters and clusters that lie close to the predicted lifetime of disks, are necessary to probe the possible non-linearity of disk evolution at the late stages and to study a possible turn-off of the disk fraction for very young sources. Also, more studies of high-mass star formation clusters would be required to determine whether the disk evolution is quicker for high-mass stars (A0 type and earlier) and to determine what role circumstellar disks play in the formation of these stars.

## 14. Acknowledgements

I would like to thank Michael Burton for being a great supervisor and making my time here at UNSW really enjoyable. Thank you for always being there when I got stuck and conveniently being occupied whenever it was better for me to just sit down and figure things out myself. I've learnt more than I ever thought possible. Thank you to Hans Olofsson for ongoing support from Sweden and the quick answers to the constant flux of e-mails from my side. Also from Sweden I'd want to thank Christoffer Sunesson and Matt Hayes for keeping me up-to-date with life at the Stockholm Observatory. Of course I have to say thank you to Steven Longmore, not only for essentially being my third supervisor, but also for discovering that B.B. King delivers the best observing soundtrack and that 99% humidity is not a reason to shut down the dome. Although I don't know for what, I'd still like to thank Matt - 'This-Is-Insane' Owers. I suppose a good chat with proper insults always lightened up a day in the office. I'd like to thank everyone in my office, Chas, Paul, Jessie, Patricia and Aliz. Thank you Suzanne for lending me your Mark Knopfler CDs - just the right soundtrack for finishing up my work. And of course thank you Melinda for ongoing Linux support. Thanks to everyone in the astronomy department at UNSW, in particular the star formation group. You've made my stay unforgettable and a true once in a lifetime experience. Sounds cheesy, but I don't know how else to say it. And without a doubt I would want to thank Victoria. You made this trip to what it really was and I will never forget that. Without you it would not have been possible. You know what I mean. And of course thank you, Victoria, for the graphical support. I'm sorry for wanting to make a front-page in Microsoft Word.

## Appendix A - Literature cited

Allen, C. W., *Astrophysical Quantities, 3rd ed. (London: The Athlone Press, 1973)*
Barbosa et al, *ApJ 126:2411-2420, 2003 November*
Beatty, J. K.; Petersen, C. C.; Chaikin, A. (Editors), *The new solar system*, *4th ed. (Cambridge University Press, 1999)*
Beckwith, S. V. W., *Near Infrared Techniques For Studies Of Star Formation*, in Ray, Beckwith (Editors), *Star Formation and Techniques in IR and mm-Wave Astronomy (Springer-Verlag, 1994)*
Blum et al, *ApJ, 470:864-881, 1996 October*
Bosch et al, *A&A Suppl. Ser. 137, 21-24, 1999*
Brandeker, A., *Young Stars And Circumstellar Disks, PhD thesis, Stockholm Observatory, Stockholm, 2003*
Brandner et al, *ApJ 122:858-865, 2001 August*
Burton et al, *Proceedings ASA, 1994, 11 (2) 127-50*
Christensen-Dalsgaard, J., *Lecture Notes on Stellar Structure and Evolution,* 5th ed. (*Institut for Fysik og Astronomi, Aarhus Universitet, 2000)*
Clénet et al, *A&A 376, 124-135, 2001*
Emerson, D., *Interpreting Astronomical Spectra*, *(John Wiley & Sons, 1996)*
Figuerêdo et al, *AJ 124:2739-2748, 2002 November*
Haisch et al, *AJ 121:2065-2074, 2001 April*
Haisch et al, *ApJ 553:L153-L156, 2001 June*
Jiang et al, *ApJ 577:245-259, 2002 September*
Kenyon et al, *AJ 121:2673-2680, 2001 May*
Koorneef, *A&A 128, 84-93*, *1983*
Lada, Lada, *Annu. Rev. Astron. Astrophys. 41:57-115, 2003*
Lada, Adams, *ApJ 393:278-288, 1992 July*
Lada et al, *AJ 120:3162-3176, 2000 December*
Liseau et al, *A&A 402, 183-187, 2003*
Lyo et al, *Mon. Not. R. Astron. Soc. 338, 616-622, 2003*
Massex, Hunter, *ApJ 493:180-194, 1998 January*
McGregor, Hyland, *ApJ 250:116-134, 1981 November*
Panagia et al, *ApJ 272:123-130, 1983 September*
Parker, *AJ 106:560-577, 1993 August*
Persi et al, *A&A 282, 474-484, 1994*
Rathborne, *Young Massive Stars: Traffic Lights for Nearby Star Formation, PhD thesis, University of New South Wales, Sydney, 2003*
Rathborne, Burton, *ASP Conference Series, Vol. 13, 2003*
Schneider et al, *ApJ 513:L127-L130, 1999 March*
Selman et al, *A&A 341,98-109, 1999*
Shu et al, *Ann. Rev. Astron. Astrophys. 25:23-81, 1987*
Walborn, Blades, *ApJ Supp. Ser. 112:457-485, 1997 October*
Zuckerman, *Annu. Rev. Astron. Astrophys. 39:549-80, 2001*
SPIREX/Abu data pipeline, *http://pipe.cis.rit.edu*
2MASS homepage, *http://www.ipac.caltech.edu/2mass/*
*2*MASS, *Photometry/Astrometry from 2MASS Quicklook Images, http://www.astro.caltech.edu/~jmc/2mass/v3/quicklook/*
Mount Stromlo Siding Spring Observatory, *http://msowww.anu.edu.au/*
McGregor, *User Manual for the Cyrogenic Array Spectrometer/Imager (CASPIR) on MSSSO 2.3m Telescope, 1997 June*
JACARA homepage, *www.phys.unsw.edu.au/jacara*
Davis, *A Reference Guide to the IRAF/DAOPHOT Package, 1994 January*

# Appendix B

## Coordinates and magnitudes for all sources detected in SPIREX images

### 30 Doradus

| *id* | *RA (J2000)* *h m s* | | | *Dec (J2000)* *d m s* | | | $m_J$ | $m_H$ | $m_K$ | $m_L$ | $id_{IRAF}$ |
|---|---|---|---|---|---|---|---|---|---|---|---|
| 1 | 5 | 38 | 53.86 | -69 | 9 | 31.32 | 15.74 | 14.98 | 14.19 | 11.75 | 29 |
| 2 | 5 | 38 | 37.39 | -69 | 8 | 43.08 | 13.43 | 12.54 | 12.36 | 12.19 | 37 |
| 3 | 5 | 38 | 45.05 | -69 | 4 | 47.28 | 13.99 | 13.92 | 13.45 | 12.37 | 287 |
| 4 | 5 | 38 | 23.69 | -69 | 5 | 3.48 | 12.63 | 12.66 | 12.71 | 12.73 | 147 |
| 5 | 5 | 38 | 14.78 | -69 | 3 | 29.88 | 14.08 | 13.33 | 13.11 | 12.90 | 148 |
| 6 | 5 | 38 | 53.76 | -69 | 3 | 32.04 | 14.21 | 13.35 | 13.16 | 12.97 | 102 |
| 7 | 5 | 38 | 13.18 | -69 | 5 | 36.6 | 12.74 | 12.32 | 12.27 | 12.19 | 132 |
| 8 | 5 | 39 | 7.44 | -69 | 4 | 20.64 | 13.75 | 13.45 | 13.34 | 14.34 | 266 |
| 9 | 5 | 38 | 47.09 | -69 | 5 | 1.68 | 11.87 | 13.52 | 11.55 | 8.78 | 77 |
| 10 | 5 | 38 | 42.74 | -69 | 5 | 42.72 | 11.18 | 11.05 | 10.93 | 10.82 | 73 |
| 11 | 5 | 38 | 41.21 | -69 | 2 | 58.56 | 13.75 | 13.65 | 13.62 | 12.99 | 322 |
| 12 | 5 | 38 | 58.34 | -69 | 4 | 21.72 | 15.40 | 15.15 | 14.42 | 12.03 | 86 |
| 13 | 5 | 38 | 30.96 | -69 | 1 | 15.96 | 10.87 | 10.65 | 10.63 | 10.44 | 156 |
| 14 | 5 | 38 | 16.66 | -69 | 4 | 14.16 | 9.83 | 8.92 | 8.59 | 8.31 | 134 |
| 15 | 5 | 38 | 45.89 | -69 | 2 | 43.44 | 13.40 | 12.55 | 12.33 | 12.16 | 104 |
| 16 | 5 | 38 | 17.62 | -69 | 4 | 12 | 10.82 | 10.06 | 9.82 | 9.59 | 135 |
| 17 | 5 | 39 | 14.30 | -69 | 5 | 25.44 | 15.12 | 14.13 | 13.72 | 13.61 | 198 |
| 18 | 5 | 39 | 1.92 | -69 | 2 | 34.44 | 14.57 | 13.44 | 12.95 | 12.44 | 153 |
| 19 | 5 | 38 | 26.69 | -69 | 8 | 52.8 | 9.83 | 8.82 | 8.42 | 7.92 | 141 |
| 20 | 5 | 38 | 44.21 | -69 | 5 | 47.04 | 12.65 | 12.56 | 12.48 | 12.06 | 216 |
| 21 | 5 | 38 | 45.55 | -69 | 5 | 47.76 | 11.89 | 11.73 | 11.64 | 11.41 | 74 |
| 22 | 5 | 39 | 35.83 | -69 | 4 | 8.04 | 13.56 | 12.49 | 12.12 | 11.92 | 111 |
| 23 | 5 | 38 | 53.40 | -69 | 2 | 0.96 | 10.88 | 10.82 | 10.62 | 10.15 | 149 |
| 24 | 5 | 39 | 5.81 | -69 | 6 | 14.4 | 13.74 | 12.64 | 12.32 | 12.13 | 57 |
| 25 | 5 | 38 | 16.68 | -69 | 4 | 33.24 | 13.58 | 12.57 | 12.38 | 12.05 | 131 |
| 26 | 5 | 38 | 46.18 | -69 | 5 | 19.32 | 13.44 | 13.34 | 12.97 | 11.21 | 190 |
| 27 | 5 | 38 | 40.58 | -69 | 5 | 57.12 | 10.84 | 10.60 | 10.71 | 10.33 | 68 |
| 28 | 5 | 38 | 57.31 | -69 | 7 | 9.84 | 12.19 | 11.72 | 11.28 | 10.73 | 25 |
| 29 | 5 | 38 | 34.75 | -69 | 4 | 50.52 | 13.23 | 12.16 | 11.67 | 11.07 | 127 |
| 30 | 5 | 37 | 59.09 | -69 | 8 | 41.28 | 11.16 | 10.12 | 9.74 | 9.57 | 177 |
| 31 | 5 | 38 | 15.36 | -69 | 4 | 3.72 | 11.86 | 11.72 | 11.68 | 11.40 | 138 |
| 32 | 5 | 38 | 6.58 | -69 | 3 | 45 | 10.56 | 9.72 | 9.45 | 9.29 | 161 |
| 33 | 5 | 38 | 12.00 | -69 | 6 | 34.2 | 12.84 | 12.69 | 12.68 | 12.26 | 133 |
| 34 | 5 | 38 | 48.17 | -69 | 4 | 11.64 | 15.28 | 14.16 | 12.64 | 10.18 | 99 |

| *id* | *RA (J2000)* *h m s* | | | *Dec (J2000)* *d m s* | | | $m_J$ | $m_H$ | $m_K$ | $m_L$ | $id_{IRAF}$ |
|---|---|---|---|---|---|---|---|---|---|---|---|
| 35 | 5 | 38 | 36.07 | -69 | 6 | 46.44 | 12.45 | 12.31 | 12.10 | 11.97 | 47 |
| 36 | 5 | 38 | 13.56 | -69 | 8 | 33 | 15.24 | 14.05 | 13.60 | 12.81 | 142 |
| 37 | 5 | 38 | 14.62 | -69 | 0 | 57.6 | 12.10 | 11.08 | 10.69 | 10.32 | 158 |
| 38 | 5 | 38 | 54.82 | -69 | 6 | 49.68 | 13.65 | 12.74 | 12.50 | 12.56 | 41 |
| 39 | 5 | 39 | 20.23 | -69 | 4 | 17.4 | 15.16 | 14.21 | 13.90 | 13.50 | 254 |
| 40 | 5 | 38 | 41.21 | -69 | 8 | 52.08 | 13.69 | 13.04 | 12.86 | 12.58 | 36 |
| 41 | 5 | 38 | 48.77 | -69 | 1 | 38.64 | 12.91 | 11.43 | 10.38 | 9.33 | 106 |
| 42 | 5 | 39 | 0.98 | -69 | 7 | 58.8 | 13.71 | 12.81 | 12.55 | 12.49 | 24 |
| 43 | 5 | 38 | 8.88 | -69 | 6 | 47.88 | 14.35 | 13.28 | 12.95 | 12.24 | 180 |
| 44 | 5 | 38 | 42.24 | -69 | 8 | 32.28 | 13.62 | 13.34 | 13.17 | 12.85 | 185 |
| 45 | 5 | 38 | 47.64 | -69 | 8 | 49.2 | 13.02 | 11.91 | 11.52 | 11.36 | 28 |
| 46 | 5 | 38 | 42.48 | -69 | 6 | 3.6 | 9.02 | 9.12 | 8.87 | 8.86 | 65 |
| 47 | 5 | 37 | 58.13 | -69 | 5 | 3.84 | 12.57 | 11.55 | 11.27 | 10.93 | 168 |
| 48 | 5 | 39 | 19.08 | -69 | 4 | 22.44 | 14.49 | 13.57 | 13.33 | 13.36 | 89 |
| 49 | 5 | 39 | 14.64 | -69 | 5 | 3.48 | 12.48 | 11.58 | 11.31 | 11.27 | 92 |
| 50 | 5 | 38 | 42.19 | -69 | 8 | 4.2 | 13.80 | 13.02 | 12.92 | 12.96 | 39 |
| 51 | 5 | 38 | 27.77 | -69 | 6 | 14.76 | 14.98 | 14.26 | 14.23 | 14.30 | 294 |
| 52 | 5 | 38 | 23.64 | -69 | 4 | 55.2 | 13.84 | 12.84 | 12.59 | 12.51 | 130 |
| 53 | 5 | 38 | 59.02 | -69 | 2 | 44.52 | 14.13 | 13.47 | 13.31 | 12.92 | 152 |
| 54 | 5 | 38 | 44.98 | -69 | 8 | 6.72 | 13.38 | 13.16 | 12.96 | 12.41 | 186 |
| 55 | 5 | 38 | 45.70 | -69 | 6 | 22.32 | 11.49 | 11.52 | 11.42 | 11.22 | 59 |
| 56 | 5 | 38 | 38.11 | -69 | 7 | 14.88 | 14.92 | 13.19 | 12.59 | 12.30 | 40 |
| 57 | 5 | 38 | 59.09 | -69 | 1 | 8.76 | 12.82 | 11.49 | 10.90 | 10.04 | 154 |
| 58 | 5 | 38 | 16.99 | -69 | 4 | 0.84 | 10.15 | 9.28 | 8.95 | 8.67 | 137 |
| 59 | 5 | 38 | 57.07 | -69 | 6 | 5.76 | 11.29 | 11.12 | 10.92 | 10.60 | 58 |
| 60 | 5 | 38 | 6.17 | -69 | 5 | 42 | 14.14 | 13.21 | 12.95 | 12.31 | 169 |
| 61 | 5 | 38 | 48.48 | -69 | 5 | 32.64 | 9.18 | 8.33 | 7.91 | 7.56 | 75 |
| 62 | 5 | 39 | 7.15 | -69 | 1 | 53.04 | 11.71 | 10.70 | 10.40 | 10.17 | 151 |
| 63 | 5 | 39 | 28.15 | -69 | 5 | 50.64 | 11.47 | 10.74 | 10.65 | 10.56 | 94 |
| 64 | 5 | 38 | 51.19 | -69 | 6 | 41.4 | 11.52 | 10.61 | 10.31 | 10.09 | 42 |
| 65 | 5 | 38 | 33.62 | -69 | 4 | 50.52 | 12.01 | 11.79 | 11.49 | 10.84 | 129 |
| 66 | 5 | 38 | 53.71 | -69 | 5 | 27.24 | 13.95 | 13.45 | 12.88 | 11.99 | 191 |
| 67 | 5 | 38 | 50.59 | -69 | 2 | 0.24 | 13.75 | 12.80 | 12.61 | 12.45 | 150 |
| 68 | 5 | 38 | 19.85 | -69 | 7 | 10.2 | 13.15 | 12.35 | 12.13 | 11.74 | 126 |
| 69 | 5 | 39 | 16.25 | -69 | 5 | 28.68 | 13.99 | 13.00 | 12.76 | 12.54 | 93 |
| 70 | 5 | 39 | 11.33 | -69 | 2 | 1.68 | 12.13 | 11.91 | 11.64 | 11.05 | 172 |
| 71 | 5 | 38 | 43.20 | -69 | 6 | 14.76 | 11.63 | 12.38 | 12.23 | 11.97 | 60 |
| 72 | 5 | 38 | 34.61 | -69 | 5 | 57.12 | 13.96 | 12.74 | 10.86 | 8.54 | 119 |
| 73 | 5 | 38 | 27.86 | -69 | 4 | 32.16 | 14.78 | 13.72 | 13.28 | 12.57 | 296 |
| 74 | 5 | 38 | 52.73 | -69 | 4 | 37.56 | 16.24 | 15.00 | 13.58 | 11.18 | 83 |
| 75 | 5 | 39 | 25.94 | -69 | 6 | 29.16 | 14.82 | 14.39 | 14.08 | 14.32 | 224 |
| 76 | 5 | 38 | 55.54 | -69 | 4 | 26.76 | 13.71 | 13.09 | 12.68 | 12.59 | 84 |
| 77 | 5 | 38 | 9.55 | -69 | 6 | 21.24 | 9.26 | 9.08 | 8.96 | 8.72 | 179 |
| 78 | 5 | 38 | 41.62 | -69 | 5 | 13.92 | 11.12 | 11.09 | 10.88 | 10.37 | 79 |
| 79 | 5 | 38 | 44.06 | -69 | 6 | 59.76 | 14.22 | 13.82 | 13.13 | 11.83 | 203 |
| 80 | 5 | 38 | 15.67 | -69 | 4 | 37.2 | 16.24 | 15.48 | 14.54 | 14.47 | 298 |
| 81 | 5 | 38 | 46.34 | -69 | 3 | 13.68 | 14.06 | 13.02 | 12.73 | 12.36 | 103 |

| *id* | *RA (J2000)* *h m s* | | | *Dec (J2000)* *d m s* | | | $m_J$ | $m_H$ | $m_K$ | $m_L$ | $id_{IRAF}$ |
|---|---|---|---|---|---|---|---|---|---|---|---|
| 82 | 5 | 38 | 8.78 | -69 | 3 | 45 | 13.57 | 12.71 | 12.48 | 12.15 | 162 |
| 83 | 5 | 37 | 54.62 | -69 | 9 | 3.24 | 10.36 | 9.43 | 9.16 | 9.06 | 178 |
| 84 | 5 | 38 | 41.38 | -69 | 3 | 54 | 15.74 | 13.34 | 11.52 | 8.79 | 100 |
| 85 | 5 | 38 | 45.10 | -69 | 5 | 8.88 | 12.35 | 12.10 | 11.95 | 10.24 | 78 |
| 86 | 5 | 38 | 39.46 | -69 | 6 | 6.48 | 12.78 | 12.63 | 13.32 | 14.23 | 188 |
| 87 | 5 | 38 | 23.54 | -69 | 8 | 29.4 | 15.19 | 14.45 | 14.43 | 13.39 | 184 |
| 88 | 5 | 38 | 20.90 | -69 | 3 | 50.04 | 12.20 | 11.85 | 11.65 | 11.22 | 140 |
| 89 | 5 | 39 | 18.07 | -69 | 5 | 16.8 | 14.22 | 13.46 | 13.29 | 13.08 | 229 |
| 90 | 5 | 38 | 36.98 | -69 | 5 | 7.8 | 11.55 | 11.52 | 11.40 | 11.24 | 116 |
| 91 | 5 | 38 | 44.26 | -69 | 6 | 6.12 | 11.93 | 11.78 | 11.53 | 11.07 | 63 |
| 92 | 5 | 38 | 38.86 | -69 | 8 | 14.64 | 11.23 | 10.90 | 10.76 | 10.35 | 38 |
| 93 | 5 | 38 | 56.54 | -69 | 4 | 16.68 | 16.94 | 15.04 | 14.66 | 10.89 | 85 |
| 94 | 5 | 39 | 3.79 | -69 | 3 | 46.44 | 14.86 | 14.38 | 13.67 | 13.60 | 315 |
| 95 | 5 | 38 | 56.21 | -69 | 8 | 41.28 | 14.11 | 13.01 | 12.71 | 12.39 | 193 |
| 96 | 5 | 39 | 12.53 | -69 | 2 | 9.6 | 12.83 | 12.60 | 12.49 | 12.30 | 173 |
| 97 | 5 | 38 | 41.26 | -69 | 8 | 43.44 | 16.29 | 15.46 | 14.69 | 13.56 | 207 |
| 98 | 5 | 37 | 56.98 | -69 | 3 | 38.88 | 13.03 | 12.02 | 11.77 | 10.82 | 164 |
| 99 | 5 | 38 | 42.84 | -69 | 9 | 28.8 | 12.38 | 11.12 | 10.36 | 9.56 | 30 |
| 100 | 5 | 38 | 42.55 | -69 | 1 | 2.28 | 12.76 | 12.73 | 12.71 | 12.18 | 155 |
| 101 | 5 | 38 | 40.18 | -69 | 9 | 33.12 | 14.75 | 13.91 | 13.67 | 13.74 | 187 |
| 102 | 5 | 38 | 9.96 | -69 | 3 | 43.2 | 12.47 | 11.21 | 10.50 | 9.68 | 163 |
| 103 | 5 | 38 | 48.31 | -69 | 4 | 44.76 | 13.43 | 12.86 | 12.35 | 11.15 | 81 |
| 104 | 5 | 38 | 54.70 | -69 | 7 | 44.76 | 10.68 | 10.21 | 10.10 | 10.06 | 26 |
| 105 | 5 | 38 | 31.63 | -69 | 2 | 14.64 | 14.53 | 13.80 | 12.68 | 10.34 | 170 |
| 106 | 5 | 38 | 29.42 | -69 | 8 | 21.48 | 15.12 | 14.06 | 13.89 | 13.46 | 183 |
| 107 | 5 | 39 | 0.48 | -69 | 8 | 41.28 | 13.76 | 13.40 | 13.30 | 12.67 | 192 |
| 108 | 5 | 38 | 42.36 | -69 | 4 | 58.08 | 11.60 | 11.41 | 11.31 | 11.41 | 80 |
| 109 | 5 | 38 | 31.34 | -69 | 8 | 16.08 | 13.71 | 12.84 | 12.61 | 12.29 | 125 |
| 110 | 5 | 38 | 38.45 | -69 | 6 | 29.52 | 13.68 | 13.63 | 12.77 | 11.17 | 205 |
| 111 | 5 | 39 | 32.93 | -69 | 3 | 40.68 | 14.35 | 13.37 | 12.99 | 12.58 | 112 |
| 112 | 5 | 38 | 38.83 | -69 | 6 | 49.68 | 12.72 | 12.52 | 12.31 | 12.13 | 44 |
| 113 | 5 | 38 | 51.62 | -69 | 8 | 7.44 | 10.54 | 10.27 | 10.09 | 9.78 | 27 |
| 114 | 5 | 38 | 39.34 | -69 | 5 | 52.44 | 13.57 | 13.68 | 13.13 | 11.71 | 70 |
| 115 | 5 | 38 | 49.75 | -69 | 6 | 43.2 | 12.50 | 12.47 | 12.19 | 11.22 | 43 |
| 116 | 5 | 39 | 4.78 | -69 | 4 | 9.84 | 12.35 | 12.20 | 12.09 | 11.72 | 87 |
| 117 | 5 | 38 | 30.00 | -69 | 6 | 25.92 | 13.60 | 12.94 | 12.82 | 11.65 | 123 |
| 118 | 5 | 38 | 36.12 | -69 | 5 | 57.84 | 10.78 | 10.58 | 10.47 | 10.35 | 118 |
| 119 | 5 | 38 | 36.41 | -69 | 6 | 57.6 | 12.10 | 11.84 | 11.49 | 10.98 | 45 |
| 120 | 5 | 38 | 50.04 | -69 | 3 | 38.52 | 14.00 | 13.39 | 12.88 | 12.24 | 101 |
| 121 | 5 | 39 | 35.47 | -69 | 4 | 39 | 13.55 | 12.91 | 12.77 | 12.76 | 110 |
| 122 | 5 | 39 | 29.71 | -69 | 3 | 42.12 | 13.14 | 12.22 | 11.93 | 11.62 | 113 |
| 123 | 5 | 38 | 39.82 | -69 | 6 | 34.92 | 14.09 | 14.19 | 13.31 | 11.54 | 204 |
| 124 | 5 | 39 | 12.50 | -69 | 4 | 9.12 | 13.18 | 12.79 | 12.72 | 12.62 | 88 |
| 125 | 5 | 38 | 51.05 | -69 | 8 | 55.68 | 14.31 | 13.46 | 13.23 | 13.01 | 194 |
| 126 | 5 | 38 | 40.85 | -69 | 10 | 9.12 | 13.55 | 12.75 | 12.54 | 12.51 | 32 |
| 127 | 5 | 39 | 25.73 | -69 | 11 | 36.24 | 9.03 | 8.47 | 8.39 | 8.22 | 6 |
| 128 | 5 | 39 | 33.62 | -69 | 8 | 54.96 | 13.52 | 12.68 | 12.41 | 12.40 | 21 |

| *id* | *RA (J2000)* *h m s* | | | *Dec (J2000)* *d m s* | | | $m_J$ | $m_H$ | $m_K$ | $m_L$ | $id_{IRAF}$ |
|---|---|---|---|---|---|---|---|---|---|---|---|
| 129 | 5 | 39 | 34.37 | -69 | 10 | 44.76 | 13.81 | 12.83 | 12.52 | 12.11 | 14 |
| 130 | 5 | 39 | 43.61 | -69 | 10 | 39.72 | 13.39 | 12.56 | 12.35 | 12.06 | 13 |
| 131 | 5 | 39 | 38.47 | -69 | 9 | 0.36 | 14.26 | 13.57 | 12.32 | 10.48 | 20 |
| 132 | 5 | 38 | 52.58 | -69 | 11 | 24.36 | 12.43 | 11.34 | 11.05 | 10.65 | 7 |
| 133 | 5 | 39 | 45.50 | -69 | 9 | 37.08 | 14.05 | 12.99 | 12.67 | 12.30 | 12 |
| 134 | 5 | 38 | 29.88 | -69 | 11 | 16.44 | 12.43 | 11.35 | 10.91 | 10.40 | 10 |
| 135 | 5 | 39 | 28.92 | -69 | 6 | 56.88 | 14.68 | 13.73 | 13.48 | 13.31 | 223 |
| 136 | 5 | 39 | 19.78 | -69 | 10 | 10.92 | 13.12 | 12.00 | 11.47 | 10.89 | 16 |
| 137 | 5 | 39 | 52.39 | -69 | 9 | 41.04 | 10.69 | 9.75 | 9.42 | 9.28 | 11 |
| 138 | 5 | 38 | 57.74 | -69 | 10 | 40.08 | 13.65 | 12.53 | 12.11 | 11.43 | 15 |
| 139 | 5 | 39 | 39.91 | -69 | 6 | 36.36 | 13.01 | 12.09 | 11.81 | 11.55 | 54 |
| 140 | 5 | 39 | 36.53 | -69 | 8 | 48.84 | 13.58 | 12.72 | 12.56 | 12.72 | 196 |
| 141 | 5 | 39 | 39.41 | -69 | 11 | 52.08 | 9.92 | 8.77 | 8.54 | 8.76 | 3 |
| 142 | 5 | 39 | 18.17 | -69 | 8 | 48.48 | 13.86 | 13.58 | 13.64 | 13.31 | 195 |
| 143 | 5 | 39 | 11.42 | -69 | 8 | 25.08 | 14.10 | 12.42 | 11.26 | 10.22 | 23 |
| 144 | 5 | 39 | 16.32 | -69 | 7 | 34.32 | 14.43 | 13.25 | 12.87 | 12.83 | 22 |
| 145 | 5 | 38 | 6.17 | -69 | 2 | 35.16 | 11.83 | 10.90 | 10.31 | 10.10 | 160 |
| 146 | 5 | 38 | 5.62 | -69 | 9 | 9.72 | 15.39 | 14.48 | 13.28 | 11.17 | 176 |
| 147 | 5 | 37 | 50.47 | -69 | 4 | 2.28 | 14.78 | 12.99 | 11.48 | 9.37 | 165 |
| 148 | 5 | 38 | 5.47 | -69 | 9 | 26.64 | 13.29 | 12.22 | 11.88 | 11.26 | 175 |
| 149 | 5 | 39 | 36.10 | -69 | 5 | 15.72 | 13.97 | 13.18 | 12.86 | 12.92 | 97 |
| 150 | 5 | 38 | 12.72 | -69 | 2 | 54.24 | 14.35 | 13.38 | 13.18 | 12.82 | 159 |
| 151 | 5 | 38 | 18.29 | -69 | 4 | 2.28 | 12.48 | 12.35 | 12.34 | 12.32 | 136 |
| 152 | 5 | 38 | 14.88 | -69 | 3 | 48.6 | 12.52 | 12.43 | 12.44 | 12.26 | 139 |
| 153 | 5 | 39 | 44.69 | -69 | 4 | 30.36 | 12.91 | 12.29 | 12.12 | 12.13 | 174 |
| 154 | 5 | 39 | 32.11 | -69 | 5 | 43.8 | 13.89 | 12.72 | 12.37 | 12.07 | 95 |
| 155 | 5 | 37 | 49.03 | -69 | 5 | 8.16 | 11.03 | 10.96 | 10.85 | 11.90 | 167 |
| 156 | 5 | 39 | 32.02 | -69 | 4 | 40.8 | 13.07 | 12.05 | 11.61 | 11.18 | 109 |
| 157 | 5 | 38 | 21.38 | -69 | 9 | 48.96 | 13.20 | 12.15 | 11.80 | 11.37 | 9 |
| 158 | 5 | 39 | 29.33 | -69 | 5 | 18.6 | 15.06 | 14.35 | 14.06 | 13.67 | 242 |
| 159 | 5 | 39 | 37.80 | -69 | 5 | 0.96 | 12.41 | 11.32 | 11.00 | 10.80 | 98 |
| 160 | 5 | 37 | 50.21 | -69 | 4 | 24.24 | 10.03 | 9.53 | 9.47 | 9.67 | 166 |
| 161 | 5 | 39 | 20.23 | -69 | 6 | 26.28 | 12.01 | 11.87 | 11.79 | 11.74 | 56 |
| 162 | 5 | 38 | 15.98 | -69 | 10 | 11.28 | 9.32 | 8.38 | 7.91 | 7.44 | 8 |
| 163 | 5 | 39 | 41.76 | -69 | 11 | 30.84 | 10.30 | 9.38 | 8.96 | 8.59 | 2 |
| 164 | 5 | 39 | 39.41 | -69 | 11 | 52.08 | 9.92 | 8.77 | 8.54 | 8.13 | 4 |
| 165 | 5 | 39 | 37.92 | -69 | 11 | 46.32 | 10.91 | 10.29 | 10.10 | 9.79 | 5 |
| 166 | 5 | 38 | 37.97 | -69 | 7 | 30.36 | - | - | 13.99 | 11.90 | 201 |
| 167 | 5 | 38 | 39.14 | -69 | 6 | 21.24 | - | - | 11.43 | 11.22 | 48 |
| 168 | 5 | 38 | 35.95 | -69 | 6 | 9.36 | - | - | 11.91 | 12.62 | 121 |
| 169 | 5 | 38 | 42.14 | -69 | 5 | 56.04 | - | - | 11.54 | 11.46 | 66 |
| 170 | 5 | 38 | 39.67 | -69 | 5 | 38.4 | - | - | 13.17 | 9.67 | 72 |
| 171 | 5 | 38 | 40.87 | -69 | 6 | 3.24 | - | - | 11.70 | 10.47 | 67 |
| 172 | 5 | 38 | 38.57 | -69 | 6 | 12.96 | - | - | 14.29 | 14.12 | 71 |
| 173 | 5 | 38 | 45.10 | -69 | 5 | 0.24 | - | - | 12.97 | 11.31 | 189 |
| 174 | 5 | 38 | 42.41 | -69 | 6 | 15.12 | - | - | 11.64 | 11.03 | 62 |
| 175 | 5 | 38 | 41.30 | -69 | 5 | 31.92 | - | - | 13.09 | 13.80 | 218 |

| *id* | *RA (J2000)* *h m s* | | | *Dec (J2000)* *d m s* | | | $m_J$ | $m_H$ | $m_K$ | $m_L$ | $id_{IRAF}$ |
|---|---|---|---|---|---|---|---|---|---|---|---|
| 176 | 5 | 38 | 54.31 | -69 | 4 | 37.56 | - | - | 15.22 | 12.21 | 280 |
| 177 | 5 | 38 | 49.68 | -69 | 3 | 44.28 | - | - | 15.07 | 13.45 | 308 |
| 178 | 5 | 38 | 52.99 | -69 | 3 | 21.6 | - | - | 13.83 | 13.59 | 310 |
| 179 | 5 | 38 | 46.78 | -69 | 5 | 5.64 | - | - | 12.53 | 10.25 | 76 |
| 180 | 5 | 38 | 48.17 | -69 | 4 | 40.8 | - | - | 12.51 | 11.08 | 284 |
| 181 | 5 | 38 | 54.31 | -69 | 5 | 0.24 | - | - | 12.31 | 10.88 | 291 |
| 182 | 5 | 38 | 53.59 | -69 | 4 | 58.08 | - | - | 12.15 | 10.94 | 290 |
| 183 | 5 | 38 | 32.02 | -69 | 7 | 44.04 | - | - | 13.67 | 11.78 | 124 |
| 184 | 5 | 38 | 15.31 | -69 | 6 | 55.08 | - | - | 15.59 | 12.62 | 146 |
| 185 | 5 | 38 | 36.50 | -69 | 5 | 22.56 | - | - | 13.62 | 11.33 | 117 |
| 186 | 5 | 38 | 34.73 | -69 | 6 | 5.4 | - | - | 12.40 | 11.51 | 120 |
| 187 | 5 | 38 | 41.33 | -69 | 6 | 14.4 | - | - | 13.23 | 11.62 | 61 |
| 188 | 5 | 39 | 7.92 | -69 | 4 | 3 | - | - | 14.98 | 13.06 | 264 |
| 189 | 5 | 38 | 48.96 | -69 | 4 | 45.12 | - | - | 13.32 | 10.48 | 82 |
| 190 | 5 | 38 | 59.26 | -69 | 5 | 9.24 | - | - | 13.23 | 12.32 | 293 |
| 191 | 5 | 38 | 50.50 | -69 | 5 | 2.04 | - | - | 12.66 | 11.67 | 289 |
| 192 | 5 | 38 | 43.34 | -69 | 5 | 21.12 | - | - | 14.71 | 14.06 | 217 |
| 193 | 5 | 39 | 55.49 | -69 | 10 | 31.8 | - | - | - | 11.84 | 1 |
| 194 | 5 | 39 | 58.37 | -69 | 6 | 8.64 | - | - | - | 12.63 | 107 |
| 195 | 5 | 38 | 33.14 | -69 | 6 | 11.52 | - | - | - | 11.80 | 122 |
| 196 | 5 | 38 | 34.13 | -69 | 4 | 52.32 | - | - | - | 10.45 | 128 |
| 197 | 5 | 39 | 26.14 | -69 | 11 | 28.68 | - | - | - | 13.49 | 197 |
| 198 | 5 | 38 | 55.92 | -69 | 5 | 38.04 | - | - | - | 11.51 | 221 |
| 199 | 5 | 39 | 9.34 | -69 | 3 | 53.28 | - | - | - | 13.31 | 262 |
| 200 | 5 | 39 | 8.26 | -69 | 3 | 57.6 | - | - | - | 13.40 | 263 |
| 201 | 5 | 39 | 5.04 | -69 | 4 | 14.88 | - | - | - | 13.33 | 267 |
| 202 | 5 | 39 | 2.62 | -69 | 4 | 23.16 | - | - | - | 12.82 | 269 |
| 203 | 5 | 39 | 9.46 | -69 | 4 | 36.84 | - | - | - | 13.45 | 270 |
| 204 | 5 | 39 | 2.26 | -69 | 4 | 41.52 | - | - | - | 13.42 | 275 |
| 205 | 5 | 38 | 59.90 | -69 | 4 | 19.56 | - | - | - | 12.48 | 276 |
| 206 | 5 | 38 | 58.34 | -69 | 4 | 28.2 | - | - | - | 12.01 | 277 |
| 207 | 5 | 38 | 55.06 | -69 | 4 | 36.84 | - | - | - | 13.31 | 279 |
| 208 | 5 | 38 | 51.55 | -69 | 4 | 41.52 | - | - | - | 12.76 | 282 |
| 209 | 5 | 38 | 48.82 | -69 | 4 | 40.44 | - | - | - | 11.14 | 283 |
| 210 | 5 | 38 | 47.14 | -69 | 4 | 40.08 | - | - | - | 11.98 | 285 |
| 211 | 5 | 38 | 45.26 | -69 | 4 | 41.88 | - | - | - | 11.99 | 286 |
| 212 | 5 | 38 | 45.58 | -69 | 4 | 56.28 | - | - | - | 11.20 | 288 |
| 213 | 5 | 38 | 55.10 | -69 | 5 | 21.84 | - | - | - | 12.60 | 292 |
| 214 | 5 | 38 | 37.42 | -69 | 2 | 51 | - | - | - | 13.19 | 321 |
| 215 | 5 | 38 | 42.86 | -69 | 6 | 4.68 | - | - | - | 9.70 | 64 |
| 216 | 5 | 38 | 40.25 | -69 | 5 | 60 | - | - | 0.00 | 12.05 | 69 |

*Table 1: Coordinates and magnitudes for sources in 30 Doradus.*

## RCW 57

| *id* | *RA (J2000)* *h m s* | | | *Dec (J2000)* *d m s* | | | $m_J$ | $m_H$ | $m_K$ | $m_L$ | $id_{IRAF}$ |
|---|---|---|---|---|---|---|---|---|---|---|---|
| 1 | 11 | 11 | 37.06 | -61 | 18 | 8.64 | 13.58 | 12.04 | 11.07 | 8.70 | 309 |
| 2 | 11 | 11 | 50.16 | -61 | 20 | 22.56 | 10.64 | 9.94 | 9.75 | 9.63 | 257 |
| 3 | 11 | 11 | 55.34 | -61 | 18 | 45 | 15.45 | 13.78 | 12.20 | 9.45 | 216 |
| 4 | 11 | 11 | 40.94 | -61 | 20 | 22.2 | 9.71 | 9.08 | 8.90 | 8.86 | 297 |
| 5 | 11 | 11 | 42.55 | -61 | 18 | 46.44 | 16.99 | 16.81 | 12.69 | 10.69 | 291 |
| 6 | 11 | 11 | 42.50 | -61 | 16 | 25.32 | 11.63 | 9.69 | 8.88 | 8.15 | 296 |
| 7 | 11 | 11 | 47.74 | -61 | 18 | 30.6 | 12.46 | 10.91 | 9.95 | 8.43 | 274 |
| 8 | 11 | 11 | 33.38 | -61 | 20 | 19.68 | 16.78 | 15.67 | 10.44 | 7.54 | 321 |
| 9 | 11 | 12 | 12.34 | -61 | 15 | 28.8 | 16.49 | 15.35 | 14.62 | 10.05 | 131 |
| 10 | 11 | 11 | 39.67 | -61 | 19 | 30 | 16.34 | 14.46 | 13.26 | 10.63 | 301 |
| 11 | 11 | 12 | 15.98 | -61 | 21 | 42.84 | 15.86 | 15.17 | 14.48 | 11.76 | 102 |
| 12 | 11 | 11 | 54.84 | -61 | 18 | 30.6 | 13.46 | 10.85 | 9.58 | 8.02 | 220 |
| 13 | 11 | 11 | 57.00 | -61 | 18 | 1.8 | 12.53 | 11.26 | 10.36 | 8.19 | 201 |
| 14 | 11 | 11 | 43.15 | -61 | 18 | 39.24 | 16.09 | 14.50 | 13.46 | 10.06 | 289 |
| 15 | 11 | 11 | 31.58 | -61 | 17 | 23.64 | 13.16 | 11.77 | 11.11 | 10.44 | 329 |
| 16 | 11 | 11 | 53.28 | -61 | 15 | 5.04 | 13.34 | 11.76 | 10.84 | 10.07 | 247 |
| 17 | 11 | 11 | 51.84 | -61 | 14 | 20.4 | 12.96 | 11.35 | 10.76 | 10.34 | 264 |
| 18 | 11 | 11 | 53.21 | -61 | 18 | 22.32 | 11.21 | 9.87 | 7.54 | 4.15 | 276 |
| 19 | 11 | 12 | 30.72 | -61 | 21 | 18.72 | 15.61 | 15.04 | 14.42 | 10.32 | 25 |
| 20 | 11 | 11 | 39.46 | -61 | 11 | 34.8 | 15.55 | 14.97 | 15.09 | 10.96 | 310 |
| 21 | 11 | 12 | 32.11 | -61 | 23 | 53.88 | 15.17 | 13.64 | 12.89 | 8.62 | 18 |
| 22 | 11 | 11 | 41.14 | -61 | 22 | 29.28 | 17.62 | 13.36 | 10.28 | 8.17 | 290 |
| 23 | 11 | 11 | 58.32 | -61 | 16 | 34.32 | 15.51 | 14.06 | 13.52 | 11.72 | 200 |
| 24 | 11 | 11 | 31.92 | -61 | 16 | 12.72 | 14.86 | 14.25 | 13.80 | 11.30 | 330 |
| 25 | 11 | 11 | 47.76 | -61 | 16 | 17.4 | 13.44 | 11.57 | 10.74 | 9.70 | 281 |
| 26 | 11 | 12 | 29.66 | -61 | 23 | 21.12 | 15.89 | 15.40 | 12.40 | 8.77 | 34 |
| 27 | 11 | 11 | 53.47 | -61 | 18 | 4.68 | 13.66 | 13.23 | 11.34 | 8.26 | 236 |
| 28 | 11 | 11 | 56.18 | -61 | 21 | 46.44 | 14.44 | 13.86 | 13.76 | 12.33 | 196 |
| 29 | 11 | 11 | 38.57 | -61 | 22 | 22.44 | 16.77 | 16.98 | 12.05 | 8.62 | 302 |
| 30 | 11 | 11 | 42.50 | -61 | 18 | 15.48 | 17.90 | 14.62 | 12.67 | 10.98 | 292 |
| 31 | 11 | 11 | 31.73 | -61 | 21 | 46.8 | 10.42 | 9.76 | 9.41 | 8.83 | 323 |
| 32 | 11 | 12 | 12.82 | -61 | 15 | 13.32 | 17.47 | 13.73 | 12.06 | 11.73 | 130 |
| 33 | 11 | 11 | 21.22 | -61 | 18 | 42.84 | 14.84 | 13.45 | 12.89 | 12.03 | 358 |
| 34 | 11 | 11 | 33.62 | -61 | 21 | 35.64 | 14.14 | 13.25 | 13.96 | 9.24 | 317 |
| 35 | 11 | 11 | 54.38 | -61 | 18 | 24.12 | 11.99 | 10.59 | 9.03 | 6.53 | 225 |
| 36 | 11 | 11 | 53.93 | -61 | 18 | 28.44 | 11.28 | 10.20 | 10.56 | 7.09 | 224 |
| 37 | 11 | 11 | 51.74 | -61 | 22 | 4.08 | 16.21 | 15.04 | 14.98 | 10.91 | 228 |
| 38 | 11 | 11 | 34.63 | -61 | 21 | 37.08 | 13.87 | 12.59 | 11.77 | 8.71 | 311 |
| 39 | 11 | 11 | 59.86 | -61 | 21 | 38.88 | 16.57 | 15.18 | 14.37 | 10.42 | 171 |
| 40 | 11 | 11 | 24.43 | -61 | 20 | 49.56 | 17.37 | 13.59 | 11.81 | 10.48 | 347 |
| 41 | 11 | 11 | 30.14 | -61 | 17 | 23.64 | 12.96 | 11.04 | 10.23 | 9.64 | 333 |

| *id* | *RA (J2000)* *h m s* | | | *Dec (J2000)* *d m s* | | | $m_J$ | $m_H$ | $m_K$ | $m_L$ | $id_{IRAF}$ |
|---|---|---|---|---|---|---|---|---|---|---|---|
| 42 | 11 | 11 | 36.62 | -61 | 12 | 4.68 | 15.80 | 15.18 | 14.97 | 10.81 | 320 |
| 43 | 11 | 11 | 35.28 | -61 | 18 | 25.2 | 15.75 | 14.30 | 13.37 | 12.02 | 315 |
| 44 | 11 | 12 | 4.80 | -61 | 22 | 45.12 | 16.65 | 15.59 | 14.46 | 12.00 | 150 |
| 45 | 11 | 11 | 45.12 | -61 | 14 | 24.36 | 16.45 | 14.99 | 14.34 | 10.96 | 284 |
| 46 | 11 | 11 | 57.82 | -61 | 14 | 30.48 | 15.04 | 14.53 | 14.24 | 10.30 | 210 |
| 47 | 11 | 11 | 43.18 | -61 | 19 | 15.6 | 16.37 | 15.00 | 13.89 | 12.88 | 288 |
| 48 | 11 | 11 | 26.62 | -61 | 18 | 39.96 | 14.44 | 12.02 | 10.94 | 9.65 | 343 |
| 49 | 11 | 12 | 18.05 | -61 | 21 | 9 | 16.38 | 15.51 | 14.73 | 11.85 | 92 |
| 50 | 11 | 11 | 39.84 | -61 | 14 | 49.2 | 13.65 | 11.56 | 10.66 | 10.26 | 303 |
| 51 | 11 | 11 | 54.38 | -61 | 22 | 4.08 | 10.52 | 9.73 | 9.26 | 8.70 | 213 |
| 52 | 11 | 11 | 47.09 | -61 | 13 | 49.08 | 10.32 | 9.70 | 9.53 | 10.60 | 283 |
| 53 | 11 | 11 | 56.28 | -61 | 16 | 10.2 | 11.74 | 10.30 | 9.70 | 9.41 | 214 |
| 54 | 11 | 11 | 54.17 | -61 | 14 | 50.28 | 11.76 | 10.86 | 10.14 | 9.01 | 244 |
| 55 | 11 | 11 | 51.07 | -61 | 18 | 14.4 | 12.59 | 12.75 | 11.41 | 7.58 | 269 |
| 56 | 11 | 12 | 0.24 | -61 | 15 | 27 | 14.42 | 12.89 | 11.96 | 11.41 | 184 |
| 57 | 11 | 11 | 17.81 | -61 | 17 | 60 | 10.93 | 10.76 | 10.72 | 11.57 | 367 |
| 58 | 11 | 11 | 43.54 | -61 | 14 | 33.36 | 12.74 | 10.62 | 9.63 | 8.93 | 295 |
| 59 | 11 | 11 | 47.33 | -61 | 15 | 25.2 | 13.46 | 11.66 | 10.90 | 10.45 | 279 |
| 60 | 11 | 11 | 56.62 | -61 | 17 | 18.24 | 13.50 | 12.46 | 11.74 | 11.07 | 209 |
| 61 | 11 | 11 | 28.15 | -61 | 16 | 10.92 | 13.88 | 13.65 | 13.51 | 12.08 | 341 |
| 62 | 11 | 10 | 59.88 | -61 | 18 | 39.6 | 15.12 | 14.62 | 14.32 | 9.67 | 381 |
| 63 | 11 | 11 | 50.04 | -61 | 16 | 30 | 17.43 | 14.75 | 12.66 | 13.46 | 270 |
| 64 | 11 | 11 | 56.47 | -61 | 18 | 55.08 | 13.46 | 13.18 | 10.85 | 7.91 | 202 |
| 65 | 11 | 12 | 0.89 | -61 | 18 | 22.68 | 12.98 | 11.11 | 10.11 | 8.09 | 177 |
| 66 | 11 | 11 | 49.34 | -61 | 13 | 9.12 | 10.25 | 8.91 | 8.39 | 8.01 | 275 |
| 67 | 11 | 11 | 51.22 | -61 | 14 | 53.52 | 12.77 | 11.16 | 10.54 | 10.76 | 265 |
| 68 | 11 | 11 | 36.36 | -61 | 16 | 54.84 | 16.31 | 15.22 | 14.62 | 11.93 | 313 |
| 69 | 11 | 11 | 59.52 | -61 | 20 | 26.52 | 14.56 | 13.53 | 13.44 | 9.92 | 186 |
| 70 | 11 | 12 | 39.65 | -61 | 21 | 34.92 | 14.66 | 13.38 | 12.97 | 8.74 | 13 |
| 71 | 11 | 11 | 20.04 | -61 | 17 | 24 | 12.24 | 11.11 | 10.70 | 10.16 | 361 |
| 72 | 11 | 11 | 47.86 | -61 | 13 | 24.6 | 10.18 | 9.71 | 9.55 | 9.76 | 282 |
| 73 | 11 | 11 | 38.06 | -61 | 19 | 4.44 | 12.63 | 12.13 | 11.87 | 9.88 | 307 |
| 74 | 11 | 12 | 4.10 | -61 | 21 | 11.16 | 13.01 | 10.85 | 9.97 | 9.43 | 157 |
| 75 | 11 | 11 | 39.58 | -61 | 13 | 54.48 | 12.33 | 11.49 | 11.27 | 11.74 | 305 |
| 76 | 11 | 11 | 24.07 | -61 | 17 | 12.12 | 12.25 | 11.49 | 10.89 | 10.65 | 353 |
| 77 | 11 | 11 | 14.64 | -61 | 15 | 30.96 | 12.09 | 14.34 | 10.89 | 8.88 | 372 |
| 78 | 11 | 11 | 24.89 | -61 | 18 | 16.56 | 10.47 | 10.30 | 10.15 | 9.87 | 349 |
| 79 | 11 | 11 | 46.22 | -61 | 14 | 30.84 | 15.76 | 14.18 | 13.58 | 11.74 | 286 |
| 80 | 11 | 11 | 53.50 | -61 | 18 | 49.32 | 16.14 | 15.04 | 11.45 | 7.98 | 234 |
| 81 | 11 | 11 | 17.69 | -61 | 19 | 39.72 | 12.25 | 12.12 | 12.02 | 10.56 | 366 |
| 82 | 11 | 12 | 8.83 | -61 | 14 | 24 | 10.81 | 10.61 | 10.53 | 10.27 | 144 |
| 83 | 11 | 12 | 20.45 | -61 | 17 | 7.8 | 15.33 | 14.97 | 14.85 | 11.17 | 91 |

| *id* | *RA (J2000)* *h m s* | | | *Dec (J2000)* *d m s* | | | $m_J$ | $m_H$ | $m_K$ | $m_L$ | $id_{IRAF}$ |
|---|---|---|---|---|---|---|---|---|---|---|---|
| 84 | 11 | 11 | 37.99 | -61 | 12 | 5.4 | 12.66 | 11.55 | 11.16 | 10.22 | 314 |
| 85 | 11 | 12 | 2.47 | -61 | 15 | 2.16 | 10.48 | 9.28 | 8.87 | 8.58 | 176 |
| 86 | 11 | 11 | 56.30 | -61 | 14 | 3.12 | 12.67 | 10.69 | 9.88 | 9.35 | 221 |
| 87 | 11 | 12 | 3.91 | -61 | 19 | 58.08 | 13.82 | 13.28 | 13.09 | 9.43 | 164 |
| 88 | 11 | 11 | 28.37 | -61 | 18 | 8.64 | 15.29 | 14.26 | 13.63 | 10.49 | 337 |
| 89 | 11 | 12 | 2.78 | -61 | 19 | 40.8 | 13.08 | 10.11 | 8.67 | 7.69 | 166 |
| 90 | 11 | 11 | 54.26 | -61 | 22 | 11.28 | 14.61 | 13.86 | 14.38 | 12.17 | 218 |
| 91 | 11 | 11 | 33.00 | -61 | 23 | 51.72 | 11.72 | 9.24 | 8.07 | 7.32 | 316 |
| 92 | 11 | 11 | 54.60 | -61 | 13 | 48.36 | 12.72 | 11.30 | 10.83 | 11.44 | 242 |
| 93 | 11 | 11 | 51.98 | -61 | 18 | 37.44 | 13.64 | 11.88 | 10.10 | 6.64 | 248 |
| 94 | 11 | 11 | 53.71 | -61 | 19 | 4.44 | 16.11 | 13.62 | 11.49 | 8.23 | 396 |
| 95 | 11 | 11 | 51.79 | -61 | 18 | 20.52 | 13.04 | 12.21 | 9.36 | 7.10 | 260 |
| 96 | 11 | 11 | 53.33 | -61 | 19 | 40.08 | 14.74 | 12.82 | 12.27 | 8.40 | 271 |
| 97 | 11 | 11 | 33.86 | -61 | 11 | 35.16 | 9.00 | 8.18 | 7.85 | 7.53 | 327 |
| 98 | 11 | 12 | 8.64 | -61 | 18 | 28.08 | 15.63 | 15.03 | 14.85 | 10.31 | 140 |
| 99 | 11 | 11 | 42.84 | -61 | 12 | 57.24 | 11.80 | 11.01 | 10.58 | 9.93 | 299 |
| 100 | 11 | 11 | 29.26 | -61 | 21 | 36 | 14.77 | 14.80 | 14.14 | 10.12 | 325 |
| 101 | 11 | 12 | 28.92 | -61 | 21 | 40.32 | 14.69 | 14.30 | 13.27 | 9.72 | 30 |
| 102 | 11 | 11 | 34.34 | -61 | 13 | 16.68 | 12.33 | 10.87 | 10.32 | 9.74 | 324 |
| 103 | 11 | 12 | 8.45 | -61 | 16 | 31.8 | 9.65 | 9.46 | 9.35 | 9.26 | 142 |
| 104 | 11 | 12 | 9.96 | -61 | 18 | 44.28 | 8.87 | 8.92 | 8.86 | 9.03 | 133 |
| 105 | 11 | 11 | 19.51 | -61 | 20 | 9.6 | 12.40 | 10.18 | 9.25 | 8.60 | 360 |
| 106 | 11 | 11 | 16.68 | -61 | 21 | 19.8 | 18.08 | 13.93 | 12.05 | 10.64 | 364 |
| 107 | 11 | 11 | 22.39 | -61 | 16 | 7.68 | 10.43 | 9.63 | 9.28 | 8.96 | 357 |
| 108 | 11 | 12 | 32.69 | -61 | 20 | 16.8 | 13.66 | 12.60 | 12.29 | 10.91 | 23 |
| 109 | 11 | 12 | 8.04 | -61 | 15 | 54 | 12.15 | 11.24 | 10.82 | 10.57 | 146 |
| 110 | 11 | 11 | 58.32 | -61 | 11 | 54.24 | 13.95 | 12.99 | 12.69 | 10.64 | 211 |
| 111 | 11 | 11 | 12.38 | -61 | 17 | 10.32 | 15.25 | 12.47 | 12.33 | 8.97 | 374 |
| 112 | 11 | 12 | 4.42 | -61 | 18 | 6.84 | 13.09 | 13.59 | 12.43 | 8.64 | 162 |
| 113 | 11 | 11 | 26.93 | -61 | 13 | 10.92 | 15.76 | 13.14 | 12.62 | 9.86 | 386 |
| 114 | 11 | 13 | 4.06 | -61 | 17 | 41.64 | 16.18 | 15.48 | 14.20 | 8.10 | 1 |
| 115 | 11 | 11 | 58.68 | -61 | 17 | 51 | 13.44 | 12.14 | 11.36 | 8.70 | 208 |
| 116 | 11 | 12 | 6.14 | -61 | 22 | 31.8 | 13.97 | 13.75 | 13.72 | 12.32 | 151 |
| 117 | 11 | 12 | 12.89 | -61 | 14 | 11.76 | 14.94 | 14.56 | 13.51 | 10.02 | 132 |
| 118 | 11 | 11 | 31.61 | -61 | 22 | 5.16 | 15.69 | 14.50 | 13.71 | 10.60 | 322 |
| 119 | 11 | 11 | 46.87 | -61 | 11 | 31.92 | 9.26 | 9.09 | 9.05 | 9.05 | 287 |
| 120 | 11 | 11 | 24.02 | -61 | 17 | 22.92 | 11.10 | 10.41 | 10.22 | 10.11 | 352 |
| 121 | 11 | 11 | 9.62 | -61 | 15 | 36 | 11.03 | 10.28 | 10.05 | 10.24 | 378 |
| 122 | 11 | 12 | 13.68 | -61 | 17 | 57.48 | 15.37 | 14.94 | 13.91 | 9.95 | 119 |
| 123 | 11 | 12 | 6.70 | -61 | 22 | 19.2 | 14.26 | 12.01 | 11.00 | 10.25 | 141 |
| 124 | 11 | 11 | 59.54 | -61 | 18 | 39.96 | 11.95 | 11.45 | 10.70 | 8.80 | 398 |
| 125 | 11 | 12 | 22.15 | -61 | 11 | 54.96 | 13.24 | 12.35 | 12.05 | 8.81 | 388 |

| *id* | *RA (J2000)* *h m s* | | | *Dec (J2000)* *d m s* | | | $m_J$ | $m_H$ | $m_K$ | $m_L$ | $id_{IRAF}$ |
|---|---|---|---|---|---|---|---|---|---|---|---|
| 126 | 11 | 11 | 32.04 | -61 | 18 | 6.48 | 14.91 | 14.53 | 14.41 | 12.24 | 326 |
| 127 | 11 | 11 | 18.60 | -61 | 16 | 25.68 | 11.14 | 10.17 | 9.77 | 9.51 | 365 |
| 128 | 11 | 11 | 10.61 | -61 | 17 | 45.24 | 8.23 | 7.75 | 7.60 | 7.54 | 377 |
| 129 | 11 | 12 | 14.26 | -61 | 16 | 44.04 | 13.22 | 12.90 | 12.75 | 9.55 | 104 |
| 130 | 11 | 12 | 9.77 | -61 | 15 | 23.76 | 16.96 | 14.63 | 12.75 | 9.96 | 139 |
| 131 | 11 | 12 | 33.38 | -61 | 21 | 4.32 | 14.04 | 13.36 | 13.08 | 11.94 | 21 |
| 132 | 11 | 11 | 35.90 | -61 | 23 | 0.6 | 16.62 | 15.18 | 14.60 | 11.42 | 308 |
| 133 | 11 | 11 | 50.21 | -61 | 12 | 58.68 | 12.34 | 10.93 | 10.44 | 9.96 | 273 |
| 134 | 11 | 12 | 22.49 | -61 | 20 | 51.36 | 16.16 | 15.23 | 14.59 | 11.08 | 76 |
| 135 | 11 | 11 | 47.66 | -61 | 20 | 44.52 | 16.13 | 15.78 | 15.15 | 11.77 | 266 |
| 136 | 11 | 12 | 11.64 | -61 | 17 | 30.12 | 16.48 | 15.57 | 13.54 | 9.44 | 117 |
| 137 | 11 | 11 | 12.36 | -61 | 15 | 20.52 | 11.35 | 10.82 | 10.69 | 11.36 | 375 |
| 138 | 11 | 12 | 25.32 | -61 | 16 | 4.08 | 17.61 | 14.92 | 14.43 | 10.16 | 70 |
| 139 | 11 | 12 | 16.30 | -61 | 21 | 56.52 | 13.29 | 11.84 | 11.26 | 10.85 | 99 |
| 140 | 11 | 12 | 10.01 | -61 | 25 | 43.68 | 10.74 | 9.14 | 8.41 | 7.98 | 121 |
| 141 | 11 | 12 | 0.62 | -61 | 10 | 50.52 | 10.61 | 9.32 | 8.86 | 8.43 | 191 |
| 142 | 11 | 12 | 40.78 | -61 | 16 | 3.36 | 16.97 | 15.41 | 14.95 | 11.20 | 15 |
| 143 | 11 | 11 | 27.94 | -61 | 17 | 1.32 | 16.42 | 15.67 | 14.83 | 11.68 | 340 |
| 144 | 11 | 12 | 7.94 | -61 | 12 | 23.76 | 15.13 | 15.13 | 14.34 | 9.40 | 387 |
| 145 | 11 | 11 | 19.70 | -61 | 15 | 25.92 | 7.98 | 7.42 | 7.27 | 7.15 | 362 |
| 146 | 11 | 11 | 16.75 | -61 | 12 | 51.12 | 8.74 | 7.56 | 7.15 | 6.82 | 371 |
| 147 | 11 | 12 | 21.96 | -61 | 19 | 40.44 | 15.44 | 13.69 | 12.99 | 10.39 | 78 |
| 148 | 11 | 10 | 49.13 | -61 | 18 | 24.84 | 13.45 | 12.44 | 13.44 | 8.31 | 384 |
| 149 | 11 | 11 | 12.43 | -61 | 19 | 9.12 | 12.07 | 10.38 | 9.71 | 10.07 | 373 |
| 150 | 11 | 10 | 55.94 | -61 | 17 | 13.56 | 13.05 | 12.80 | 12.72 | 8.47 | 383 |
| 151 | 11 | 12 | 8.23 | -61 | 14 | 48.84 | 10.41 | 9.79 | 9.66 | 9.67 | 147 |
| 152 | 11 | 12 | 21.46 | -61 | 20 | 48.12 | 16.50 | 15.48 | 14.91 | 11.51 | 79 |
| 153 | 11 | 11 | 51.91 | -61 | 14 | 40.92 | 15.78 | 14.75 | 14.44 | 13.19 | 263 |
| 154 | 11 | 12 | 13.34 | -61 | 13 | 37.92 | 12.53 | 10.85 | 10.22 | 9.84 | 128 |
| 155 | 11 | 12 | 13.68 | -61 | 22 | 21.36 | 14.36 | 12.65 | 11.64 | 10.87 | 115 |
| 156 | 11 | 11 | 55.37 | -61 | 23 | 9.24 | 14.66 | 12.53 | 11.52 | 11.02 | 199 |
| 157 | 11 | 12 | 7.58 | -61 | 17 | 17.16 | 11.39 | 10.80 | 10.63 | 10.15 | 145 |
| 158 | 11 | 12 | 26.21 | -61 | 14 | 38.76 | 14.82 | 11.53 | 10.96 | 9.84 | 68 |
| 159 | 11 | 11 | 15.53 | -61 | 15 | 43.56 | 13.35 | 12.26 | 11.90 | 9.25 | 370 |
| 160 | 11 | 12 | 21.34 | -61 | 16 | 10.56 | 9.98 | 9.35 | 9.18 | 9.36 | 84 |
| 161 | 11 | 12 | 16.32 | -61 | 22 | 36.48 | 16.72 | 15.47 | 14.87 | 11.96 | 95 |
| 162 | 11 | 12 | 17.30 | -61 | 13 | 36.48 | 12.32 | 11.04 | 10.58 | 9.68 | 108 |
| 163 | 11 | 12 | 19.15 | -61 | 20 | 1.32 | 14.86 | 13.99 | 13.52 | 13.34 | 90 |
| 164 | 11 | 12 | 30.12 | -61 | 21 | 14.4 | 14.86 | 14.50 | 13.81 | 10.14 | 44 |
| 165 | 11 | 12 | 18.05 | -61 | 21 | 9 | 16.38 | 15.51 | 14.73 | 10.91 | 96 |
| 166 | 11 | 12 | 23.95 | -61 | 21 | 25.2 | 11.75 | 9.74 | 8.76 | 8.18 | 66 |
| 167 | 11 | 12 | 19.03 | -61 | 15 | 8.64 | 15.86 | 15.35 | 14.96 | 11.61 | 111 |

| *id* | *RA (J2000)* *h m s* | | | *Dec (J2000)* *d m s* | | | $m_J$ | $m_H$ | $m_K$ | $m_L$ | $id_{IRAF}$ |
|---|---|---|---|---|---|---|---|---|---|---|---|
| 168 | 11 | 12 | 29.64 | -61 | 20 | 32.28 | 14.50 | 13.86 | 13.46 | 10.78 | 39 |
| 169 | 11 | 12 | 29.45 | -61 | 21 | 30.96 | 13.76 | 13.42 | 13.55 | 9.68 | 36 |
| 170 | 11 | 12 | 30.89 | -61 | 20 | 36.6 | 14.71 | 14.51 | 14.28 | 10.25 | 37 |
| 171 | 11 | 12 | 24.58 | -61 | 15 | 41.04 | 15.65 | 15.09 | 14.59 | 11.99 | 74 |
| 172 | 11 | 12 | 15.89 | -61 | 22 | 23.52 | 12.96 | 11.17 | 10.37 | 9.56 | 101 |
| 173 | 11 | 12 | 27.02 | -61 | 19 | 54.84 | 14.17 | 12.98 | 12.20 | 11.56 | 55 |
| 174 | 11 | 12 | 31.99 | -61 | 20 | 33.36 | 16.23 | 15.85 | 14.89 | 12.03 | 22 |
| 175 | 11 | 12 | 21.72 | -61 | 14 | 35.16 | 10.43 | 9.10 | 8.58 | 8.22 | 85 |
| 176 | 11 | 12 | 34.34 | -61 | 16 | 48.72 | 12.68 | 12.01 | 11.52 | 10.99 | 19 |
| 177 | 11 | 12 | 25.37 | -61 | 15 | 11.52 | 11.20 | 9.15 | 8.21 | 7.54 | 72 |
| 178 | 11 | 12 | 24.86 | -61 | 19 | 55.56 | 10.62 | 10.59 | 10.54 | 11.24 | 63 |
| 179 | 11 | 12 | 23.42 | -61 | 19 | 10.2 | 16.53 | 15.69 | 15.09 | 12.57 | 69 |
| 180 | 11 | 12 | 13.78 | -61 | 20 | 7.8 | 16.25 | 13.12 | 11.72 | 11.42 | 114 |
| 181 | 11 | 12 | 24.26 | -61 | 23 | 58.2 | 13.24 | 11.25 | 10.42 | 9.88 | 62 |
| 182 | 11 | 12 | 27.34 | -61 | 20 | 13.56 | 14.92 | 13.28 | 12.59 | 11.49 | 50 |
| 183 | 11 | 12 | 14.28 | -61 | 12 | 55.8 | 12.98 | 11.42 | 10.86 | 9.93 | 124 |
| 184 | 11 | 12 | 23.50 | -61 | 16 | 15.24 | 13.81 | 11.24 | 10.04 | 9.33 | 75 |
| 185 | 11 | 12 | 29.57 | -61 | 16 | 21.72 | 12.30 | 11.36 | 10.76 | 9.91 | 46 |
| 186 | 11 | 12 | 23.86 | -61 | 17 | 3.48 | 12.88 | 11.75 | 10.83 | 9.37 | 73 |
| 187 | 11 | 12 | 55.61 | -61 | 16 | 37.92 | 14.03 | 11.31 | 10.06 | 8.64 | 6 |
| 188 | 11 | 12 | 12.98 | -61 | 14 | 44.52 | 12.04 | 11.30 | 11.15 | 13.01 | 127 |
| 189 | 11 | 12 | 29.57 | -61 | 19 | 1.92 | 12.57 | 10.27 | 9.20 | 8.62 | 42 |
| 190 | 11 | 12 | 29.66 | -61 | 24 | 22.32 | 13.47 | 11.26 | 10.28 | 9.59 | 32 |
| 191 | 11 | 12 | 33.36 | -61 | 15 | 52.2 | 11.59 | 10.19 | 9.39 | 8.83 | 28 |
| 192 | 11 | 12 | 20.81 | -61 | 21 | 14.76 | 16.73 | 15.74 | 14.81 | 11.85 | 80 |
| 193 | 11 | 12 | 36.98 | -61 | 16 | 39 | 16.01 | 13.91 | 12.70 | 10.52 | 16 |
| 194 | 11 | 12 | 34.85 | -61 | 18 | 51.48 | 13.96 | 11.16 | 9,91 | 8.94 | 17 |
| 195 | 11 | 12 | 29.40 | -61 | 13 | 54.12 | 11.40 | 10.02 | 9.45 | 9.34 | 54 |
| 196 | 11 | 12 | 16.32 | -61 | 22 | 36.48 | 16.72 | 15.47 | 14.87 | 11.82 | 98 |
| 197 | 11 | 12 | 40.78 | -61 | 16 | 3.36 | 16.97 | 15.41 | 14.95 | 11.09 | 14 |
| 198 | 11 | 12 | 19.80 | -61 | 15 | 22.68 | 14.95 | 14.62 | 14.62 | 12.73 | 100 |
| 199 | 11 | 12 | 32.90 | -61 | 14 | 13.92 | 11.91 | 10.73 | 10.22 | 10.30 | 33 |
| 200 | 11 | 12 | 55.61 | -61 | 16 | 37.92 | 14.03 | 11.31 | 10.06 | 9.55 | 5 |
| 201 | 11 | 12 | 48.36 | -61 | 21 | 10.44 | 13.01 | 10.84 | 9.82 | 9.19 | 10 |
| 202 | 11 | 12 | 59.90 | -61 | 16 | 23.16 | 16.10 | 14.59 | 13.97 | 7.04 | 3 |
| 203 | 11 | 12 | 15.65 | -61 | 21 | 3.96 | 15.45 | 14.14 | 13.62 | 10.34 | 106 |
| 204 | 11 | 12 | 32.66 | -61 | 21 | 43.92 | 14.63 | 13.13 | 12.55 | 13.04 | 26 |
| 205 | 11 | 12 | 22.61 | -61 | 14 | 53.16 | 16.14 | 15.55 | 15.21 | 12.27 | 88 |
| 206 | 11 | 12 | 16.06 | -61 | 16 | 22.44 | 14.36 | 13.68 | 13.47 | 10.54 | 109 |
| 207 | 11 | 12 | 11.21 | -61 | 17 | 41.64 | 14.58 | 13.59 | 13.66 | 9.39 | 123 |
| 208 | 11 | 12 | 19.03 | -61 | 15 | 8.64 | 15.86 | 15.35 | 14.96 | 11.45 | 94 |
| 209 | 11 | 12 | 26.95 | -61 | 21 | 3.96 | 14.82 | 14.40 | 14.50 | 13.07 | 47 |

| *id* | *RA (J2000)* *h m s* | | | *Dec (J2000)* *d m s* | | | $m_J$ | $m_H$ | $m_K$ | $m_L$ | $id_{IRAF}$ |
|---|---|---|---|---|---|---|---|---|---|---|---|
| 210 | 11 | 12 | 29.26 | -61 | 19 | 26.4 | 15.75 | 15.27 | 14.74 | 12.93 | 45 |
| 211 | 11 | 12 | 13.22 | -61 | 20 | 57.12 | 15.60 | 14.76 | 14.38 | 13.02 | 116 |
| 212 | 11 | 12 | 41.62 | -61 | 21 | 5.4 | 11.78 | 10.76 | 10.34 | 10.20 | 12 |
| 213 | 11 | 12 | 33.36 | -61 | 16 | 5.16 | 16.17 | 13.58 | 11.95 | 9.90 | 27 |
| 214 | 11 | 12 | 28.27 | -61 | 22 | 23.52 | - | - | 14.33 | 9.64 | 43 |
| 215 | 11 | 12 | 18.10 | -61 | 20 | 55.32 | - | - | 14.80 | 10.42 | 93 |
| 216 | 11 | 12 | 26.45 | -61 | 20 | 18.24 | - | - | 15.23 | 10.57 | 56 |
| 217 | 11 | 12 | 20.04 | -61 | 19 | 50.16 | - | - | 13.63 | 12.42 | 83 |
| 218 | 11 | 12 | 21.89 | -61 | 15 | 23.76 | - | - | 15.47 | 11.31 | 89 |
| 219 | 11 | 12 | 10.85 | -61 | 17 | 27.24 | - | - | 13.63 | 9.36 | 134 |
| 220 | 11 | 12 | 16.10 | -61 | 16 | 11.28 | - | - | 14.07 | 9.83 | 103 |
| 221 | 11 | 11 | 28.73 | -61 | 21 | 55.08 | - | - | 14.71 | 10.98 | 331 |
| 222 | 11 | 11 | 54.07 | -61 | 20 | 38.76 | - | - | 14.21 | 14.04 | 232 |
| 223 | 11 | 11 | 53.14 | -61 | 18 | 36.36 | - | - | 10.65 | 7.37 | 223 |
| 224 | 11 | 11 | 29.26 | -61 | 18 | 33.12 | - | - | 15.50 | 10.75 | 332 |
| 225 | 11 | 11 | 25.94 | -61 | 16 | 28.92 | - | - | 15.56 | 12.09 | 346 |
| 226 | 11 | 11 | 56.42 | -61 | 14 | 17.52 | - | - | 15.17 | 10.27 | 226 |
| 227 | 11 | 12 | 1.56 | -61 | 19 | 18.84 | - | - | 14.95 | 10.44 | 175 |
| 228 | 11 | 11 | 56.09 | -61 | 19 | 1.2 | - | - | 12.15 | 8.82 | 206 |
| 229 | 11 | 11 | 50.18 | -61 | 19 | 4.44 | - | - | 11.27 | 6.72 | 393 |
| 230 | 11 | 12 | 6.60 | -61 | 19 | 28.56 | - | - | - | 10.16 | 137 |
| 231 | 11 | 12 | 5.14 | -61 | 19 | 33.96 | - | - | - | 9.74 | 153 |
| 232 | 11 | 12 | 5.57 | -61 | 18 | 34.2 | - | - | - | 8.75 | 154 |
| 233 | 11 | 12 | 4.44 | -61 | 19 | 46.56 | - | - | - | 9.50 | 158 |
| 234 | 11 | 12 | 2.69 | -61 | 21 | 50.4 | - | - | - | 11.70 | 163 |
| 235 | 11 | 12 | 2.52 | -61 | 20 | 17.88 | - | - | - | 9.54 | 167 |
| 236 | 11 | 12 | 3.91 | -61 | 15 | 23.04 | - | - | - | 11.49 | 172 |
| 237 | 11 | 11 | 56.18 | -61 | 22 | 21.36 | - | - | - | 11.81 | 195 |
| 238 | 11 | 12 | - | -61 | 11 | 53.16 | - | - | - | 9.77 | 198 |
| 239 | 11 | 11 | 54.31 | -61 | 23 | 25.08 | - | - | - | 11.18 | 205 |
| 240 | 11 | 11 | 55.25 | -61 | 18 | 26.28 | - | - | - | 8.23 | 207 |
| 241 | 11 | 11 | 56.59 | -61 | 15 | 54.36 | - | - | - | 11.84 | 217 |
| 242 | 11 | 11 | 52.30 | -61 | 22 | 57 | - | - | - | 10.94 | 230 |
| 243 | 11 | 11 | 52.42 | -61 | 21 | 14.76 | - | - | - | 10.20 | 233 |
| 244 | 11 | 11 | 52.15 | -61 | 22 | 45.48 | - | - | - | 10.36 | 235 |
| 245 | 11 | 11 | 52.42 | -61 | 18 | 28.08 | - | - | - | 7.15 | 237 |
| 246 | 11 | 11 | 55.10 | -61 | 15 | 30.6 | - | - | - | 11.20 | 239 |
| 247 | 11 | 11 | 53.69 | -61 | 16 | 30.72 | - | - | - | 10.65 | 240 |
| 248 | 11 | 11 | 50.06 | -61 | 22 | 38.64 | - | - | - | 10.39 | 251 |
| 249 | 11 | 11 | 50.47 | -61 | 21 | 42.12 | - | - | - | 10.87 | 256 |
| 250 | 11 | 11 | 48.84 | -61 | 19 | 59.52 | - | - | - | 11.67 | 272 |
| 251 | 11 | 11 | 45.41 | -61 | 22 | 4.44 | - | - | - | 11.90 | 277 |

| *id* | *RA (J2000)* *h m s* | | | *Dec (J2000)* *d m s* | | | $m_J$ | $m_H$ | $m_K$ | $m_L$ | $id_{IRAF}$ |
|---|---|---|---|---|---|---|---|---|---|---|---|
| 252 | 11 | 11 | 45.41 | -61 | 22 | 12.36 | - | - | - | 11.34 | 278 |
| 253 | 11 | 11 | 29.98 | -61 | 22 | 3.36 | - | - | - | 11.72 | 328 |
| 254 | 11 | 11 | 31.70 | -61 | 16 | 0.84 | - | - | - | 10.58 | 334 |
| 255 | 11 | 11 | 28.80 | -61 | 19 | 28.2 | - | - | - | 11.89 | 335 |
| 256 | 11 | 11 | 30.12 | -61 | 13 | 42.6 | - | - | - | 10.76 | 336 |
| 257 | 11 | 11 | 28.85 | -61 | 15 | 51.12 | - | - | - | 11.71 | 338 |
| 258 | 11 | 11 | 25.56 | -61 | 21 | 37.08 | - | - | - | 10.70 | 342 |
| 259 | 11 | 11 | 26.95 | -61 | 17 | 8.16 | - | - | - | 11.68 | 344 |
| 260 | 11 | 11 | 24.43 | -61 | 16 | 58.08 | - | - | - | 11.56 | 354 |
| 261 | 11 | 11 | 22.27 | -61 | 18 | 49.32 | - | - | - | 11.07 | 356 |
| 262 | 11 | 11 | 21.38 | -61 | 18 | 47.88 | - | - | - | 11.22 | 359 |
| 263 | 11 | 11 | 5.74 | -61 | 15 | 9.72 | - | - | - | 10.03 | 379 |
| 264 | 11 | 11 | 5.18 | -61 | 15 | 37.08 | - | - | - | 9.42 | 380 |
| 265 | 11 | 10 | 58.82 | -61 | 18 | 2.88 | - | - | - | 9.27 | 382 |
| 266 | 11 | 13 | 2.09 | -61 | 16 | 44.4 | - | - | - | 9.23 | 2 |
| 267 | 11 | 12 | 56.18 | -61 | 16 | 29.64 | - | - | - | 9.73 | 4 |
| 268 | 11 | 12 | 53.78 | -61 | 16 | 33.24 | - | - | - | 8.60 | 7 |
| 269 | 11 | 12 | 49.63 | -61 | 18 | 5.04 | - | - | - | 10.29 | 11 |
| 270 | 11 | 12 | 30.58 | -61 | 20 | 25.08 | - | - | - | 10.44 | 29 |
| 271 | 11 | 12 | 29.42 | -61 | 19 | 55.56 | - | - | - | 10.96 | 41 |
| 272 | 11 | 12 | 25.25 | -61 | 19 | 31.08 | - | - | - | 11.68 | 65 |
| 273 | 11 | 12 | 20.90 | -61 | 20 | 39.84 | - | - | - | 11.83 | 81 |
| 274 | 11 | 12 | 19.78 | -61 | 22 | 31.8 | - | - | - | 11.46 | 82 |
| 275 | 11 | 12 | 17.98 | -61 | 15 | 42.84 | - | - | - | 10.68 | 97 |
| 276 | 11 | 12 | 10.87 | -61 | 18 | 54.36 | - | - | - | 9.10 | 118 |
| 277 | 11 | 12 | 13.97 | -61 | 15 | 29.52 | - | - | - | 10.59 | 125 |
| 278 | 11 | 12 | 8.09 | -61 | 19 | 26.76 | - | - | - | 9.71 | 138 |
| 279 | 11 | 12 | 59.54 | -61 | 20 | 2.4 | - | - | - | 8.88 | 385 |

*Table 2: Coordinates and magnitudes for sources in RCW 57.*

## Galactic Centre

| *id* | *RA (J2000)* *h m s* | | | *Dec (J2000)* *d m s* | | | $m_J$ | $m_H$ | $m_K$ | $m_{Br\alpha}$ | $id_{IRAF}$ |
|---|---|---|---|---|---|---|---|---|---|---|---|
| 1 | 17 | 45 | 44.33 | -28 | 59 | 13.2 | 14.13 | 10.33 | 7.92 | 6.00 | 2229 |
| 2 | 17 | 45 | 34.42 | -29 | 1 | 33.96 | 13.51 | 10.89 | 9.29 | 6.64 | 1673 |
| 3 | 17 | 45 | 44.45 | -29 | 0 | 56.52 | 17.21 | 13.49 | 10.51 | 8.75 | 1829 |
| 4 | 17 | 45 | 37.30 | -28 | 59 | 22.92 | 14.71 | 12.39 | 10.07 | 8.35 | 2180 |
| 5 | 17 | 45 | 44.11 | -29 | 1 | 31.44 | 17.63 | 12.49 | 10.08 | 8.06 | 1706 |
| 6 | 17 | 45 | 42.34 | -29 | 0 | 36.72 | 12.21 | 11.79 | 9.57 | 6.58 | 1902 |
| 7 | 17 | 45 | 41.40 | -29 | 1 | 26.76 | 14.95 | 12.77 | 10.55 | 7.43 | 1714 |
| 8 | 17 | 45 | 42.84 | -28 | 59 | 42.72 | 15.08 | 10.97 | 9.03 | 7.88 | 2123 |
| 9 | 17 | 45 | 35.09 | -29 | 1 | 41.88 | 15.80 | 12.17 | 11.23 | 7.09 | 1646 |
| 10 | 17 | 45 | 35.88 | -29 | 0 | 52.56 | 15.77 | 11.70 | 9.26 | 7.47 | 1818 |
| 11 | 17 | 45 | 35.66 | -28 | 59 | 42.72 | 16.13 | 11.79 | 9.62 | 8.30 | 2098 |
| 12 | 17 | 45 | 45.43 | -29 | 0 | 0.36 | 15.93 | 11.24 | 9.00 | 6.78 | 2057 |
| 13 | 17 | 45 | 39.38 | -29 | 0 | 14.76 | 15.12 | 10.62 | 8.35 | 5.42 | 1965 |
| 14 | 17 | 45 | 42.34 | -28 | 59 | 17.88 | 16.70 | 12.02 | 9.40 | 7.47 | 2210 |
| 15 | 17 | 45 | 35.57 | -28 | 59 | 27.96 | 17.42 | 13.23 | 10.49 | 9.83 | 2156 |
| 16 | 17 | 45 | 40.44 | -29 | 1 | 10.56 | 17.01 | 13.46 | 11.24 | 7.93 | 1767 |
| 17 | 17 | 45 | 46.08 | -29 | 0 | 20.16 | 15.84 | 14.11 | 11.69 | 11.23 | 1949 |
| 18 | 17 | 45 | 39.36 | -29 | 0 | 39.24 | 15.05 | 11.08 | 9.07 | 5.67 | 1893 |
| 19 | 17 | 45 | 43.51 | -29 | 0 | 5.04 | 14.99 | 11.09 | 9.32 | 7.36 | 2029 |
| 20 | 17 | 45 | 42.70 | -28 | 59 | 57.84 | 14.80 | 10.42 | 7.98 | 5.53 | 2061 |
| 21 | 17 | 45 | 36.98 | -29 | 1 | 38.64 | 15.30 | 12.55 | 10.26 | 7.38 | 1664 |
| 22 | 17 | 45 | 40.10 | -28 | 59 | 40.2 | 15.64 | 11.36 | 8.93 | 7.03 | 2126 |
| 23 | 17 | 45 | 41.18 | -29 | 0 | 46.8 | 15.84 | 10.65 | 7.98 | 5.38 | 1858 |
| 24 | 17 | 45 | 45.29 | -29 | 1 | 10.2 | 15.72 | 11.73 | 9.85 | 8.59 | 1784 |
| 25 | 17 | 45 | 40.61 | -29 | 1 | 21.72 | 14.85 | 11.13 | 9.33 | 8.32 | 1732 |
| 26 | 17 | 45 | 40.70 | -29 | 0 | 11.16 | 12.40 | 11.68 | 9.40 | 5.46 | 1985 |
| 27 | 17 | 45 | 36.79 | -29 | 0 | 25.56 | 15.63 | 11.62 | 9.69 | 7.24 | 1915 |
| 28 | 17 | 45 | 38.30 | -28 | 59 | 42 | 15.28 | 11.00 | 8.83 | 7.04 | 2109 |
| 29 | 17 | 45 | 38.02 | -29 | 1 | 2.28 | 15.75 | 11.83 | 9.10 | 6.43 | 1794 |
| 30 | 17 | 45 | 38.59 | -29 | 0 | 54 | 16.64 | 13.02 | 9.82 | 6.14 | 1821 |
| 31 | 17 | 45 | 35.93 | -29 | 0 | 35.64 | 14.48 | 10.27 | 8.17 | 6.38 | 1879 |
| 32 | 17 | 45 | 34.94 | -28 | 59 | 55.32 | 15.77 | 12.10 | 9.80 | 8.25 | 2042 |
| 33 | 17 | 45 | 43.15 | -29 | 0 | 50.04 | 16.47 | 11.78 | 9.13 | 6.36 | 1852 |
| 34 | 17 | 45 | 42.77 | -29 | 1 | 25.68 | 14.31 | 10.90 | 9.05 | 7.55 | 1724 |
| 35 | 17 | 45 | 43.30 | -29 | 1 | 19.2 | 17.63 | 14.77 | 11.85 | 8.33 | 1753 |
| 36 | 17 | 45 | 41.50 | -28 | 59 | 58.92 | 15.17 | 11.63 | 9.45 | 6.93 | 2056 |
| 37 | 17 | 45 | 36.86 | -29 | 1 | 14.52 | 16.45 | 12.57 | 9.82 | 7.45 | 1746 |
| 38 | 17 | 45 | 40.13 | -28 | 59 | 47.76 | 16.66 | 13.51 | 10.50 | 5.43 | 2089 |
| 39 | 17 | 45 | 45.46 | -28 | 59 | 34.8 | 14.25 | 10.78 | 8.99 | 7.46 | 2161 |
| 40 | 17 | 45 | 41.30 | -28 | 59 | 38.04 | 14.67 | 10.51 | 8.28 | 6.44 | 2139 |
| 41 | 17 | 45 | 37.01 | -29 | 1 | 5.16 | 15.44 | 12.26 | 9.99 | 7.68 | 1782 |

| *id* | *RA (J2000)* *h m s* | | | *Dec (J2000)* *d m s* | | | $m_J$ | $m_H$ | $m_K$ | $m_{Br\alpha}$ | $id_{IRAF}$ |
|---|---|---|---|---|---|---|---|---|---|---|---|
| 42 | 17 | 45 | 45.24 | -29 | 0 | 47.88 | 15.99 | 12.97 | 10.96 | 7.55 | 1863 |
| 43 | 17 | 45 | 39.96 | -29 | 0 | 10.8 | 14.94 | 11.51 | 9.33 | 5.62 | 2027 |
| 44 | 17 | 45 | 45.36 | -28 | 59 | 43.8 | 15.96 | 11.53 | 9.26 | 7.25 | 2129 |
| 45 | 17 | 45 | 37.92 | -28 | 59 | 26.52 | 17.09 | 13.29 | 11.08 | 7.33 | 2170 |
| 46 | 17 | 45 | 38.26 | -29 | 0 | 6.48 | 14.81 | 11.65 | 9.26 | 6.48 | 2009 |
| 47 | 17 | 45 | 35.23 | -29 | 0 | 48.96 | 15.16 | 11.85 | 10.02 | 8.65 | 1834 |
| 48 | 17 | 45 | 39.84 | -29 | 0 | 54 | 13.58 | 9.65 | 7.39 | 5.49 | 1823 |
| 49 | 17 | 45 | 42.07 | -28 | 59 | 35.16 | 15.54 | 10.97 | 8.96 | 7.06 | 2151 |
| 50 | 17 | 45 | 41.76 | -29 | 0 | 4.68 | 16.43 | 11.97 | 9.31 | 6.41 | 2026 |
| 51 | 17 | 45 | 39.82 | -29 | 0 | 29.88 | 14.72 | 10.79 | 8.16 | 2.82 | 1903 |
| 52 | 17 | 45 | 40.46 | -29 | 0 | 27.36 | 13.30 | 9.44 | 7.90 | 3.64 | 1921 |
| 53 | 17 | 45 | 45.79 | -29 | 1 | 37.92 | 17.75 | 15.09 | 11.37 | 7.37 | 1690 |
| 54 | 17 | 45 | 44.66 | -28 | 59 | 58.92 | 14.66 | 11.32 | 8.98 | 6.23 | 2066 |
| 55 | 17 | 45 | 40.68 | -29 | 0 | 18 | 14.70 | 10.85 | 9.35 | 4.57 | 1931 |
| 56 | 17 | 45 | 36.96 | -29 | 0 | 57.6 | - | - | 9.50 | 7.21 | 1802 |
| 57 | 17 | 45 | 36.31 | -29 | 0 | 41.4 | - | - | 9.34 | 7.35 | 1825 |
| 58 | 17 | 45 | 44.21 | -28 | 59 | 22.56 | - | - | 10.58 | 8.83 | 2198 |
| 59 | 17 | 45 | 36.67 | -29 | 0 | 15.84 | - | - | 8.60 | 6.45 | 1953 |
| 60 | 17 | 45 | 36.77 | -29 | 1 | 30 | - | - | 9.33 | 7.51 | 1693 |
| 61 | 17 | 45 | 43.13 | -29 | 0 | 12.96 | - | - | 7.95 | 5.72 | 1989 |
| 62 | 17 | 45 | 44.95 | -28 | 59 | 18.96 | - | - | 9.11 | 7.42 | 2215 |
| 63 | 17 | 45 | 35.83 | -29 | 0 | 5.04 | - | - | 9.19 | 7.76 | 1986 |
| 64 | 17 | 45 | 40.18 | -28 | 59 | 58.92 | - | - | 9.50 | 4.65 | 2046 |
| 65 | 17 | 45 | 36.65 | -29 | 1 | 21 | - | - | 10.19 | 7.81 | 1702 |
| 66 | 17 | 45 | 39.46 | -29 | 0 | 56.16 | - | - | 8.17 | 5.72 | 1816 |
| 67 | 17 | 45 | 39.60 | -28 | 59 | 35.16 | - | - | 9.18 | 7.32 | 2144 |
| 68 | 17 | 45 | 34.82 | -29 | 1 | 49.08 | - | - | 10.05 | 7.97 | 1626 |
| 69 | 17 | 45 | 38.93 | -29 | 1 | 23.16 | - | - | 11.54 | 8.22 | 1717 |
| 70 | 17 | 45 | 37.34 | -28 | 59 | 49.92 | - | - | 10.79 | 9.49 | 2073 |
| 71 | 17 | 45 | 40.63 | -29 | 0 | 24.12 | - | - | 8.40 | 4.15 | 1957 |
| 72 | 17 | 45 | 38.62 | -28 | 59 | 58.2 | - | - | 9.82 | 6.65 | 2093 |
| 73 | 17 | 45 | 39.17 | -28 | 59 | 36.96 | - | - | 9.77 | 8.12 | 2137 |
| 74 | 17 | 45 | 44.78 | -29 | 0 | 8.64 | - | - | 10.11 | 7.77 | 2016 |
| 75 | 17 | 45 | 37.87 | -29 | 0 | 45.72 | - | - | 10.12 | 7.70 | 1848 |
| 76 | 17 | 45 | 37.30 | -29 | 0 | 45.72 | - | - | 11.34 | 7.10 | 1856 |
| 77 | 17 | 45 | 43.27 | -29 | 0 | 26.28 | - | - | 10.59 | 9.48 | 1935 |
| 78 | 17 | 45 | 40.61 | -28 | 59 | 15 | - | - | 9.97 | 8.22 | 2217 |
| 79 | 17 | 45 | 39.58 | -28 | 59 | 56.76 | - | - | 9.92 | 7.07 | 2108 |
| 80 | 17 | 45 | 40.06 | -29 | 0 | 22.68 | - | - | 7.02 | 2.59 | 1938 |
| 81 | 17 | 45 | 41.40 | -29 | 0 | 23.4 | - | - | 9.00 | 5.36 | 1956 |
| 82 | 17 | 45 | 37.75 | -29 | 1 | 15.6 | - | - | 10.32 | 7.92 | 1745 |
| 83 | 17 | 45 | 46.15 | -28 | 59 | 38.76 | - | - | 10.61 | 8.21 | 2148 |

| *id* | *RA (J2000)* *h m s* | | | *Dec (J2000)* *d m s* | | | $m_J$ | $m_H$ | $m_K$ | $m_{Br\alpha}$ | $id_{IRAF}$ |
|---|---|---|---|---|---|---|---|---|---|---|---|
| 84 | 17 | 45 | 37.78 | -29 | 1 | 33.96 | - | - | - | 7.80 | 1682 |
| 85 | 17 | 45 | 38.98 | -29 | 1 | 2.64 | - | - | - | 6.50 | 1760 |
| 86 | 17 | 45 | 39.86 | -29 | 1 | 10.56 | - | - | - | 6.93 | 1769 |
| 87 | 17 | 45 | 40.51 | -29 | 0 | 54.36 | - | - | - | 6.17 | 1822 |
| 88 | 17 | 45 | 41.09 | -29 | 0 | 33.48 | - | - | - | 4.74 | 1865 |
| 89 | 17 | 45 | 39.38 | -29 | 0 | 26.28 | - | - | - | 4.61 | 1975 |
| 90 | 17 | 45 | 39.07 | -29 | 0 | 8.28 | - | - | - | 6.48 | 1997 |
| 91 | 17 | 45 | 39.58 | -29 | 0 | 5.4 | - | - | - | 6.37 | 2058 |

*Table 3: Coordinates and magnitudes for sources in the Galactic Centre.*

# Appendix C

## IRAF/Daophot parameters

| DATAPARS | FINDPARS | CENTERPARS | FITSKYPARS | PHOTPARS | DAOPARS |
|---|---|---|---|---|---|
| scale = 1. | threshold = 4. | calgorithm = "none" | salgorithm = | weighting = | function = "gauss" |
| fwhmpsf = 4.48 | nsigma = 1.5 | cbox = 8.96 | "median" | "constant" | varorder = 0 |
| emission = yes | ratio = 1. | cthreshold = 0. | annulus = 17.92 | apertures = "INFIN" | nclean = 0 |
| sigma = 2. | theta = 0. | minsnratio = 1. | dannulus = 13.44 | zmag = 18. | saturated = no |
| datamin = -24. | sharplo = 0.2 | cmaxiter = 10 | skyvalue = 0. | mkapert = no | matchrad = 3. |
| datamax = 1143.964 | sharphi = 1. | maxshift = 1. | smaxiter = 10 | mode = "ql" | psfrad = 14. |
| noise = "poisson" | roundlo = -1. | clean = no | sloclip = 0. | | fitrad = 4.48 |
| ccdread = " " | roundhi = 1. | rclean = 1. | shiclip = 0. | | recenter = yes |
| gain = " " | mkdetections = no | rclip = 2. | snreject = 50 | | fitsky = no |
| readnoise = 0. | mode = "ql | kclean = 3. | sloreject = 3. | | groupsky = yes |
| epadu = 0. | | mkcenter = no | shireject = 3. | | sannulus = 19.92 |
| exposure = " " | | mode = "ql" | khist = 3. | | wsannulus = 13.44 |
| airmass = " " | | | binsize = 0.1 | | flaterr = 0.75 |
| filter = "FILTER" | | | smooth = no | | proferr = 5. |
| obstime = "UT" | | | rgrow = 0. | | maxiter = 50 |
| itime = 1. | | | mksky = no | | clipexp = 6 |
| xairmass = INDEF | | | mode = "ql" | | cliprange = 2.5 |
| ifilter = "INDEF" | | | | | mergerad = INDEF |
| otime = "INDEF" | | | | | critsnratio = 1. |
| mode = "ql" | | | | | maxnstar = 10000 |
| | | | | | maxgroup = 60 |
| | | | | | mode = "ql" |

*Table 1: Parameters for photometry in IRAF/DAOPHOT for 30 Doradus.*

| DATAPARS | FINDPARS | CENTERPARS | FITSKYPARS | PHOTPARS | DAOPARS |
|---|---|---|---|---|---|
| scale = 1. | threshold = 3. | calgorithm = "gauss" | salgorithm = | weighting = | function = "gauss" |
| fwhmpsf = 8. | nsigma = 1.5 | cbox = 16. | "median" | "constant" | varorder = 0 |
| emission = yes | ratio = 1. | cthreshold = 0. | annulus = 32. | apertures = "8" | nclean = 0 |
| sigma = 7. | theta = 0. | minsnratio = 1. | dannulus = 20. | zmag = 17.92 | saturated = no |
| datamin = -56. | sharplo = 0.2 | cmaxiter = 10 | skyvalue = 0. | mkapert = no | matchrad = 3. |
| datamax = 2000. | sharphi = 1. | maxshift = 1. | smaxiter = 10 | mode = "ql" | psfrad = 13. |
| noise = "poisson" | roundlo = -1. | clean = no | sloclip = 0. | | fitrad = 8. |
| ccdread = " " | roundhi = 1. | rclean = 1. | shiclip = 0. | | recenter = yes |
| gain = " " | mkdetections = no | rclip = 2. | snreject = 50 | | fitsky = no |
| readnoise = 0. | mode = "ql" | kclean = 3. | sloreject = 3. | | groupsky = yes |
| epadu = 0. | | mkcenter = no | shireject = 3. | | sannulus = 0. |
| exposure = " " | | mode = "ql" | khist = 3. | | wsannulus = 11. |
| airmass = " " | | | binsize = 0.1 | | flaterr = 0.75 |
| filter = "FILTER" | | | smooth = no | | proferr = 5. |
| obstime = "UT" | | | rgrow = 0. | | maxiter = 50 |
| itime = 1. | | | mksky = no | | clipexp = 6 |
| xairmass = INDEF | | | mode = "ql" | | cliprange = 2.5 |
| ifilter = "INDEF" | | | | | mergerad = INDEF |
| otime = "INDEF" | | | | | critsnratio = 1. |
| mode = "ql" | | | | | maxnstar = 10000 |
| | | | | | maxgroup = 60 |
| | | | | | mode = "ql" |

*Table 2: Parameters for photometry in IRAF/DAOPHOT for RCW 57.*

| **DATAPARS** | **FINDPARS** | **CENTERPARS** | **FITSKYPARS** | **PHOTPARS** | **DAOPARS** |
|---|---|---|---|---|---|
| scale = 1. | threshold = 3. | calgorithm = "none" | salgorithm = | weighting = | function = "gauss" |
| fwhmpsf = 8.5 | nsigma = 1.5 | cbox = 17. | "median" | "constant" | varorder = 0 |
| emission = yes | ratio = 1. | cthreshold = 0. | annulus = 34. | apertures = "8.5" | nclean = 0 |
| sigma = 10. | theta = 0. | minsnratio = 1. | dannulus = 21.25 | zmag = 18. | saturated = no |
| datamin = -88. | sharplo = 0.2 | cmaxiter = 10 | skyvalue = 0. | mkapert = no | matchrad = 3. |
| datamax = 1143.964 | sharphi = 1. | maxshift = 1. | smaxiter = 10 | mode = "ql" | psfrad = 35. |
| noise = "poisson" | roundlo = -1. | clean = no | sloclip = 0. | | fitrad = 8.5 |
| ccdread = " " | roundhi = 1. | rclean = 1. | shiclip = 0. | | recenter = yes |
| gain = " " | mkdetections = no | rclip = 2. | snreject = 50 | | fitsky = no |
| readnoise = 0. | mode = "ql" | kclean = 3. | sloreject = 3. | | groupsky = yes |
| epadu = 0. | | mkcenter = no | shireject = 3. | | sannulus = 30. |
| exposure = " " | | mode = "ql" | khist = 3. | | wsannulus = 20. |
| airmass = " " | | | binsize = 0.1 | | flaterr = 0.75 |
| filter = "FILTER" | | | smooth = no | | proferr = 5. |
| obstime = "UT" | | | rgrow = 0. | | maxiter = 50 |
| itime = 1. | | | mksky = no | | clipexp = 6 |
| xairmass = INDEF | | | mode = "ql" | | cliprange = 2.5 |
| ifilter = "INDEF" | | | | | mergerad = INDEF |
| otime = "INDEF" | | | | | critsnratio = 1. |
| mode = "ql" | | | | | maxnstar = 10000 |
| | | | | | maxgroup = 60 |
| | | | | | mode = "ql" |

*Table 3:Parameters for photometry in IRAF/DAOPHOT for the Galactic Centre.*